Universität Regensburg

Transport measurements on graphene

Dissertation
zur Erlangung des Doktorgrades der Naturwissenschaften
(Dr. rer. nat.)
der Fakultät für Physik
der Universität Regensburg

vorgelegt von
Silvia Minke, geb. Schmidmeier, aus Zeitlarn
Regensburg, Mai 2012

Die Arbeit wurde von Prof. Dr. Dieter Weiss angeleitet.
Das Promotionsgesuch wurde am 08.05.2012 eingereicht.
Das Promotionskolloquium fand am 09.07.2012 statt.

Prüfungsausschuss:

Vorsitzender:	Prof. Dr. Gunnar Bali
1. Gutachter:	Prof. Dr. Dieter Weiss
2. Gutachter:	Prof. Dr. Klaus Richter
weiterer Prüfer:	Prof. Dr. John Lupton

Contents

1 Introduction

The Nobel Prize in Physics 2010 was awarded jointly to Andre Geim and Konstantin Novoselov "for groundbreaking experiments regarding the two-dimensional material graphene" [1]. Graphene is a monolayer of carbon atoms arranged in a honeycomb-like hexagonal lattice.

> It *"...is a wonder material with many superlatives to its name. It is the thinnest known material in the universe and the strongest ever measured. Its charge carriers exhibit giant intrinsic mobility, have zero effective mass, and can travel for micrometers without scattering at room temperature..."* [2].

Consequently it is no surprise that graphene is a very promising material for future applications. Furthermore the relativistic nature of the charge carriers makes it interesting for fundamental questions in condensed matter physics.
Graphene is the thinnest member of the few layer graphene (FLG) family. Due to the outstanding properties of single layer graphene it becomes obvious that it is also important to study the other FLG materials. Bilayer graphene, for example, has a gate-tunable band gap, whereas trilayer graphene exhibits either a gate-tunable band overlap or a band gap, depending on the stacking order of the layers.

This thesis presents some of the above mentioned multifarious diversity of graphite materials. Here, we want to focus on both trilayer graphene devices as well as graphene nanoribbons, which are thin stripes of (single-layer) graphene. On the one hand graphene nanoribbons (GNRs) and arrays of GNRs were measured at the University of Regensburg in magnetic fields up to 16 T, where their phase coherent properties were studied. On the other hand GNRs were measured at Dresden High Magnetic Field Laboratory in pulsed magnetic fields up to 60 T, in order to gain information about the disorder present in our samples. Furthermore, trilayer graphene samples were measured at Dresden High Magnetic Field Laboratory, where the transport properties of differently stacked trilayer devices (ABA and ABC, respectively) were investigated.

The thesis is organized as follows: In Chapter 2 we briefly review the basic electronic properties of graphene materials. First we introduce the band structure of single-, bi- and trilayer graphene, then we discuss some of the main relevant effects observed in magneto-transport experiments. Followed by the properties of graphene nanoribbons.
Then the sample preparation of graphene nanoribbon devices as well as of trilayer samples is illustrated in Chapter 3. We introduce the differences in the measurement setup for different sample types at different laboratories.
In Chapter 4 we discuss the measurements of our graphene nanoribbon samples done at the University Regensburg. First we present the theoretical background of different phase coherent effects in graphene. Then we use these theoretical models to analyze the experimental data. We analyze individual graphene nanoribbons as well as arrays of nanoribbons at Kelvin and mK-temperature.
In Chapter 5 measurements on graphene nanoribbons in pulsed magnetic fields are introduced. We present experimental data and corresponding numerical simulations, which explain the observed features and give a new understanding of the disorder present in our samples.
Chapter 6 is dedicated to measurements on trilayer graphene samples. We first present how Raman measurements can determine the stacking-order of trilayer samples, then we discuss the magneto-transport measurements of both, ABA and ABC-stacked trilayer graphene samples, and show the differences of the different sample types.
Chapter 7 summarizes the main findings of this thesis and is followed by an appendix, where details of the sample preparation (Chap. 8), the measurement setup and the sample layout as well as additional measurements are presented (Chap. 9).

2 Basic Properties of Graphene Materials

In the first part of this chapter we introduce the band structure of single-, bi- and trilayer graphene. We explain how to set up the corresponding Hamiltonians and how to deduce distinct sample properties. This chapter is mainly based on the publications [3–7]. In the second part we will briefly review the magneto-transport properties of the different few layer graphene materials, we follow Ref. [8], which summarizes the properties of single-, bi- and trilayer graphene. The last section is dedicated graphene nanoribbons, which will be the focus of Chapter 4 and 5. First we focus on the theoretical predictions for transport properties deduced for a certain edge structure and then we will discuss the state of the art of GNR experiments.

2.1 Electronic Properties

In single layer graphene the carbon atoms are arranged in a honeycomb structure, which is formed by a triangular lattice with a basis of two atoms per unit cell (denoted as A and B) as shown in Fig. 2.1(a). The carbon atoms form covalent bonds by three in-plane sp^2 hybridized orbitals between the nearest-neighbors and cause the hexagonal lattice structure. The remaining p-electron (of the $2s^2p^2$ orbitals of carbon) moves freely in plane, forming the so called π-electronic system. The delocalized π-electronic states cause electronic conductance and make graphene a semi-metal. The energy band dispersion can be calculated using a tight-binding model and the electronic states close to the Fermi level can be described by an effective Hamiltonian:

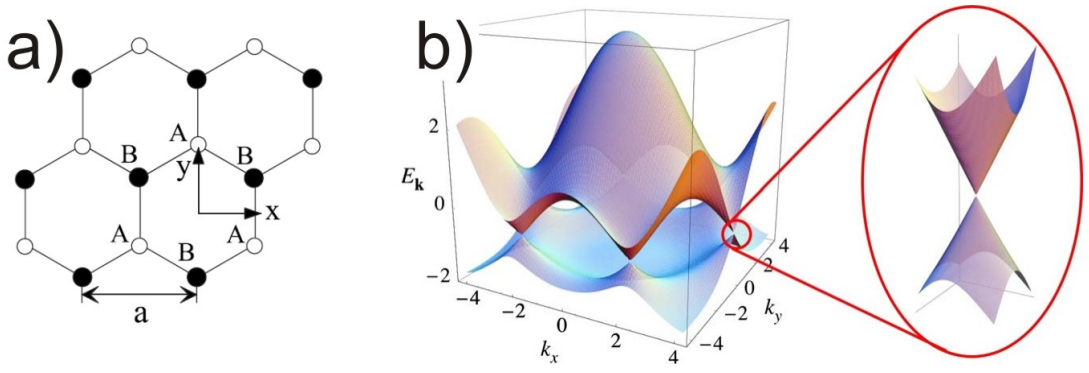

Figure 2.1: (a) Lattice of single layer graphene showing A and B sites [9]. (b) Electronic dispersion in the honeycomb lattice, right: zoom in of the energy bands close to one of the Dirac points [10].

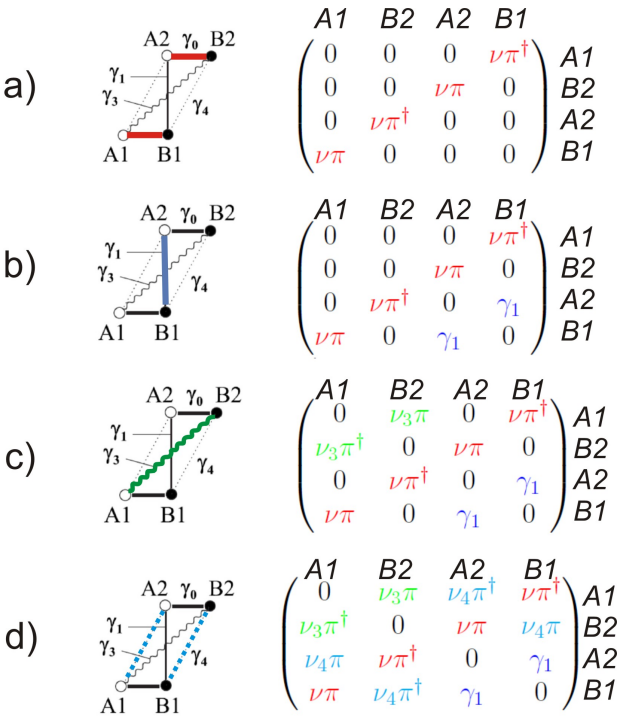

Figure 2.2:
Setting up the bilayer Hamiltonian using the Slonczewski-Weiss-McClure parameters of tight-binding couplings of bulk graphene: (a) First we consider only the nearest-neighbor hopping within each honeycomb layer by γ_0, which enters in the terms $\nu\pi$ and $\nu\pi^\dagger$ (marked in red).
In (b) we additionally include the inter-layer coupling γ_1 (blue).
In (c) we furthermore take into account the inter-layer coupling $A1$-$B2$, described by γ_3, which enters in $\nu_3\pi$ and $\nu_3\pi^\dagger$ (green).
And in (d) the inter-layer hopping γ_4, which describes $A1$-$A2$ and $B1$-$B2$ hopping. It enters in the terms $\nu_4\pi$ and $\nu_4\pi^\dagger$(cyan). Schematics on the left side adopted from Ref. [4].

$$\hat{H}_1 = \xi\nu \begin{pmatrix} 0 & \pi^\dagger \\ \pi & 0 \end{pmatrix} \equiv \xi\nu(\sigma_x p_x + \sigma_y p_y). \tag{2.1}$$

Here $\pi = p_x + ip_y$ is related to the in-plane momentum $\vec{p} = (p_x, p_y)$, $\nu = \frac{\sqrt{3}}{2} a\gamma_0/\hbar$ is the effective velocity, where γ_0 describes the strength of the nearest-neighbor hopping within each honeycomb layer, a the lattice constant, $\hbar$ the reduced Planck constant and $\vec{\sigma} = (\sigma_x, \sigma_y)$ is the 2D vector of the Pauli matrices. The band structure of graphene is shown in Fig. 2.1(b), where the valence and conduction band touch at the K and K' points, with the valley index $\xi = +1$ and $\xi = -1$, respectively, at the corners of the first Brillouin zone. In the low energy limit, zoomed-in region in Fig. 2.1(b), the band dispersion is approximately linear and can be described by $\epsilon = \pm\hbar\nu_F|\vec{q}|$ with a Fermi velocity of $\nu_F \approx 10^6$ m/s.

Thicker few layer graphene material systems may be considered as stacks of several single graphene layers. Studies of the low energy electronic band structure of these graphene materials, however, show that each stack is a unique material system and remarkably different from the single layer one, cf. Ref. [11]. In order to better understand the setting up of the Hamiltonians for different FLG systems, it will be shown exemplarily for bilayer graphene. Analogously this can be done for the other FLG materials.
Bernal stacked (AB) bilayer graphene is composed of two coupled honeycomb lattices of carbon atoms. The two layers are arranged according to Bernal ($A2$-$B1$) stacking as shown in Fig. 2.3(a) and (d). It means that half of the sites, $A2$ and $B1$, lie directly above or below a counterpart in the other layer. They are connected by a relatively strong inter-layer coupling γ_1, cf. Fig. 2.3(d). The inter-layer coupling

$A1$-$B2$, described by γ_3, causes trigonal warping and becomes particularly relevant at very low energy (of the order of 1 meV). The so-called trigonal warping effect is a modification of the conical dispersion of the carriers, leading to a trigonal deformation at the K points of the Brillouin zone, compare Fig. 2.4. The parameter γ_4 describes $A1$-$A2$ and $B1$-$B2$ inter-layer hopping and causes asymmetry between the conduction and valence band [3]. Fig. 2.2 explains how to set up the Hamiltonian using the Slonczewski-Weiss-McClure parameters of tight-binding couplings of bulk graphene. The bilayer Hamiltonian can be written as:

$$\hat{H}_2 = \begin{pmatrix} -\Delta/2 & \nu_3\pi & \nu_4\pi^\dagger & \nu\pi^\dagger \\ \nu_3\pi^\dagger & \Delta/2 & \nu\pi & \nu_4\pi \\ \nu_4\pi & \nu\pi^\dagger & \Delta/2 & \gamma_1 \\ \nu\pi & \nu_4\pi^\dagger & \gamma_1 & -\Delta/2 \end{pmatrix}, \tag{2.2}$$

with the effective velocities $\nu_3 = \frac{\sqrt{3}}{2}a\gamma_3/\hbar$, $\nu_4 = \frac{\sqrt{3}}{2}a\gamma_4/\hbar$ and an additional introduced asymmetry gap Δ. In a two component basis of $A1$ and $B2$ it can be written as:

$$\hat{H}_2 = \frac{1}{2m}\begin{pmatrix} 0 & (\pi^\dagger)^2 \\ (\pi)^2 & 0 \end{pmatrix} + \hat{h_{2w}} + ... \tag{2.3}$$

with the effective mass $m = \gamma_1/2\nu^2$. The first term takes into account $A1$-$B2$ hopping via the $A1$-$B2$ dimer state with effective mass m reflecting the energetic cost γ_1 of a transition via the dimer state. This term yields a parabolic spectrum $\epsilon = \pm\hbar^2q^2/2m$ [Fig. 2.3(g)], making bilayer graphene a two dimensional zero-gap semiconductor. Quasi-particles described by $\hat{H}_2$ are chiral, with a degree of chirality related to Berry phase 2 π. Breaking the interlayer symmetry in bilayer graphene, by external top and back gates, leads to the *opening of a band-gap* in the K and K' points as shown in Fig. 2.3(g). The second term $\hat{h_{2w}}$, where the parameter γ_3 enters, describes weak $A1$-$B2$ coupling and produces trigonal warping. For more information about the exact composition of $\hat{h_{2w}}$ or further terms and their contribution, see [3, 5].

Trilayer graphene is the thinnest of the few layer graphene material systems in which all the hopping parameters that play a role in the band structure of bulk graphite, appear for the first time. The Hamiltonians for ABA and ABC trilayer graphene can be set up in a similar way as for bilayer graphene, considering the schematic of the corresponding lattice [Fig. 2.3(b, e) and (c, f)].
For the Bernal stacked (ABA) trilayer graphene we have three layers of carbon with six atoms in the unit cell ($A1$, $B1$, $A2$, $B2$, $A3$, $B3$), see Fig. 2.3(b) and (e). The hopping within a single layer is described by γ_0, the interlayer coupling by γ_1, γ_3, γ_4 and the next-nearest layer hopping by γ_2 and γ_5. The interlayer asymmetry is described by U_1, U_2 and U_3. For the ABA-Hamiltonian we yield:

$$\hat{H}_{ABA} = \begin{pmatrix} U_1 & \nu\pi^\dagger & \nu_4\pi^\dagger & \nu_3\pi & \gamma_2 & 0 \\ \nu\pi & U_1 & \gamma_1 & \nu_4\pi^\dagger & 0 & \gamma_5 \\ \nu_4\pi & \gamma_1 & U_2 & \nu\pi^\dagger & \nu_4\pi & \gamma_1 \\ \nu_3\pi^\dagger & \nu_4\pi & \nu\pi & U_2 & \nu_3\pi^\dagger & \nu_4\pi \\ \gamma_2 & 0 & \nu_4\pi^\dagger & \nu_3\pi & U_3 & \nu\pi^\dagger \\ 0 & \gamma_5 & \gamma_1 & \nu_4\pi^\dagger & \nu\pi & U_3 \end{pmatrix}. \tag{2.4}$$

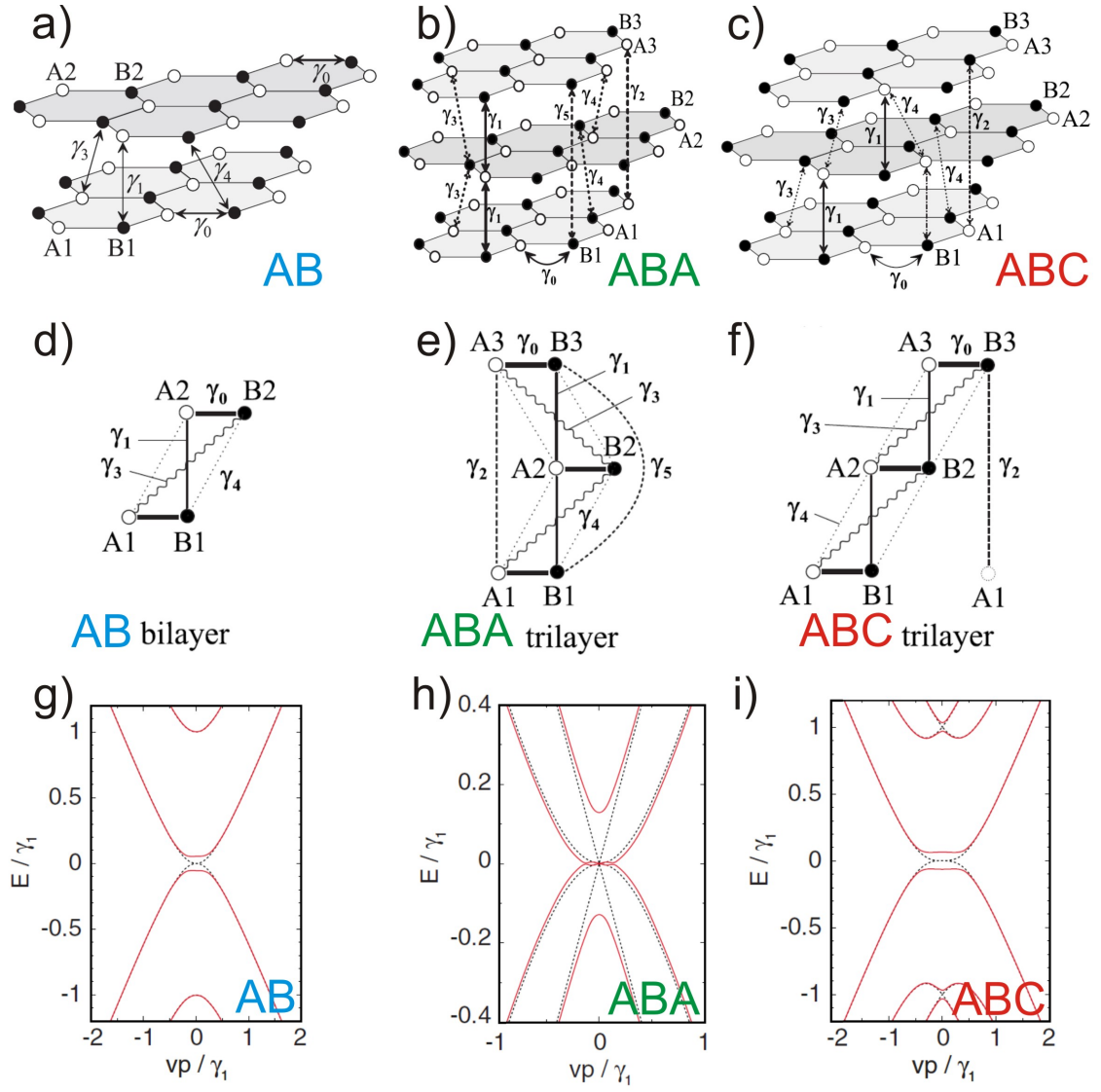

Figure 2.3: (a) Schematic of the bilayer lattice containing four sites in the unit cell: $A1$ (white circles) and $B1$ (black) in the bottom layer, and $A2$ (white) and $B2$ (black) in the top layer [3], where γ_0 - γ_5 are the Slonczewski-Weiss-McClure parameters describing the tight-binding couplings of bulk graphene. Schematic of the ABA-stacked (b) and the ABC-stacked (c) trilayer lattice containing six sites in the unit cell, A (white circles) and B (black circles) on each layer [4, 7]. Schematic of the unit cell of AB-stacked bilayer (d), ABA-stacked trilayer (e) and ABC-stacked trilayer (f) graphene [4]. Self-consistent band structures for AB-stacked bilayer (g), ABA-stacked trilayer (h) and ABC-stacked trilayer graphene (i) without (dotted, black) and with (solid, red) external field. The situation is realized in experiment with external top and bottom gate electrodes which are held at the opposite gate voltages with respect to the graphene, cf. [6].

Exploiting mirror reflection symmetry of the lattice in the plane of its central layer [Fig. 2.3(b)], we can perform a unitary transformation to a basis consisting of linear combinations of the atomic orbitals. Thus the Hamiltonian $\hat{H}_{ABA}$ consists of a 2×2 block H_m and a 4×4 block H_b on the diagonal, connected by a simple off-diagonal block D:

$$\hat{H}_{ABA} = \begin{pmatrix} H_m & D \\ D^\dagger & H_b \end{pmatrix}. \tag{2.5}$$

H_m is similar to the Hamiltonian of monolayer graphene and contributes two bands near zero energy. H_b is reminiscent of the Hamiltonian of bilayer graphene and gives two bands split away from zero energy $\pm\sqrt{2}\gamma_1$ and two bands near zero energy [7]. When the interlayer symmetry of ABA trilayer is broken, for instance by means of an external perpendicular electric field, this results in a *band overlap* between conduction and valence band, cf. Fig. 2.3(h). This is the opposite of the band gap opening induced by the interlayer symmetry breaking in bilayer graphene.

For the rhombohedral stacked (ABC) trilayer graphene we have again three layers of carbon with six atoms in the unit cell ($A1$, $B1$, $A2$, $B2$, $A3$, $B3$), see Fig. 2.3(c) and (f). The hopping within a layer is described by γ_0, the interlayer coupling by γ_1, γ_3, γ_4 and the next-nearest layer hopping by γ_2. The interlayer asymmetry is characterized by U_1, U_2 and U_3. The Hamiltonian for ABC- stacked trilayer can be written as:

$$\hat{H}_{ABC} = \begin{pmatrix} U_1 & \nu\pi^\dagger & \nu_4\pi^\dagger & \nu_3\pi & 0 & \gamma_2/2 \\ \nu\pi & U_1 & \gamma_1 & \nu_4\pi^\dagger & 0 & 0 \\ \nu_4\pi & \gamma_1 & U_2 & \nu\pi^\dagger & \nu_4\pi^\dagger & \nu_3\pi \\ \nu_3\pi^\dagger & \nu_4\pi & \nu\pi & U_2 & \gamma_1 & \nu_4\pi^\dagger \\ 0 & 0 & \nu_4\pi & \gamma_1 & U_3 & \nu\pi^\dagger \\ \gamma_2/2 & 0 & \nu_3\pi^\dagger & \nu_4\pi & \nu\pi & U_3 \end{pmatrix}. \tag{2.6}$$

To picture low-energy electronic properties of ABC-stacked trilayer graphene it is useful to derive an effective two-component Hamiltonian that describes hopping between atomic sites $A1$ and $B3$. The following two-component Hamiltonian can be found, following Ref. [4]:

$$\hat{H}_{ABC} = \frac{\nu^3}{\gamma_1^2}\begin{pmatrix} 0 & (\pi^\dagger)^3 \\ (\pi)^3 & 0 \end{pmatrix} + \hat{h_{3w}} + ... \tag{2.7}$$

The cubic term describes effective hopping between sites $A1$ and $B3$ via other sites on the lattice that are strongly coupled by γ_1. It yields a dispersion $\epsilon = \pm\nu^3 p^3/\gamma_1^2$. The term $\hat{h_{3w}}$ arises from the skewed interlayer coupling γ_3 and the next-nearest interlayer coupling γ_2 and is responsible for trigonal warping. Further terms correspond to other interlayer couplings introducing electron-hole asymmetry, interlayer asymmetries, etc., cf. Ref. [4]. Fig. 2.3(i) shows the schematic band structure of ABC trilayer graphene with and without an external electric field. The application of a perpendicular electric field *opens an energy band gap*.

The low-energy effective Hamiltonian for ABC-stacked trilayer graphene has some resemblance to that of bilayer graphene. The first term in those Hamiltonians describes chiral quasiparticles, whereas the degree of chirality is J=2 in bilayer and J=3 in ABC-stacked trilayer graphene and the quasi-particles acquire a corresponding

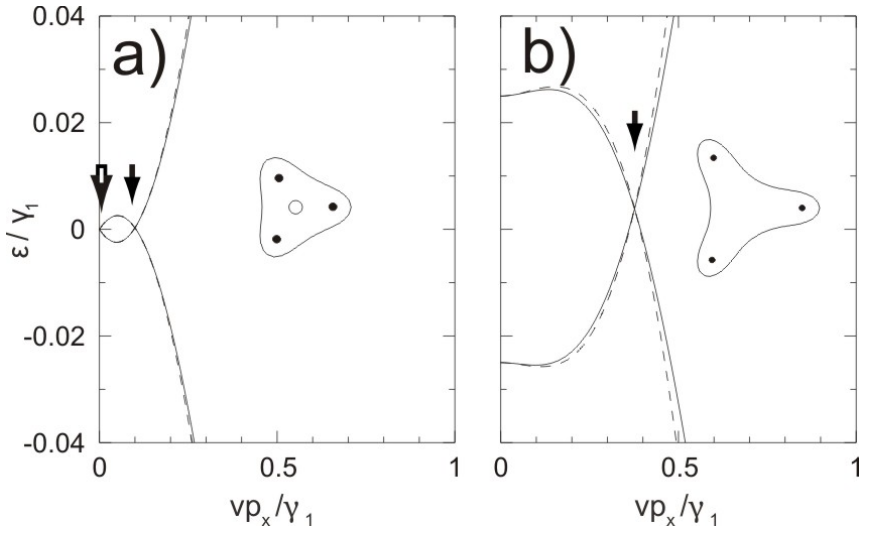

Figure 2.4: Low energy band structure of (a) bilayer and (b) *ABC*-stacked trilayer graphene. The solid and dashed curves represent the band structure using different approximations, cf. [4]. Insets show the equienergy lines at $\epsilon = 0.04\gamma_1$. The black and white arrows (circles in insets) represent Dirac points having Berry´s phase $\xi\pi$ and $-\xi\pi$, respectively. Adopted from [4].

Berry phase of $J\pi$. In addition in *ABC* trilayer graphene there is a trigonal warping effect, similar to the one in bilayer graphene, but more pronounced. The major difference to bilayer graphene is the contribution of the factor γ_2, so that the Lifshitz transition occurs at an energy of $\epsilon_L \approx |\gamma_2/2| \approx 10$ meV. At lower energies the equienergetic line around each valley is split into three leg pockets, but unlike in bilayer graphene the central pocket is missing. The different nature of the Lifshitz transition has its manifestation in the Berry phase. In bilayer the three leg pockets contribute $3\xi\pi$ and the central pocket $-\xi\pi$ leading to a Berry phase of $2\xi\pi$, whereas in *ABC* trilayer graphene each pocket contributes with $\xi\pi$ leading to Berry phase of $3\xi\pi$, compare figure 2.4.

2.2 Landau-Level Spectrum

When Dirac fermions in graphene travel in a perpendicular magnetic field, they experience a Lorentz force, which bends their trajectory. In the quantum regime, these cyclotron orbits give rise to discrete energy levels, the Landau levels (LL). The LL sequence reflects the nature of the charge carriers. The sequence for single layer graphene is very different to the one of conventional two-dimensional electron gases. The LL energy for single layer graphene in a perpendicular magnetic field B is given by $E_n \propto \sqrt{Bn}$, with integer n being the LL index. At zero energy the density of states shows $f = Jg = 4$-fold degenerate LLs [Fig. 2.5(c)], where $g = 4$ for the valley and spin degeneracy and $J = 1$ for single layer graphene with the Berry phase of $J\pi = 1\pi$.
For bilayer graphene the Landau-level energy is given by $E_n \propto B\sqrt{n(n-1)}$. At zero energy it shows $f = Jg = 8$-fold degenerate LLs, whereas $J = 2$ for bilayer graphene with the corresponding Berry phase of 2π [Fig. 2.5(c)]. The existence of f-fold degenerate zero-energy LLs explains the unusual sequence of quantum Hall

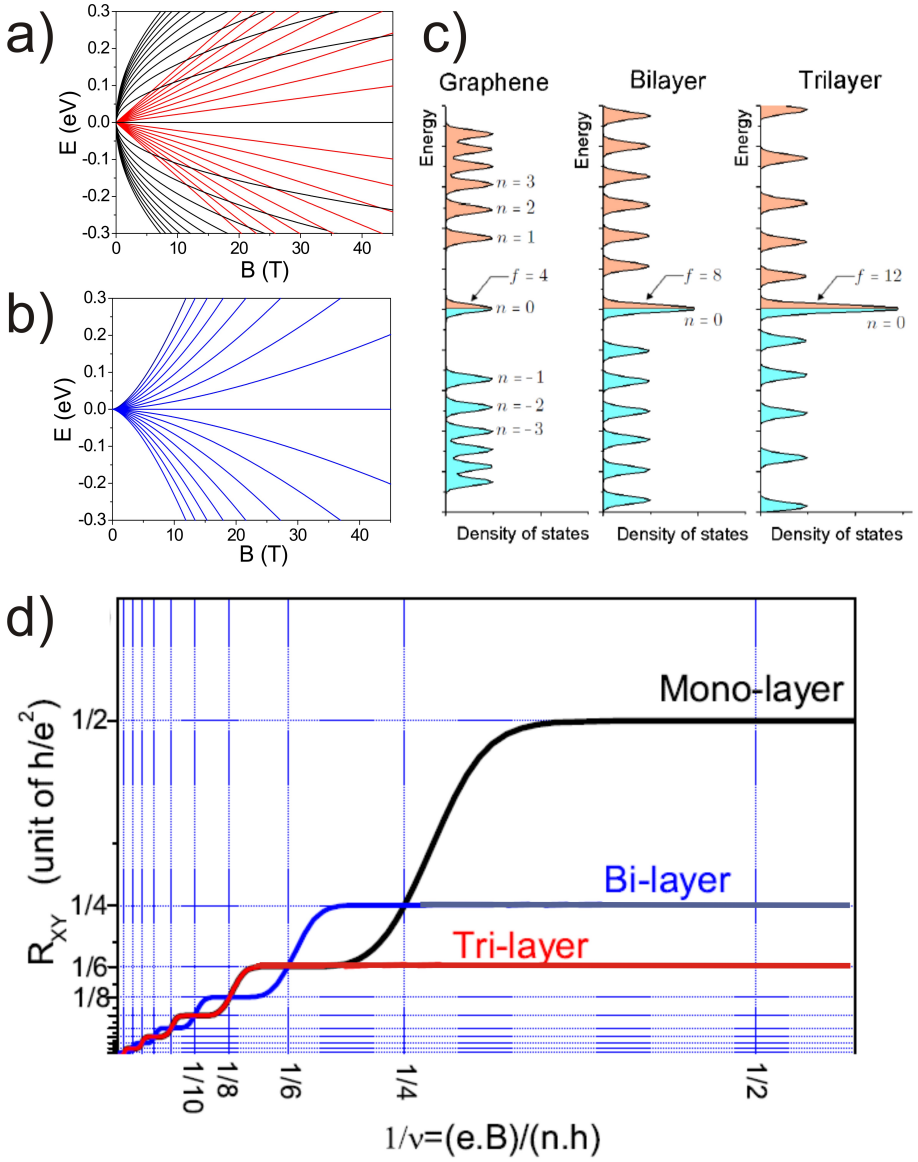

Figure 2.5:
(a) Landau level spectrum of *ABA*-stacked trilayer graphene. It can be seen as a superposition of monolayer-like and bilayer-like Landau levels. (b) Landau levels of ABC-stacked trilayer graphene [12]. (c) The density of states for single, bi- and trilayer graphene. The degeneracy of the zeroth Landau Level, equally shared by electrons and holes (blue and red), is 4-fold degenerate in single layer graphene, 8-fold degenerate in bilayer graphene and 12-fold degenerate in trilayer graphene [13]. (d) Quantum Hall Effect in single-, bi- and trilayer graphene [8, 13].

states observed at filling factor sequences $\nu = \pm 2, \pm 6, \pm 10...$ for monolayer [14, 15] and $\nu = \pm 4, \pm 8, \pm 12...$ for bilayer graphene [16], compare Fig. 2.5(d). The bilayer graphene is further distinguished from the gapless monolayer by a tunable energy gap, induced by breaking the inversion symmetry of the two layers in a perpendicular electric field [17–19].

In the simplest tight-binding model that includes only the nearest intra- and interlayer hopping parameters γ_0 and γ_1, the Landau level spectrum of the ABA trilayer can be seen as a superposition of $\sqrt{B}$-dependent monolayer-like LLs and B-dependent bilayer-like LLs [Fig. 2.5(a)]. On the other hand, LLs of the ABC trilayer are given by $E_n \propto B^{3/2}\sqrt{n(n-1)(n-2)}$ [Fig. 2.5(b)], with Berry phase 3π [20, 21]. Despite the substantial difference in the LL spectrum, 12-fold degenerate zero-energy LLs are expected to result in QHE plateaus at filling factor sequences $\nu = \pm 6, \pm 10, \pm 14...$ for the trilayer graphene independently of the stacking order [20–23], cf. Fig. 2.5(d). However, the lack of inversion symmetry in ABA trilayer may lead to broken valley degeneracy, while the valley degeneracy of LLs is always given in the inversion-symmetric ABC trilayer [23].

2.3 Graphene Nanoribbons

Graphene nanoribbons (GNR) can be considered as thin stripes of graphene. In contrast to (bulk) graphene, graphene nanoribbons exhibit a band gap, which is essential for semiconductor devices and make them a promising material system for future applications, like graphene transistors, tunnel barriers, single electron transistors and quantum dots [24]. This section gives a short overview of the theoretical predictions for transport properties and the state of the art of GNR experiments.

One of the most important issues in the patterning of graphene nanodevices is the control of the width. In order to have quantum confinement effects one should be able to produce widths of a few nanometers. To realize this, many different techniques are suggested, like a solution-phase derived method which produces sub-10 nm GNRs [25], chemical methods [26] or the unzipping of carbon nanotubes [27–29], etc. Beside this, GNRs can be patterned by standard electron beam lithography, which is a widely used method we also use for our devices, cf. Chap. 3.1 and 3.3. Herewith GNR widths of a few tens of nanometers can be produced.

In the theoretical studies of GNRs an important point is the exact edge structure [armchair or zigzag edges, see Fig.2.6(a) and (b)] [30]. For example, GNRs with zigzag edges feature localized edge states at the Fermi level, those with armchair edges do not. In case of armchair ribbons the ribbon width determines whether the system is metallic or insulating. The system is metallic when $N = 3M - 1$, where N is the number of dimer lines in the armchair ribbon and M an integer, else the system is isolating. For insulating ribbons, the direct gap decreases with increasing ribbon width and tends to zero in the limit of very large widths. Fig. 2.6(c) shows the band structure of an armchair GNR with a width of $N = 30$. For zigzag ribbons the highest valence band state and the lowest conduction band state are always

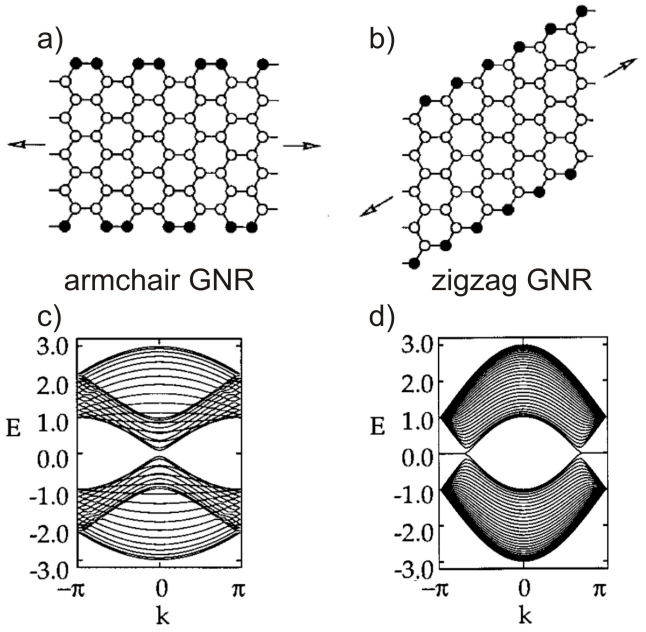

Figure 2.6:
(a) Schematics of an armchair and (b) a zigzag graphene nanoribbon. The edges are indicated by solid circles, the arrows indicate the translational directions of the GNRs. (c) Band structure of an armchair GNR and (d) a zigzag GNR. For the zigzag GNR a pair of almost flat bands appears within the region of $2\pi/3 \leq |k| \leq \pi$ where the bands sit in the very vicinity of the Fermi level. Graphics adopted from [30].

degenerated in the region of $2\pi/3 \leq |k| \leq \pi$, compare Fig. 2.6(d), where the band structure of a zigzag GNR with a width of $N = 30$ is shown. Here, N is the number of zigzag lines. While in theory a certain edge orientation of the nanoribbon determines the gap in the band structure as well as the transport properties, these models are not applicable for real devices. In experimentally studied graphene nanoribbons, which are e.g. lithographically produced, the edge roughness causes scattering, the fact that the ribbons lie on a silicon substrate adds disorder, etc. Therefore the properties of the sample and thus the characteristics of the gap, are not as simple as supposed theoretically. Several mechanisms have been suggested to explain the observed gap structure, ranging from Anderson localization to Coloumb blockade. For example, in Ref. [31] and [32] edge disorder is proposed to induce an energy gap due to Anderson-type localization. Others, e.g Ref. [33] and [34], state that the charge transport is dominated by the formation of quantum dots along the ribbon.

In early experiments Han *et al.* [35] studied lithographically patterned GNRs with different width and different crystollographic orientation. In conductance measurements, as a function of carrier density and temperature, they found that in the same crystallographic orientation the size of the gap strongly depends on the size of the ribbon: the gap scales inversely with the ribbon width, whereas it does not depend on the crystallographic orientation. This indicates that the detailed edge structure is more important than the overall crystallographic orientation and that the edge structure can not be controlled atomically sharp by a lithographic fabrication process.

Magneto-transport measurements might give further insight to the properties of the transport gap. Oostinga *et al.* [36] observed diamond-like structures while measuring the conductance as a function of gate and bias voltage, which is typical evidence of Coloumb blockade. This observation indicates that the electrons are confined in small regions in the ribbon. An irregular diamond pattern furthermore

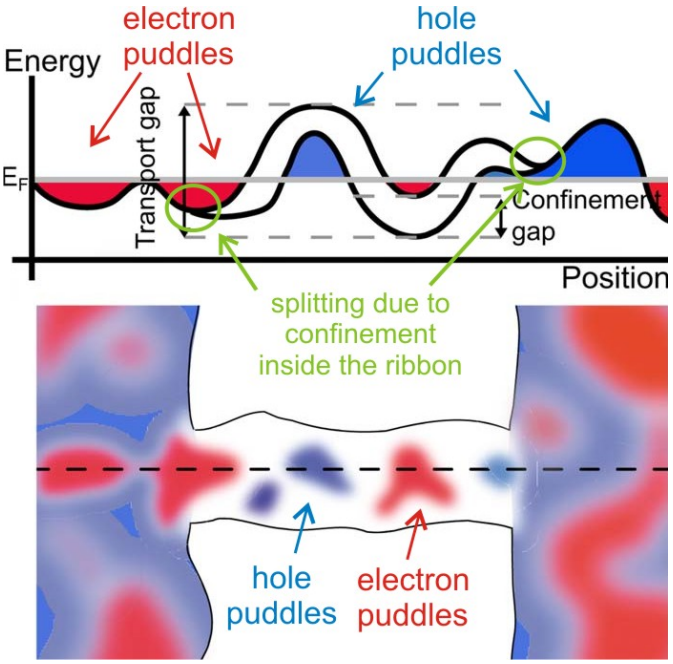

Figure 2.7:
Quantum dots forming along the graphene nanoribbon due to potential inhomogeneities and a confinement gap. The red puddles indicate electrons and the blue holes. The thick dark curves in the upper panel depict the energies of the conduction and the valence band as a function of position along the dashed line on the lower panel. The curve splits inside the ribbon due to the confinement gap (indicated by green circles). The transport gap can be identified as the amplitude of the disorder plus the confinement gap [33].

suggests that the confinement areas vary in size and that the electrons have to cross several of these areas while traversing the ribbon. Applying a magnetic field decreases the diamond size and thus increases the island size. Additionally, a positive magneto-conductance while applying a magnetic field, as well as the temperature dependence of the conductance in the transport gap, indicate that strong localization effects are present. Careful analysis of the measurements showed that only the opening of a gap alone can not explain the observations. Rather strong-localization effects caused by large disorder present in the ribbons influence the transport properties.

In contrast, Droescher *et al.* [34] state that the transport through the ribbon can completely be understood based on the mesoscopic details of the sample in a single-particle picture including Coulomb blockade and no further mechanisms are necessary to describe the observed behavior.

In Ref. [33] a nice cartoon depicting the gap structure along the ribbon is shown, see Fig. 2.7. Gallagher *et al.* state that the charge transport is dominated by the formation of quantum dots along the ribbon. The quantum dots form either due to lithographically induced edge roughness or potential inhomogeneities due to charged impurities near the ribbon and couple with (a smaller) confinement-induced gap. The confinement gap creates tunnel barrier regions of zero charge carrier density between the puddles. This is shown in Fig. 2.7: due to potential inhomogeneities areas of holes (*blue*) and electrons (*red*) form, which we call puddles. The confinement gap inside the ribbon, indicated by a splitting of the thick black line (indicated by *green* circles), separates those puddles creating quantum dots. In the experiments of Ref. [33] two distinct gaps were measured: As indicated in the upper panel of Fig. 2.7, a transport gap, which can be identified to have the amplitude of the disorder plus the confinement gap. Second, a source-drain gap, which roughly is the largest value of source-drain voltage for which the conductance is suppressed. The transport gap was

found to vary independently from the source-drain gap and the size of the transport gap is connected to the doping of the sample and thus to the disorder amplitude. The source-drain gap strongly depends on the impurity configuration.

As we saw in the experiments mentioned above, the transport behavior and the gap-structure of real devices is quite complicated. For future applications of graphene nanostructures it is necessary to study all the processes influencing the electronic transport in order to get information about the intrinsic sample properties and possible improvements of the sample fabrication.

3 Sample Preparation, Gate Coupling in Graphene Nanoribbons and Laboratories

In this chapter we will show the sample preparation of the different samples types. For the fabrication we used various clean room processes. In the following sections we give a short overview of the fabrication techniques. For further and more detailed information see appendix (Chap. 8).
In Sect. 3.1, we first present the sample preparation and the sample design of the GNRs and arrays of GNRs, which were measured on the one hand at the University of Regensburg in magnetic fields up to 16 T and on the other hand at the Dresden High Magnetic Field Laboratory in pulsed magnetic fields up to 60 T. For analysis of the transport measurements it is essential that the gate coupling of the GNR devices is enhanced compared to (sheet or array) graphene devices. This will be explained in Sect. 3.2. Third of all, the sample preparation of the trilayer graphene samples will be presented in Sect. 3.3. And in Sect. 3.4 the Dresden High Magnetic Field Laboratory will be introduced where those devices were measured.

3.1 Fabrication of Graphene Nanoribbons and Nanoribbon Arrays

At the Regensburg, University of Applied Sciences coordinate systems were patterned lithographically onto silicon wafers (with 300 nm SiO_2). This allows us in later processes to orientate on the sample and to localize and recover the graphene flakes. The spacing between the Cr/Au (5 nm/50 nm) alignment markers is 50 μm. Graphene is deposited on the silicon substrate by standard exfoliation technique with Scotch Tape, see for example Ref. [37]. Subsequently the single graphene flakes are detected under an optical microscope and their position with respect to the alignment marks is taken. Due to the grayscale contrast of the graphene flakes with respect to the background, the layer thickness of the flakes can be determined very fast and easily. Consequently one knows if it is single, bi-, tri- or multi-layer graphene. The GNRs and the arrays of GNRs are defined by electron-beam lithography (EBL) and oxygen plasma etching. The length of the ribbons is always 1 μm while the width W varies between 30 nm and 200 nm. In order to perform electron transport measurements, subsequently palladium contacts were patterned to the graphene samples by EBL and thermal evaporation. In Fig. 3.1 typical samples are illustrated: In the left image a graphene nanoribbon with graphene leads and palladium contacts is shown. The images on the right show a typical GNR array, whereas image (c) is a zoom-in of the

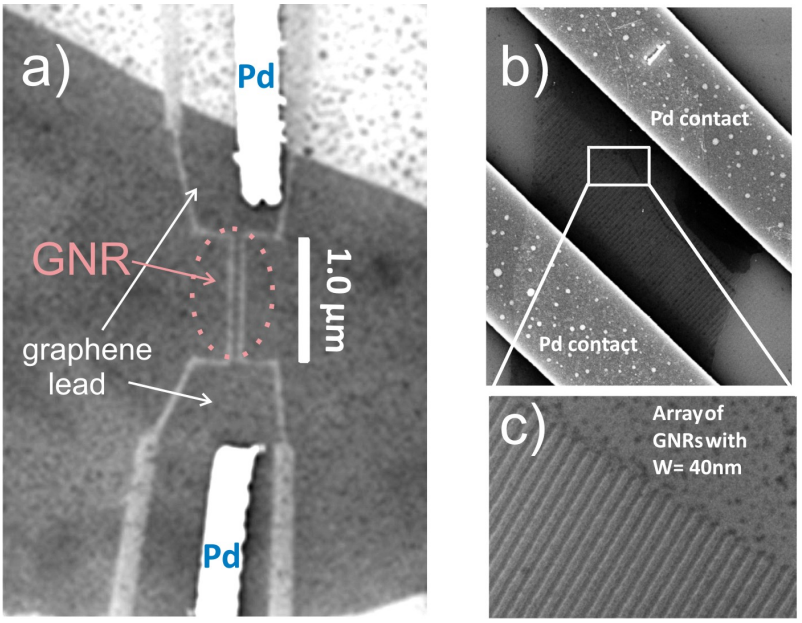

Figure 3.1: Scanning electron microscope images of typical samples. (a) Graphene nanoribbon (L= 1 μm, W= 70 nm) with two palladium contacts. (b) Array of GNRs between two palladium contacts. (c) Zoom-in of the GNR array, every GNR has a length of 1 μm, a width of 40 nm and a spacing of 30 nm to the next ribbon, the zoom-in area of image (b) is marked in white.

array of panel (b).
Achieving small ribbon widths as well as thin etched lines, which define the nanoribbon, is no straight forward process and thus a challenge for the fabrication. It has proved advantageous to fabricate many samples at once and to do an EBL test on bare silicon wafers before structuring graphene: Therefore the ribbon structures were patterned with different widths and dose values onto bare silicon substrates (without graphene) and after developing the resist $Au_{40}Pd_{60}$ was evaporated. The finished test samples were viewed under a scanning electron microscope and the dose value which shows the best results was utilized for the subsequent sample patterning on graphene.

For the measurements at the University of Regensburg, the samples were glued onto a 20-pin chip carrier with conductive silver [Fig. 3.4(a)] and subsequently bonded. The silicon dioxide was used as a back-gate and voltages up to 80 V could be applied. The characterization of the ribbons was done in different cryostats, with temperatures ranging from 1.7 K to 125 K in the He4-cryostat and between 20 mK and 900 mK in the dilution refrigerator, respectively. Transport measurements in two-terminal geometry (cf. Chap. 9.2) were performed in fields up to 16 T. For this, standard lock-in technique was used with frequencies of 13 Hz and 17 Hz, and currents of 10 nA for Kelvin-measurements and of 0.5 nA for mK-measurements, respectively.
For the measurements in pulsed fields at Dresden High Magnetic Field Laboratory no standard chip carriers were appropriate, because of a different probe design. Therefore special sample holders were fabricated, see Fig. 3.4(b - d). A documentation of the corresponding fabrication process is given in Chap. 3.3. After fabricating those special sample holders, the samples were glued onto them with conductive silver and subsequently bonded.
In order to prevent the samples from breaking during the transport to Dresden and the following assembling to the probe, special precautionary measures were done via bonding: first of all we connected the individual electrodes of the sample holder to

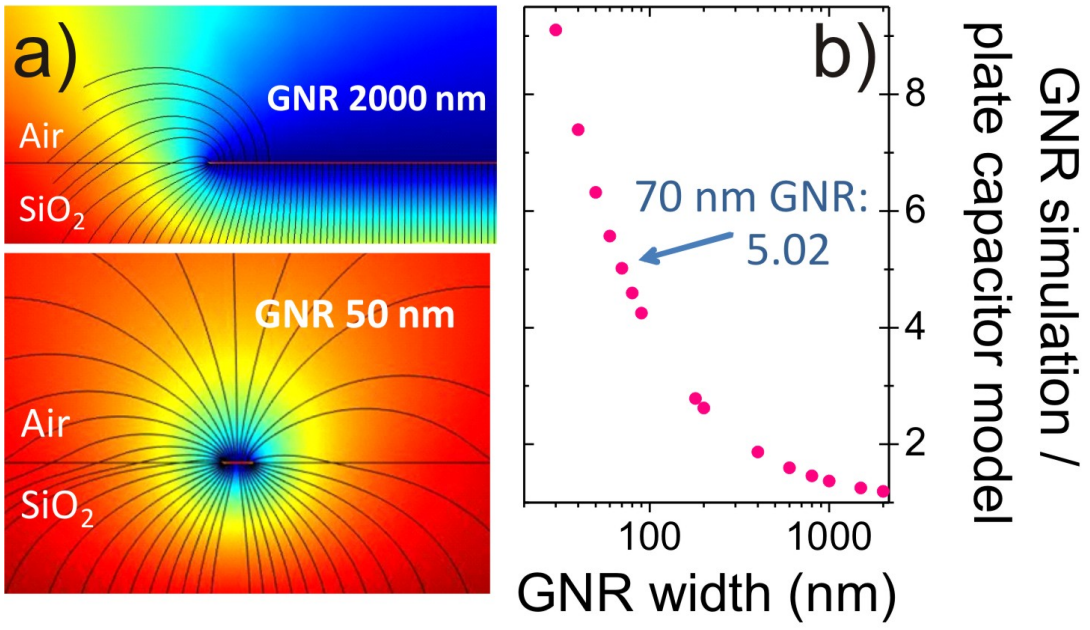

Figure 3.2: (a) Comsol simulation of GNRs with different width on SiO_2. The upper image shows the field line characteristics for a 2 μm GNR, the lower image for a 50 nm GNR. (b) Ratio between the gate coupling of a simulated GNR and the simple plate capacitor model depending on the GNR width.

each other via so-called security bonds. Only afterwards we connected the electrodes of the holder with the bondpads of the samples via aluminum bond wires. After transporting the samples to Dresden they were protected during mounting to the probe by the security bonds. Therefore the sample holders first were connected to the probes measurement lines by IC-pins, then the holder was glued onto a pod. Subsequently the security bonds were removed, and the pod was glued perpendicular to the probe. After testing the samples operability we could start the measurements.

3.2 Gate Coupling in Graphene Nanoribbons

In unpatterned, two-dimensional graphene the carrier density n can be determined with a simple parallel plate capacitor model, giving $n = 7.2 \cdot 10^{14}\mathrm{m}^{-2}\mathrm{V}^{-1} \cdot (V_{bg} - V_{CNP})$. Here, V_{CNP} is the back-gate voltage value of the charge neutrality point. However, the gate coupling C_g and consequently n strongly depends on the geometrical properties of the sample and for graphene nanoribbons the simple model can no longer be used. Rather we used the Comsol software, which is based on a finite-element-method, to determine the gate coupling. Since the GNRs simulated in 3D and in 2D showed similar results, we mainly performed the simulations in 2D, in order to reduce calculation time. The GNRs were simulated with the following parameters: the

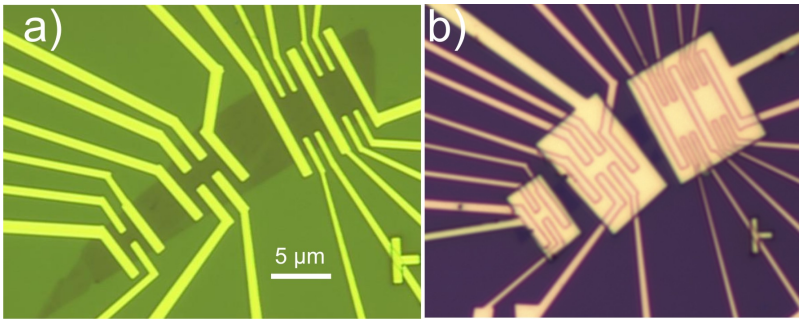

Figure 3.3: Optical images of a typical trilayer graphene device before (a) and after (b) top-gate deposition.

thickness of the graphene sheet was assumed as 1 nm, the width W of the GNR between 30 nm and 5 μm, the thickness of the SiO_2 300 nm, the thickness of the air 1.2 μm and the total system width 4.8 μm. Fig. 3.2(a) shows the field line characteristics for two ribbons of different width, simulated in 2D. In the upper image (2 μm ribbon) the field lines are almost perpendicular to the ribbon surface and only at the ribbon edge the density of the field lines is enhanced. The simple parallel plate capacitor model is still appropriate. Considering smaller ribbons, as shown in the lower image ($W = 50$ nm), the field line density and therefore the gate coupling is highly enhanced. Figure 3.2(b) summarizes the simulations for different GNR widths: it shows the ratio between the gate coupling of the simulated GNRs and the simple plate capacitor model depending on the sample width. For example, for a 70 nm wide ribbon one has to account a factor of 5.02 in comparison to the simple plate capacitor model. This results in a gate coupling $C_g = 576$ aF/μm^2 for graphene nanoribbons, in contrast to $C_g = 115$ aF/μm^2 for a (two-dimensional) graphene sheet or graphene nanoribbon arrays.

3.3 Fabrication of Trilayer Samples

The trilayer samples were fabricated mainly at the University of Tokyo by Shintaro Tokumitsu: Trilayer graphene was exfoliated onto silicon wafers with 285 nm silicon dioxide, which was used as a back-gate. Subsequently titanium/gold contacts and top-gates (SiO_2/Ti/Au) were defined by EBL. A typical sample is shown in Fig. 3.3. Further samples were fabricated in a similar fashion by Monica Craciun and Saverio Russo at the Centre for Graphene Science at the University of Exeter, England.
The patterned samples were characterized with Raman measurements by Monica Craciun at the Centre for Graphene Science (University of Exeter, England). There, on the one hand it can be verified that it indeed is trilayer graphene and on the other hand the stacking-order can be determined, see Chap. 6.1.

Afterwards the samples were sent to Regensburg, where they were scribed into appropriate pieces, glued into home-made sample holders by conductive silver and bonded. Similar to the nanoribbon samples, first security bonds were bonded between the single electrodes of the sample holder, followed by gold bonds between the electrodes of the holder and the bondpads of the sample.
The fabrication of the sample holder is analog to the one for the GNRs, only different printed circuit boards (PCB) were used, cf. Fig. 3.4(b).
The PCBs were fabricated in the electronic workshop at the University of Regensburg.

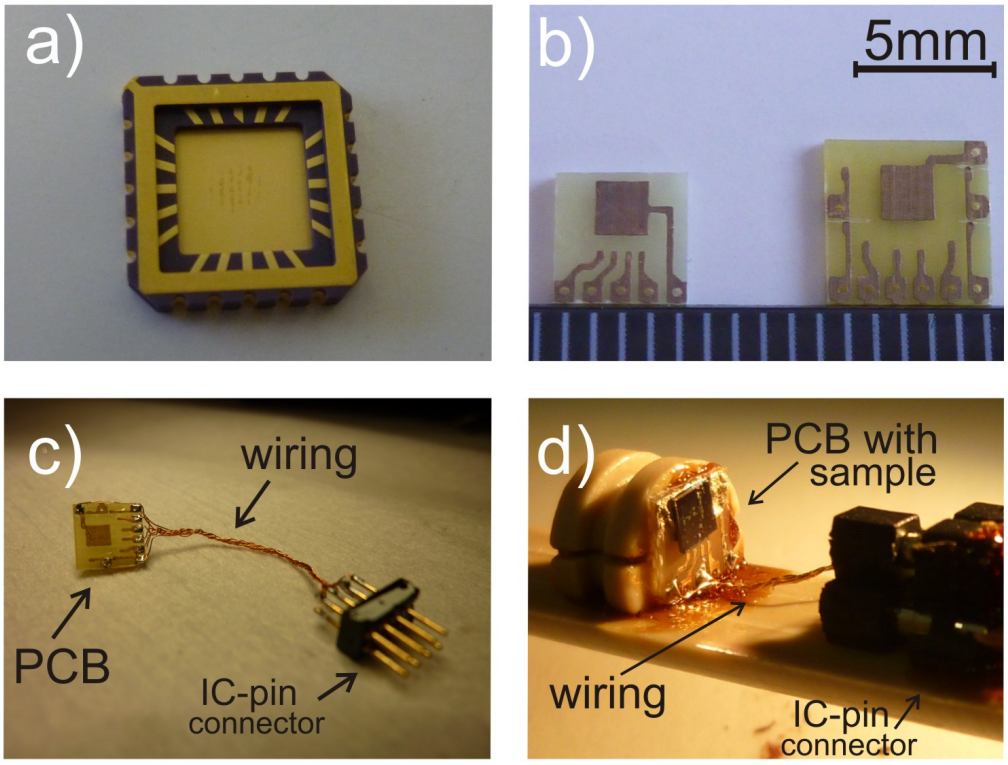

Figure 3.4: Sample holders: (a) Standard chip carrier, used for the measurements in Regensburg. For the measurements at Dresden High Magnetic Field Laboratory we fabricated special sample holders made of PCBs: (b) Left side: PCB for GNR samples, where 4 electrodes and one back-gate electrode are available. Right side: For the trilayer samples 7 electrodes, one top-gate electrode and one back-gate electrode are available. The fabrication of the trilayer and GNR sample holder in principle is the same: First of all copper wires are soldered to the electrodes, then we twisted those wires in order to avoid induction loops. After that we solder IC-pins to the wires in order to later connect the sample holder to the probe. Image (c) shows a finished trilayer sample holder. Subsequently the samples are glued to the holder by conductive silver, bonded and brought to Dresden. There the sample holder is connected to the measurement lines of the probe and glued perpendicular to the probe. Panel (d) shows a finished GNR device.

Before using them, they must be cleaned with acetone and propanol in order to remove residua of the fabrication process. Then copper wires are soldered to the electrodes of the PCB. Here one should use as few as possible soldering tin and soldering flux. Acetone and propanol are used to completely remove the soldering flux from the PCBs (else subsequent bonding is hardly possible). After that the wires were twisted in order to avoid induction loops and consequently to lower induced voltages during the magneto-transport measurements. Then IC-pins were soldered to the (other side of the) wires. This allows us later (after gluing the sample to the holder by conductive silver, bonding it and transferring it to Dresden) to connect the IC-pin-plug with the measurement lines of the probe in order to perform transport measurements. In Fig. 3.4(c, d) finished sample holders can be seen. The magneto-transport measurements were performed in pulsed, perpendicular magnetic fields up to 50 T. Typical pulse duration was 500 ms.

3.4 Dresden High Magnetic Field Laboratory

The Dresden High Magnetic Field Laboratory (HLD) [Fig. 3.5(a)] at the Helmholtz-Zentrum-Dresden-Rossendorf is one of four European user facilities (along with Grenoble, Toulouse and Nijmegen) for experiments in high magnetic fields. The access to the user facilities is coordinated in the EU project EuroMagNET II [38–40]. Since 2007 the HLD serves as a research facility for in-house projects as well as for national and international user projects. The coils available at the HLD produce both high magnetic fields (above 70 T with 150 ms pulse length) and smaller ones (60-65 T, with 25-50 ms lengths), see Fig. 3.5(b). In 2012, a record field close to 94.2 T has been reached. By now proposals for experiments up to 85 T are accepted. To achieve a field up to 100 T, an electromagnetic energy of 50 MJ and a peak current of 100 kA is needed. Therefore a pulse-discharge capacitor bank is used at the HLD [Fig. 3.6(a)]: The condenser system is composed of 20 modules, which provide energy from 0.9 to 2.9 MJ each.
Another excellent experimental possibility at the HLD is the free-electron lasers of the ELBE facility (Electron Linac for beams with high Brilliance and low Emittance) next to the magnetic field laboratory, which can be used in combination with high-field magnets and thus enables high-field magneto-optical experiments. In response to the large user demand, Dresden High Magnetic Field Laboratory is being extended till 2013. The construction of the extension building has already started, it will be equipped with a new capacitor bank and six additional magnet cells.

Our measurements were performed in the magnetic cells A and B, respectively. In Fig. 3.6(b) the magnetic cell A is shown, where the cryostat can be seen in the middle of the picture and above the beam-line set up for the free-electron lasers of the ELBE (which we did not use in our experiments). During our measurements, the grounding of the setup and the sample was essential in order to not destroy it during the preparations of the experiment. Therefore on the one hand security-bonds protected the sample during the assembling onto the probe, see Sect.3.1 and 3.3. And on the other hand a home-made switch-box was used, which allowed us to generally

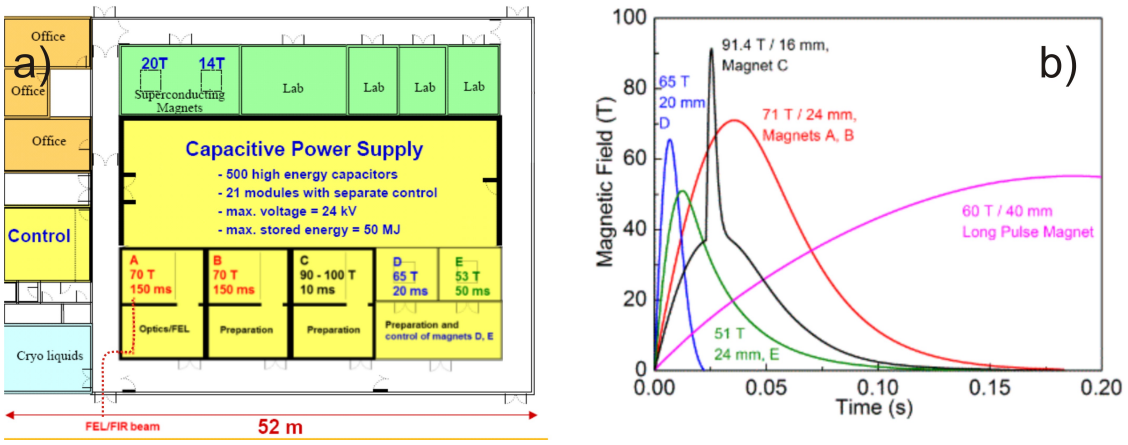

Figure 3.5: (a) Design of the Dresden High Magnetic Field Laboratory. (b) Pulse profiles of the magnets at the HLD. Four different magnets (A, B, D, E) are available for users [38].

ground the sample and to un-ground it during the experiments. The waiting-time between the measurements depends on the energy applied, the magnetic field, the pulse duration, just as well as on the coil design. In cell A the coil was designed as a fast-cooling system, whereas in the other cells not. Therefore we had to wait about 1.5 h for a 36 T pulse in cell A, and about 3 h in cell B, respectively. It is evident that, since we had quite long waiting-times between the measurements, the number of pulses during a measurement period (in our case mostly two weeks) is limited and one has to consider accurately a priori which measurements one wants to perform. In Fig. 3.6(c) the probe with the temperature sensor, the pick-ups and a mounted sample is shown. During the measurement the massive doors of all the cells [Fig. 3.6(d)] are closed for security and the experiment is operated from a control room. Both, the GNR and the trilayer DC magneto-transport measurements were done in perpendicular magnetic fields up to 60 T at temperatures between 1.8 K and 125 K and a DC bias of 10 mV. The two-terminal setup used for the measurements is schematically shown in Fig. 9.1. During the pulse the current through the sample was converted to a voltage signal by a current-to-voltage amplifier and recorded by a high-speed oscilloscope and data recorder.

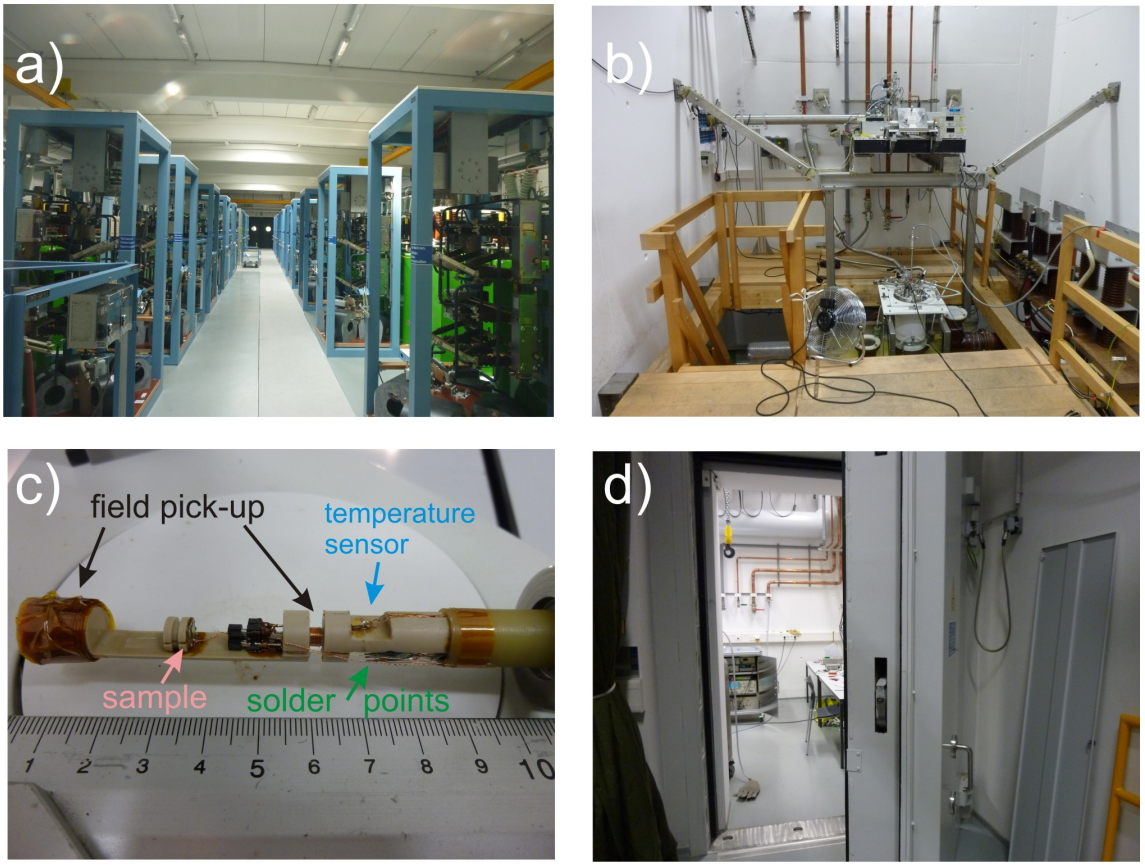

Figure 3.6: (a) Capacitor bank with 20 modules, which provide energy from 0.9 to 2.9 MJ each. (b) Magnetic cell A of the Dresden High Magnetic Field Laboratory. (c) Probe for the GNR and trilayer experiments with a sample mounted. (d) Massive security door of magnetic cell A.

4 Phase Coherent Transport in Graphene Nanoribbons and Nanoribbon Arrays

Phase coherent effects in graphene are determined by the combined action of several scattering mechanisms. In the past, extensive studies have been performed on those effects in bulk graphene [41–43]. Little attention, however, has been paid to phase coherent properties of graphene nanoribbons, where lateral confinement creates a crossover from 2D to 1D and additional scattering is introduced at the edges of the ribbons.

Here, we study the magnetotransport properties of graphene nanoribbons at low temperatures, focusing on interference effects which lead to resistance and accordingly to conductance corrections. In graphene nanoribbons edge scattering becomes the most important mechanism leading to the observation of weak localization. Another correction to the conductivity are universal conductance fluctuations (UCFs), which appear when the phase coherence length is comparable to the sample size. Both effects allow us to independently extract the phase coherence length L_φ.

4.1 Weak Localization

In the diffusive transport regime electrons can be scattered elastically (e.g. by charged impurities) or inelastically (e.g. electron-electron or electron-phonon scattering) on their way through the conductor. Elastically scattered electrons maintain their phase coherence information. The interference between pairs of time-reversed paths is constructive, because the paths are identical and the phase is the same. As a result, the probability that the electron scatters back is enhanced, leading to a decrease of the conductance. Such a coherent conductor is said to be in the regime of weak localization (WL). This effect is easily suppressed by small magnetic fields: a perpendicular magnetic field breaks time-reversal symmetry, adds a phase difference to the interfering carriers and thus destroys the constructive interference. This results in an increase of the conductance (positive magneto-conductance or rather negative magneto-resistance). Weak localization can be identified experimentally by measuring the magneto-resistance and can be used to determine the phase relaxation length. Instead, weak anti-localization (WAL) is observed in conductors with strong spin-orbit coupling, where the two paths meet in anti-phase because of spin-flips caused by scattering at impurities [44].

[0]The contents of this chapter are in preparation for publication, *Phase Coherent Transport in Graphene Nanoribbons and Graphene Nanoribbon Arrays*

In graphene weak localization is often suppressed and generally more complex than in diffusive metals [42, 43]. Due to the honeycomb lattice structure with two sublattices the charge carriers are chiral, that means that they have an additional quantum number, the pseudospin. The Berry phase adds a phase difference to the interfering trajectories, so that they meet in anti-phase and destructive interference occurs leading to a suppression of backscattering. This results in an increase of the conductance, thus displaying a weak anti-localization behavior.
However, the interference properties are strongly affected by the details of the electronic band structure and disorder which leads to either WL, WAL or total suppression of both [41, 45]. Consequently one has to account not only for the dephasing time τ_φ but also for the elastic scattering times (τ_i and τ_*). Defects of the size of the lattice spacing, dislocations and ripples can break the chirality or rather produce a random magnetic field which destroys the interference of electrons in one valley. These effects are described by $\tau_*^{-1} = \tau_w^{-1} + 2\tau_z^{-1} + \tau_i^{-1}$, with the intervalley scattering rate τ_i^{-1} (between the two valleys), the intravalley scattering rates τ_z^{-1} and τ_w^{-1}.
For **single layer graphene** the weak localization behavior can be described by [42]:

$$\frac{\Delta\rho(B)}{\rho^2} = -\frac{e^2}{\pi h}\left[F\left(\frac{B}{B_\varphi}\right) - F\left(\frac{B}{B_\varphi + 2B_i}\right) - 2F\left(\frac{B}{B_\varphi + B_*}\right)\right], \tag{4.1}$$

with $F(z) = \ln z + \psi\left(0.5 + z^{-1}\right)$, the digamma function ψ, $B_{\varphi,i,*} = \hbar/(4De)\cdot\tau_{\varphi,i,*}^{-1}$ and the diffusion coefficient D. The corresponding lengths are $L_{\varphi,i,*} = \sqrt{D\tau_{\varphi,i,*}}$. $\Delta\rho(B)$ is defined as $\Delta\rho(B) \equiv \delta\rho(B) - \delta\rho(0)$, with the sheet resistance $\rho = R\cdot W/L = W/GL$ and $\delta\rho(B)$ the WL correction to the graphene sheet resistance at a certain magnetic field B.
Negative magneto-conductance corresponds to anti-localization and is determined by the (negative) second and third terms in Eq. 4.1. In the absence of intra- and intervalley scattering ($\tau_{i,*} \to \infty$) the first and second term cancel and the resistivity correction is controlled by the third term. For strong intra- and intervalley scattering (τ_*, τ_i small), the first (positive) term dominates.

For **graphene nanoribbons**, however, the transverse diffusion time $(W^2/D) \ll \tau_i, \tau_*, \tau_\varphi$ and edge scattering is the most important mechanism leading to the observation of WL. The weak localization behavior can be described by [42]:

$$\frac{\Delta\rho(B)}{\rho^2} = \frac{2e^2 L_\varphi}{h}\left[\frac{1}{\sqrt{1 + \frac{1}{3}\frac{B^2}{B_\varphi B_\perp}}} - 1\right] = \frac{2e^2\sqrt{D}}{h}\left[\left(\frac{1}{\tau_\varphi} + \frac{1}{\tau_B}\right)^{-1/2} - \left(\frac{1}{\tau_\varphi}\right)^{-1/2}\right] \tag{4.2}$$

with $B_\perp = \hbar/eW^2$, $B_\varphi = \hbar/(De)\cdot\tau_\varphi^{-1}$ and $\tau_B = 3\hbar^2/(DW^2e^2B^2)$. Here, ρ is the resistance per unit length $\rho = R/L = 1/GL$. By fitting the magnetotransport data one can deduce the phase coherence length L_φ, whereas the first term describes the magnetic field dependent conductivity correction and the second term the WL-caused offset at zero field.

The magnetic field dependent term, namely

$$\frac{\delta\rho(B)}{\rho^2} = \frac{2e^2\sqrt{D}}{h}\left[\left(\frac{1}{\tau_\varphi}+\frac{1}{\tau_B}\right)^{-1/2}\right], \tag{4.3}$$

with $\delta\rho(B) = \Delta\rho(B) + \delta\rho(0)$, corresponds to the (standard) conductivity correction for a one-dimensional wire, cf. Ref. [44]. As generally known, e.g. the presence of spin-orbit interaction modifies the weak localization behavior and equation 4.3 needs to be expanded. This can be done by adding a spin-orbit relaxation factor, cf. Ref. [46], where this is shown for a one-dimensional wire.
In the same way we generalize Eq. 4.3 for graphene nanoribbons. Usually, the WL correction is described in terms of particle-particle correlation functions, so called "Cooperons". In two-dimensional graphene δg is determined by the interplay of one pseudospin singlet (C_0^0) and three triplet (C_0^x, C_0^y, C_0^z) Cooperons, $\delta g \propto -C_0^0 + C_0^z + C_0^x + C_0^y$ and their corresponding relaxation rates (cf. Ref. [42]). In summary this leads to Eq. 4.1. For graphene nanoribbons the four Cooperons C_0^x, C_0^y, C_0^z and C_0^0 need to be considered in a similar fashion. Therefore we have to include the contributions from one (intervalley) Cooperon C_0^z (with 2 τ_i^{-1}) and from two (intravalley) Cooperons C_0^x and C_0^y (with τ_*^{-1}). This leads to the following formula [47]:

$$\frac{\delta\rho(B)}{\rho^2} = \frac{2e^2\sqrt{D}}{h}\left[\left(\frac{1}{\tau_\varphi}+\frac{1}{\tau_B}\right)^{-1/2} - \left(\frac{1}{\tau_\varphi}+\frac{2}{\tau_i}+\frac{1}{\tau_B}\right)^{-1/2} - 2\left(\frac{1}{\tau_\varphi}+\frac{1}{\tau_*}+\frac{1}{\tau_B}\right)^{-1/2}\right], \tag{4.4}$$

Here all scattering terms relevant in two-dimensional graphene (τ_φ^{-1}, τ_B^{-1}, τ_i^{-1} and τ_*^{-1}) are included. It is important to note that weak localization is visible in samples whose dimensions are much larger than L_φ, whereas other interference phenomena, like the universal conductance fluctuations (Chap. 4.2), only appear in samples with a size $\sim L_\varphi$ and average out in larger samples. The averaging out of universal conductance fluctuations will be important in our experiments, especially at mK-temperatures.

4.2 Universal Conductance Fluctuations

The WL corrections to the *average* conductivity arise from the interference between pairs of time-reversed paths that return to their origin and the application of a magnetic field suppresses the interference and thus allows to determine L_φ by fitting the data to the theory. Another example for electron interference are the universal conductance fluctuations (UCF), which are *sample-specific*, reproducible fluctuations in the conductance that occur as a function of magnetic field, chemical potential or impurity configuration. UCFs, which are often called the *magneto-fingerprint* of the sample, arise from the interference between all of the possible paths the electron can take traversing the sample. Depending on the sample dimensionality, the magnitude and the magnetic-field dependence, the UCFs can be characterized by the thermal length $L_T = \sqrt{\hbar D/k_B T}$ with k_B the Boltzmann constant or the phase coherence length L_φ [48]. The amplitude of the UCFs is of the order of

$\Delta G_{rms} = \sqrt{var(G)} = \sqrt{\langle (G - \langle G \rangle)^2 \rangle} \approx e^2/h$ for zero temperature and $L_\varphi \geq L$, regardless of the size of the sample L and the degree of disorder. ΔG_{rms} is the *root-mean-square* conductance and $var(G)$ the conductance variance. For nonzero temperature, the magnitude of the UCFs is reduced below e^2/h due to a finite phase coherence length and thermal averaging. A large sample ($L > L_\varphi$) can be considered as an ensemble of many phase-coherent units ($N = L/L_\varphi$) and the phase coherence length can be calculated by the following expressions for 1D [44]:

For $L_\varphi \ll L_T$:

$$\Delta G_{rms} = C \frac{e^2}{h} \left(\frac{L_\varphi}{L} \right)^{3/2}, \tag{4.5}$$

for $L_\varphi \gg L_T$:

$$\Delta G_{rms} = C \frac{e^2}{h} \left(\frac{L_T L_\varphi^{1/2}}{L^{3/2}} \right), \tag{4.6}$$

and for $L_\varphi \approx L_T$:

$$\Delta G_{rms} = \frac{g_s g_v}{2} \beta^{-1/2} \sqrt{12} \frac{e^2}{h} \left(\frac{L_\varphi}{L} \right)^{3/2} \left[1 + \frac{9}{2\pi} \left(\frac{L_\varphi}{L_T} \right)^2 \right]^{-1/2}. \tag{4.7}$$

In those expressions C is a constant that depends on magnetic field and spin-orbit coupling. The parameter β is 1 at zero-magnetic field, where the time-reversal symmetry holds; $\beta = 2$ when time-reversal symmetry is broken by a magnetic field. The factor $g_s g_v$ assumes spin and valley degeneracy.
However, for graphene samples in the diffusive regime with weak disorder present, it was found that the variance $var(G)$ can take different universal values depending on the type of disorder [49, 50].

- When all scattering effects are negligible ($\gamma_\perp, \gamma_z, \gamma_w \ll \epsilon_x^*$) the variance is four times larger than in conventional metals, $\langle [\delta G]^2 \rangle = 4 \cdot \langle [\delta G]^2 \rangle_m$, where $\langle [\delta G]^2 \rangle_m$ is the conductance variance for a conventional metal. Here, $\gamma_\perp$ is the intervalley scattering, γ_z the intravalley scattering and γ_w the trigonal warping rate. $\epsilon_x^* = \pi^2 D/L_x$ is the Thouless energy for the dimension x and L_x the sample length.

- For weak intervalley scattering ($\gamma_\perp \ll \epsilon_x^*$) and either strong intravalley scattering or strong trigonal warping ($\gamma_z \gg \epsilon_x^*$ or $\gamma_w \gg \epsilon_x^*$) the variance is two times larger than in conventional metals, $\langle [\delta G]^2 \rangle = 2 \cdot \langle [\delta G]^2 \rangle_m$.

- For strong intervalley scattering ($\gamma_\perp \gg \epsilon_x^*$) and intravalley scattering or trigonal warping rates arbitrary compared to ϵ_x^*, the variance coincides with the one in conventional metals, $\langle [\delta G]^2 \rangle = \langle [\delta G]^2 \rangle_m$.

Although the UCF amplitude in graphene strongly depends on the details of electron scattering and thus differs from the one in other mesoscopic conductors, the analysis of the UCFs by the autocorrelation function (cf. text below) is independent of

such details and can for example be used for measuring the electron temperature in graphene devices [51]. The following section will introduce the autocorrelation function method with particular attention to the analysis of our measurements.

In experiments, one generally studies UCFs by changing the Fermi energy or the magnetic field, rather than by changing the impurity configuration. Employing the Ergodic hypothesis, a connection between fluctuations in magnetic field and energy can be found. The change in magnetic field B or energy E_F, by changing the gate voltage, is equivalent to ensemble averaging. A change on the order of the correlation field B_c or the correlation energy E_c, respectively, is equivalent to a change of the impurity configuration. The autocorrelation function $F_G(\Delta B)$ allows to identify the phase coherence length from the magnetotransport measurements. The magneto-autocorrelation function is given by [44]:

$$F_G(\Delta B) = \int_a^b dB\ G(B) \cdot G(B + \Delta B) \tag{4.8}$$

and B_c is determined by the width of this function at half maximum:

$$F_G(B_c) = 0.5 \cdot F_G(0), \tag{4.9}$$

as shown in Fig. 4.2(c). The correlation field B_c is the magnetic field, where a single flux quantum $\Phi_0 = h/e$ is enclosed by the maximum phase-coherent area A_φ: thus $B_c = C_1 \cdot \Phi_0/A_\varphi$, with $A_\varphi = L_\varphi^2$ for $L_\varphi \leq W$ and $A_\varphi = L_\varphi \cdot W$ for $L_\varphi \geq W$, with sample width W and a prefactor C_1. The prefactor C_1 ranges from 0.95 for $L_\varphi \gg L_T$ to 0.42 for $L_\varphi \ll L_T$ [44]. In our samples $L_\varphi \geq W$ and thus the phase coherence length L_φ can be extracted by:

$$L_\varphi = C_1 \cdot \frac{\Phi_0}{B_c W}. \tag{4.10}$$

The determination of L_φ by the autocorrelation function is limited by the finite magnetic field range available in experiment. It is only possible if the magnetic field range $B \gg B_c$.

4.3 Data Analysis

In the last sections different ways (WL and UCFs) to determine the phase coherence length were introduced. However, it is difficult to perform experiments, which allow the comparison of the L_φ determined by WL and the UCF theory, because experiments are carried out in small samples at low temperatures, where the conductance fluctuations mask the WL feature. In order to study WL also at mK-temperatures, we patterned both graphene nanoribbons and arrays of GNRs. At temperatures down to helium temperature WL as well as UCFs can be investigated in GNRs as well as in GNR arrays. At lower temperatures, as expected, the UCFs mask the WL feature in the individual ribbons. Then the GNR arrays enable us to still study weak

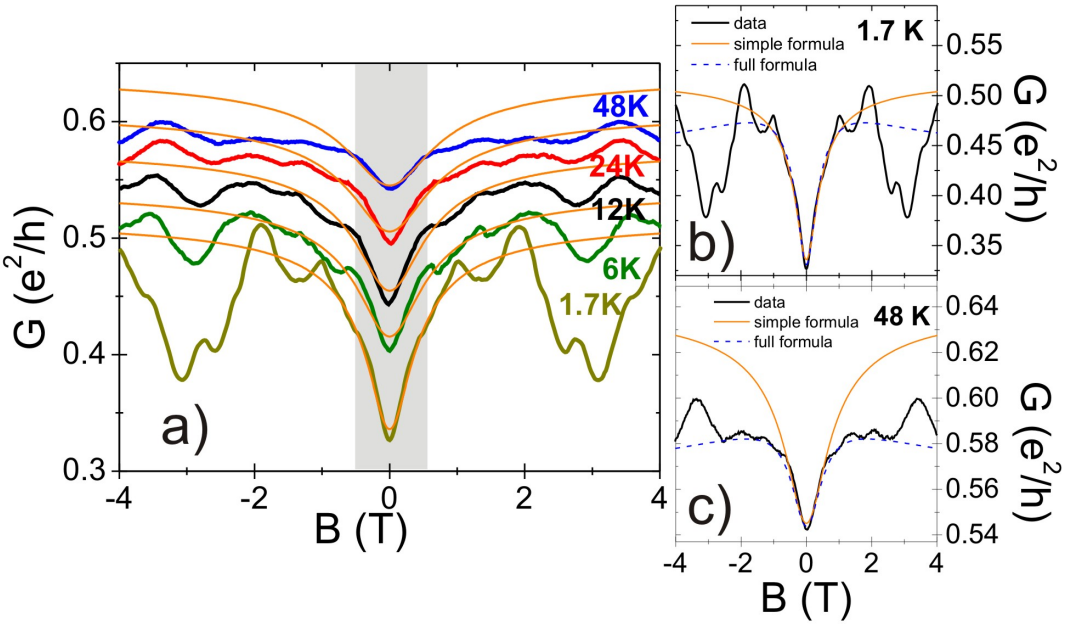

Figure 4.1: (a) Magneto-conductance of a 40 nm graphene nanoribbon (sample R1) at temperatures ranging from 1.7 K to 48 K. The gray shaded B-region highlights the magnetic field range of the WL feature, the *orange, solid* lines are fits using Eq. 4.3. The two right panels show the magneto-conductance at (b) 1.7 K and (c) 48 K. Corresponding fits to the simple (full) fit formula of the weak localization, are plotted as *orange, solid* (*blue, dashed*) lines.

localization: due to the parallel arrangement of the ribbons UCFs are suppressed by ensemble averaging, but WL is preserved.

For the analysis of the weak localization feature always the conductance per ribbon was analyzed. For the graphene nanoribbon arrays this means that the conductance measured for the device was scaled by the number of the ribbons. The magnetic field dependence of the conductance shows a dip at zero field, which corresponds to weak localization. As an example, in figure 4.1(a) the magneto-conductance of an individual 40 nm wide graphene nanoribbon is plotted for temperatures between 1.7 K and 48 K. For low temperatures one observes conductance fluctuations, but it is still possible to fit the WL feature to Eq. 4.3 (*orange solid* lines) and the phase coherence length can be extracted. Having a closer look at the individual fits, Fig. 4.1(b) and (c), one recognizes that at low temperatures the simple fit formula (Eq. 4.3) as well as the full fit formula (Eq. 4.4) reproduce the weak localization feature well [panel (b)]. However at higher temperatures [panel (c)], the fit to the full formula (*blue dashed* lines) reproduces the data much better than fits to the simple formula: While around zero field the fit works quite well, it overestimates the WL contribution at higher fields. Fitting the data to Eq. 4.4 reproduces the WL feature much better, the values of L_i were always about the ribbon width and L_* about a few ten nanometers. The determined phase coherence lengths do not differ too much: For example, at 1.7 K we get 91 nm by Eq. 4.3 and 99 nm by Eq. 4.4; at 48 K we get 48 nm by Eq. 4.3 and 54 nm by Eq. 4.4. Analogous to this example all samples introduced in

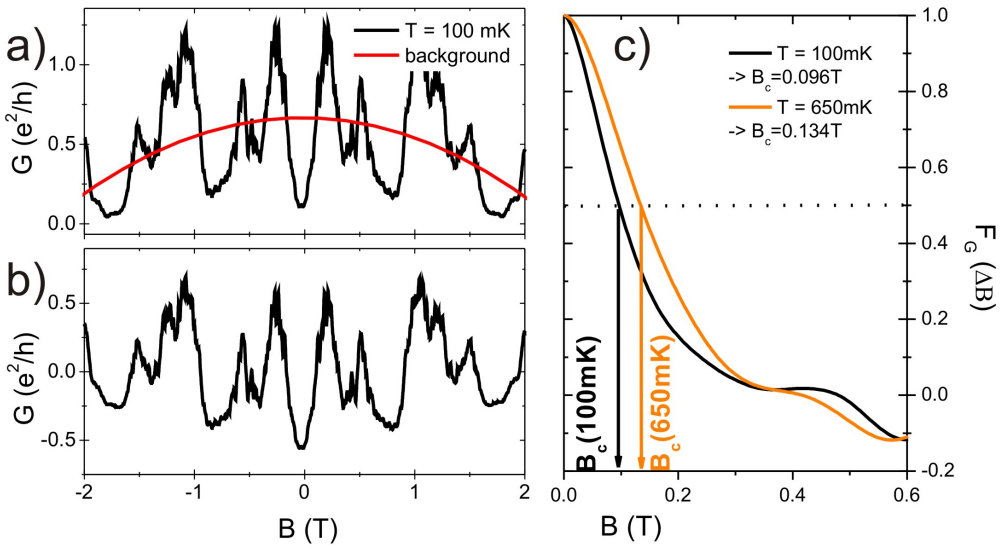

Figure 4.2: (a) Magneto-conductance of a 40 nm graphene nanoribbon (sample R1) at 100 mK. In order to analyze the universal conductance fluctuations one first has to remove the parabolic background (red). Data after background subtracted can be seen in (b). Panel (c) shows the autocorrelation function $F_G(\Delta B)$ for sample R1 at 100 mK (black) and 650 mK (orange), respectively. B_c is defined as the magnetic field value at the half maximum of the autocorrelation function.

the following sections were analyzed. The corresponding phase coherence lengths for different temperatures are summarized in $L_\varphi - T-$ diagrams, where the data points obtained by the simple fit formula (Eq. 4.3) are plotted as *black, open squares* (WL1) and the data points obtained by the full fit formula (Eq. 4.4) as *black, filled squares* (WL2). The results for this sample (R1) are summarized in Fig. 4.3.

In addition to the WL analysis, the magnetic field dependence of the universal conductance fluctuations was examined. The theoretical background for this is explained in chapter 4.2 and the method to determine the phase coherence length will be explained on a specific example, see Figure 4.2 (a). Afterwards, this method will be applied to the measured data and the results will be discussed in detail for all samples. In order to analyze the UCFs, first a parabolic background[1] has to be subtracted. The resulting conductance fluctuations are shown in Fig. 4.2 (b). For further analysis, parameters like the root-mean-square conductance[2] ΔG_{rms} or the autocorrelation function $F_G(\Delta B)$ need to be calculated. Those parameters

[1] Due to the measurement of the magneto-resistance in two-terminal configuration in GNRs a parabolic background has to be subtracted.

[2] Often the term root-mean-square (RMS) is used as a synonym for standard deviation (SD) when referring to the square root of the mean squared deviation of a signal from a given baseline or fit [52]. But in general the standard deviation and RMS are equal only when there is no DC component, i.e. zero mean value. In our measurements, the UCFs were analyzed after subtracting a background, thus the SD value can be used for further analysis and the calculated values are labeled as SD in the $L_\varphi - T-$ diagrams.

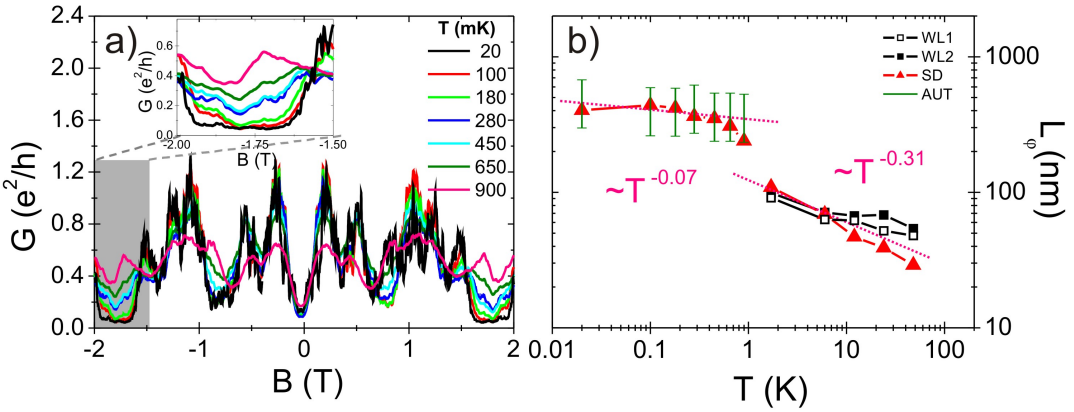

Figure 4.3: Individual GNR, sample R1. (a) Magnetoconductance of the sample at temperatures ranging from 20 mK to 900 mK. The zoom into the gray shaded region clearly shows that the amplitude of the UCFs increases with decreasing temperature. In (b) the phase coherence length L_φ was determined by different methods like weak localization (WL1 and WL2), the amplitude of the UCFs (SD) and the autocorrelation function (AUT). The data points obtained by fitting the WL feature to the simple formula (Eq. 4.3) are plotted as *black, open squares* (WL1) and by fitting the full formula (Eq. 4.4) as *black, filled squares* (WL2), respectively. The pink, dashed lines are fits of the temperature dependence of L_φ.

and functions, respectively, are directly connected to the phase coherent transport properties of the sample:

- Using Eq. 4.5 one can directly deduce L_φ from the root-mean-square conductance for our samples, whereas the constant C was set to 1. The obtained L_φ values are plotted as *red triangles* (SD) into the $L_\varphi - T-$ diagrams.

- By the autocorrelation function one can determine the correlation field B_c. It is defined as the magnetic field value at half maximum of the correlation function. The correlation field allows us to calculate the phase coherence length via equation 4.10. Since the prefactor C_1 has a value between 0.42 and 0.95 the corresponding range of L_φ is marked by *green error bars* (AUT) in the $L_\varphi - T-$ diagrams.

An example for the extraction of B_c from $F_G(\Delta B)$ for two different temperatures is given in Fig. 4.2(c). In the following sections both analysis methods of the UCFs (SD and AUT) will be used and compared to the values of L_φ extracted by weak localization (WL). Details and images of all the samples shown in the next sections can be found in Chap. 9.

4.3.1 Individual Graphene Nanoribbons

Figure 4.1(a) displays the magnetotransport data collected from a 40 nm wide individual GNR (**sample R1**, W= 40 nm) at temperatures ranging from T = 1.7 K to 48 K. Weak localization, for the low field region ($|B$ <1.5 T$|$) and universal conductance fluctuations are observed. The WL dips can be fitted with Eq. 4.3

and 4.4 (cf. Fig. 4.1) and a phase coherence length L_φ between 50 nm and 100 nm can be extracted. With decreasing temperature the amplitude of the oscillations increases and large universal conductance fluctuations are superimposed on the weak localization feature. This can be seen very clearly in Fig. 4.3(a). Consequently the phase coherence length can no longer be determined by fitting the weak localization. However, as discussed before, analyzing the UCFs allows us to determine L_φ: For temperatures between 20 mK and 900 mK the autocorrelation function leads to a phase coherence length between 680 nm and 230 nm. Analyzing the amplitude of the UCFs gives a L_φ of 440 nm to 240 nm for temperatures between 20 mK and 900 mK and of 110 nm to 30 nm for temperatures between 1.7 K and 48 K, respectively. These results are summarized in figure 4.3(b). The crossover from the Kelvin to the millikelvin temperatures, where the measurements were performed in different cryostats, is appropriate. Different methods yield similar values for L_φ: e.g. L_φ extracted by WL and by the amplitude of the UCFs at Kelvin temperatures, or the amplitude of the UCFs and the autocorrelation function at mK-temperatures. In summary, the extracted phase coherence lengths for sample R1, between 30 nm and 680 nm, clearly exceed the ribbon width. For the Kelvin temperatures a T-dependence of $\sim T^{-0.31}$ is observed, whereas it is much less for mK-temperatures ($\sim T^{-0.07}$) suggesting a saturating behavior of L_φ at low temperatures.

For the samples from the first generation, namely R1, R3 and R4, n++ doped silicon substrates were used. In most of the samples however, due to insufficient doping, its functionality as a back-gate could not be utilized. In order to be able to use the substrate as a back-gate down to very low temperature another substrate with higher doping (p++) was used, those samples are denominated as R2, R5 and A1 - A5. For example, **sample R2** (W= 40 nm) was analyzed at mK-temperatures: Like in the previous sample very prominent UCFs characterize the magnetic field dependence of the conductance, cf. Fig. 4.4(a). In addition to the analysis methods introduced previously, we could perform gate-averaging in order to obtain further information. To this end, the magnetic field dependence of the conductance was measured at different gate-voltages V_{bg} ranging from -40 V to -20 V in steps of 1 V (at T= 20mK) and the arithmetic mean was calculated. The resulting graph can be seen in Fig. 4.4(b): the average conductance clearly shows a dip at zero magnetic field. Fitting the weak localization feature one obtains a phase coherence length of about 100 nm, for both fit formulas (Eq. 4.3 and 4.4).
Furthermore, the gate dependence of the UCFs was measured at different temperatures, Fig. 4.4(c). Similar to the analysis of the magnetic field dependence of the universal conductance fluctuations [Fig. 4.2(a, b)], the background was subtracted from the measured data [Fig. 4.4(d)], the root-mean-square conductance ΔG_{rms} was calculated and the phase coherence length was determined by Eq. 4.5.
Figures 4.4(e) and (f) summarize the obtained results: determining the phase coherence length by the autocorrelation function leads to values between 100 nm and 500 nm. Analyzing the UCF amplitude, a phase coherence length of 170 nm $\leq L_\varphi \leq$ 270 nm was obtained from the magnetic field dependence and of 150 nm $\leq L_\varphi \leq$ 315 nm from the back-gate dependence, respectively. The temperature dependence of L_φ is shown in Fig. 4.4(f), the values extracted from the UCF amplitude in

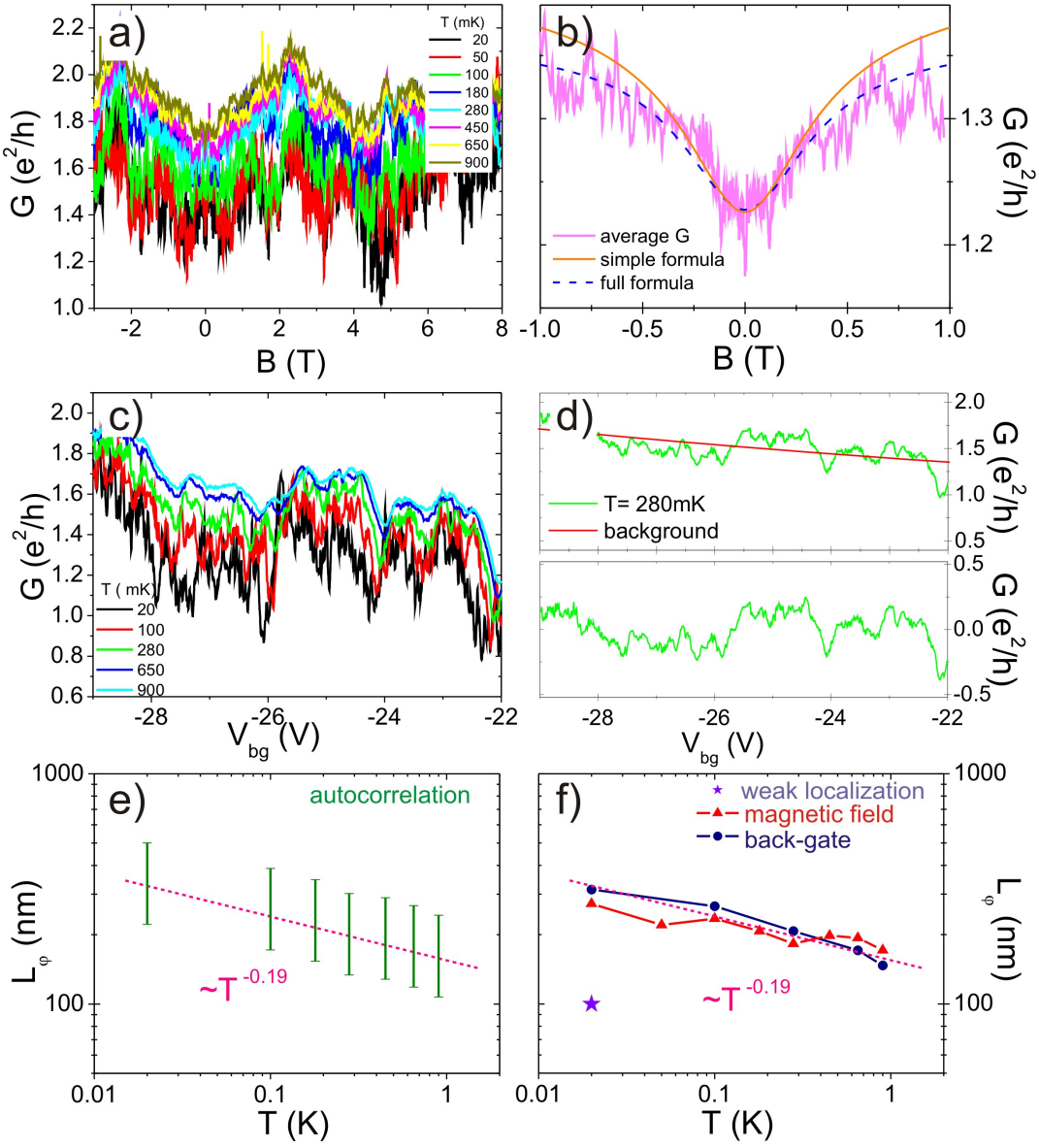

Figure 4.4: Individual GNR: sample R2 (W= 40 nm). Magneto-conductance of the sample at temperatures ranging from 20 mK to 900 mK (a). UCFs are very prominent and are superimposed on the WL feature. (b) Averaged magneto-conductance at T= 20 mK. The average was taken over 21 magneto-conductance traces at different gate voltages (V_{bg}= -40V...-20V, 1V steps) The averaged conductance shows a WL feature which was fitted with Eq. 4.3 (*orange, solid* line) and with Eq. 4.4 (*blue, dashed* line), respectively. Both fits yield a phase coherence length of about 100 nm. (c) Gate-dependent conductance fluctuations for different temperatures ranging from 20 mK to 900 mK. (d) Analysis of the UCFs shown for the 280 mK trace. Upper panel: Gate-dependence of the conductance at 280 mK with background. Lower panel: conductance fluctuations with subtracted background. (e) L_φ as a function of temperature determined via autocorrelation, and (f) L_φ as a function of temperature determined via the rms-amplitude ΔG_{rms} of the conductance fluctuations in magnetic field (*red*) and gate-voltage (*blue*), respectively. Additionally the value of L_φ for 20 mK extracted by averaging [cf. panel (b)] is shown (*purple star*). The pink, dashed lines are fits of the temperature dependence of L_φ.

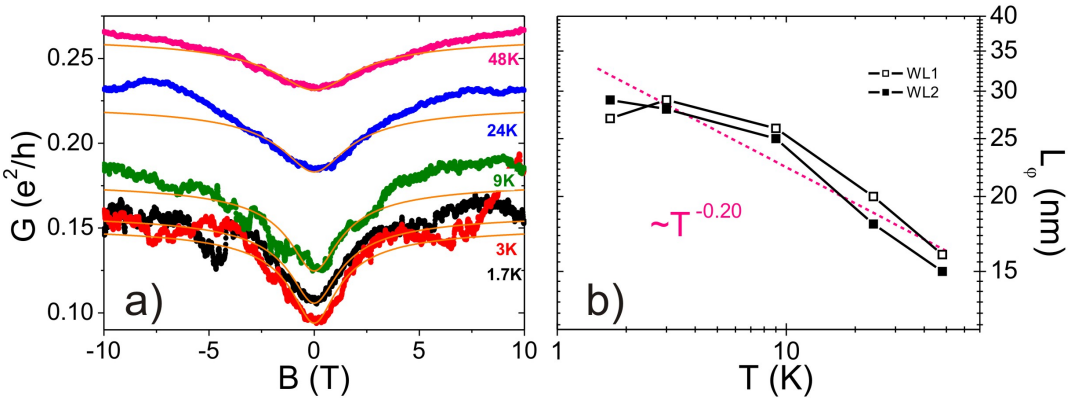

Figure 4.5: Individual GNR: sample R5. Magnetoconductance of the sample at temperatures ranging from 1.7 K to 48 K (a). In (b) the phase coherence length L_φ was determined by fitting the weak localization feature (WL). The pink, dashed line is a fit of the temperature dependence of L_φ.

magnetic field are *red* and from the UCF amplitude in gate-voltage in *blue*, respectively. The values of L_φ deduced from $\Delta G_{rms}(V_{bg})$ and $\Delta G_{rms}(B)$, match almost exactly. The pink dashed line corresponds to a temperature dependence proportional to $T^{-0.19}$. Comparing this to panel (e) it is noticed that the absolute values of L_φ extracted by autocorrelation and by ΔG_{rms} matches very well. Compared to the value of L_φ obtained by the fitting the WL feature of the averaged data [*purple star*, panel (f)], they are slightly higher.

Further samples yield similar values for L_φ, details are summarized in the appendix in Chap. 9.2: For **sample R3** (W= 40 nm) phase coherence lengths between 150 nm and 50 nm were found for temperatures between 1.7 K and 48 K. Similarly in **sample R4** (W= 40 nm), 95 nm $\leq L_\varphi \leq$ 650 nm for temperatures between 48 K and 1.7 K, where L_φ was determined by different methods. And for temperatures between 900 mK and 20 mK one obtains phase coherence lengths between 370 nm and 1100 nm via autocorrelation and 360 nm $\leq L_\varphi \leq$ 480 nm via the UCF amplitude. In summary, for most graphene nanoribbon devices phase coherence lengths between a few hundred nanometers up to about 1 μm at mK-temperatures can be observed and thus L_φ clearly exceeds the ribbon width. However, a few samples with much lower L_φ were measured and will be discussed shortly for completeness, cf. Fig. 4.5 (**sample R5**, W= 40 nm). As one can see in panel (a) the WL feature is very broad in magnetic field. Fitting the WL feature with Eq. 4.3 or Eq. 4.4 can reproduce the measured traces appropriately and leads to a phase coherence length between 15 nm and 30 nm for temperatures between 48 K and 1.7 K [panel (b)]. However, the reason why we observe such small phase coherence lengths on a few samples is unclear: the sample fabrication process was the same and no obvious difference can be found at least in the scanning electron microscope images. A possible reason might be that the graphene quality was worse[3]. Still the temperature dependence of L_φ is similar to the one of samples with larger phase coherence lengths ($\sim T^{-0.20}$).

[3]The low sample mobility, cf. table 9.1, suggest a bad sample quality.

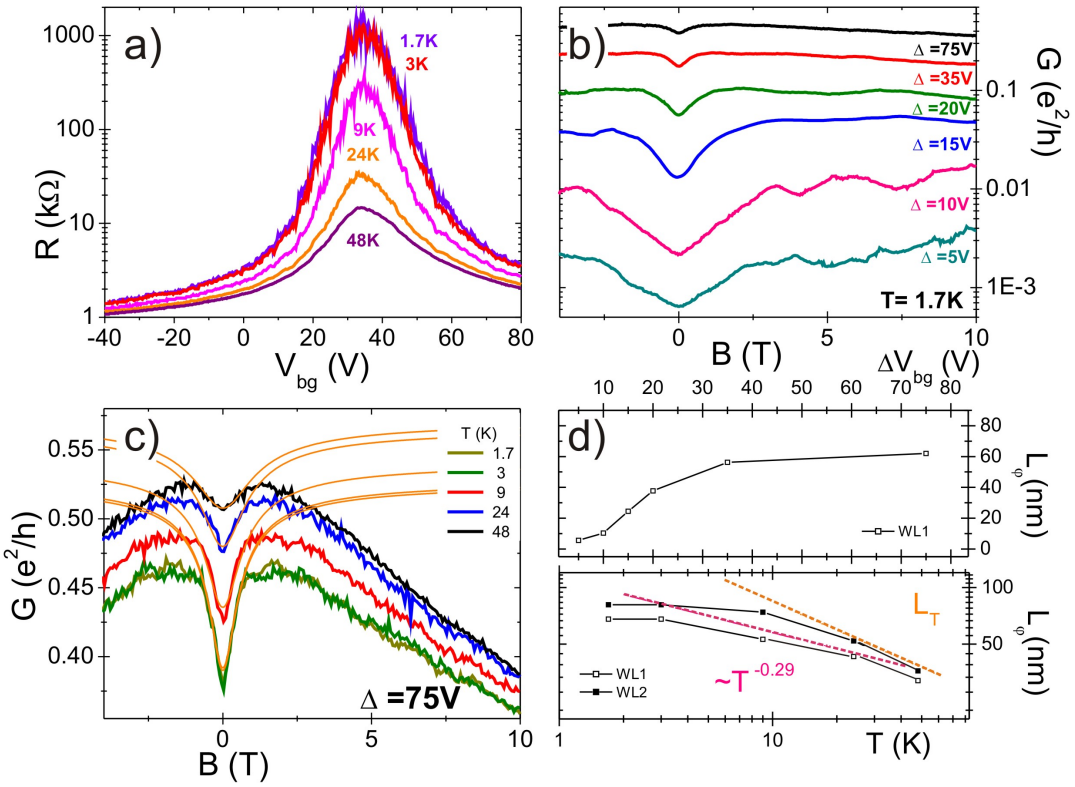

Figure 4.6: Array of 46 GNRs: sample A1. (a) Gate dependence of the resistance of the whole array at different temperatures ranging from 1.7 K to 48 K. (b) Magnetoconductance per ribbon for different carrier densities at 1.7 K. (c) Magnetoconductance per ribbon at temperatures ranging from 1.7 K to 48 K and Δ= 75 V away from the charge neutrality point. In (d) the phase coherence length L_φ was determined by fitting the weak localization feature (WL) of the data shown in panel (b, c). The pink, dashed line is a fit of the temperature dependence of L_φ. The orange, dashed line corresponds to the thermal length L_T.

4.3.2 Graphene Nanoribbon Arrays

In order to (better) observe the weak localization feature at mK-temperature, arrays of graphene nanoribbons were fabricated. As expected, the parallel arrangement of the nanoribbons leads to a suppression of the universal conductance fluctuations via ensemble averaging, whereas weak localization is not suppressed. Thus the phase coherent effects can be separated and again fitting Eq. 4.3 and 4.4 can be used to extract the phase coherence length.

Fig. 4.6(a) shows the back-gate dependence of the resistance of the whole GNR array of **sample A1** (W_{GNR}= 40 nm) at different temperatures, the charge neutrality point is located at around +35 V and the sample mobility can be calculated to 680 cm^2/Vs. In figure 4.6(b) the magnetoconductance per ribbon is shown for different carrier densities at 1.7 K. The array ensemble averaging (over 46 ribbons) obviously suppresses the UCFs and the WL feature is clearly observed. Furthermore one notices that the WL feature gets smaller - and thus the phase coherence lengths get larger - for larger gate voltage values $\Delta = |V_{bg} - V_{CNP}|$ away from the Dirac

point. Fitting the WL feature to Eq. 4.3, phase coherence lengths between 6 nm[4] and 62 nm are determined for gate voltage values Δ between 5 V and 75 V [panel (d), upper graph]. In order to determine the temperature dependence of L_φ, the magneto-conductance per ribbon was measured for temperatures ranging from 1.7 K to 48 K at Δ= 75 V, as shown in Fig. 4.6(c). Fitting the conductance dip one obtains phase coherence lengths between 80 nm and 30 nm [panel (d), lower graph], following a temperature dependence of $\sim T^{-0.29}$. The values of L_φ are very similar to those determined for individual ribbons at Kelvin temperatures, compare e.g. Fig. 4.3(b). Also the T-dependence of L_φ is the same. The similarity of the results approves that ensemble-averaging is an appropriate method to uncover the weak localization behavior of the sample and thus to determine the phase coherent properties of the sample.

At Kelvin temperatures, further samples yield similar values for L_φ. Like in GNR samples, a few arrays with much lower values of L_φ were measured and are mentioned here for completeness. The WL feature of **sample A2**[5], W_{GNR}= 30 nm, is very broad in magnetic field (see Chap. 9.2, Fig. 9.10). In panel (c) the magneto-conductance of the sample is shown at Δ = 60 V. Fitting the data with Eq. 4.3 and 4.4 can reproduce the data and leads to phase coherence lengths between 8 nm and 18 nm. Consequently, for individual as well as for arrays of GNRs devices with very small L_φ were observed. The origin of this is unclear, but at least they were found in both sample layouts, namely in individual ribbons and in arrays of GNRs.

Sample A3 and **sample A4** (both W_{GNR}= 80 nm) were analyzed at mK-temperature. Array A3 contains 23 and array A4 32 ribbons, in both arrays the width of the ribbons was 80 nm and the length 1 μm, sample images can be found in Fig. 9.4. The charge neutrality point for array A3 (A4) is about $V_{CNP} \approx$ +40 V (+20 V) and the sample mobility can be calculated to 500 cm^2/Vs (240 cm^2/Vs). Fig. 4.7(a) and Fig. 4.7(c), respectively, show the magneto-conductance per ribbon of the array A3 and A4 at temperatures ranging from 20 mK to 900 mK at V_{bg} = -20 V. Again the data was fitted by Eq. 4.3 and Eq. 4.4 and L_φ was determined. As already observed in sample A1, the phase coherence length slightly increases for increasing gate voltage values $\Delta = |V_{bg} - V_{CNP}|$, e.g. from about 60 nm to 100 nm for Δ from 20 V to 60 V at 280 mK [Fig. 4.7(e), fitting Eq. 4.3]. Whereas in those two arrays it stays almost constant for a particular Δ value and varying temperature: compare e.g. Fig. 4.7(f) with Δ = 40 V. Fitting Eq. 4.3, L_φ stays between 80 nm and 100 nm, indicating a saturating behavior of the phase coherence length at low temperature.

For an array of N ribbons the total conductance is given by $G_N = N \cdot G_1$, with G_1 the conductance of a single ribbon. This can be seen in Fig. 4.8(a): The absolute conductance of the array is $\sim N$ times larger than for an individual GNR. For further analysis, the variance of the conductance is calculated as var(G_N)= $N \cdot$ var(G_1) and the average fluctuation amplitude as $\Delta G_N = \sqrt{N} \cdot \Delta G_1$. In panel (b) the magneto-conductance with subtracted background is plotted. G_N is plotted in *red*, G_1 in *black*

[4]Or 12 nm, using the 2D formula Eq. 4.1

[5]Also for this sample the mobility was low, cf. table 9.1.

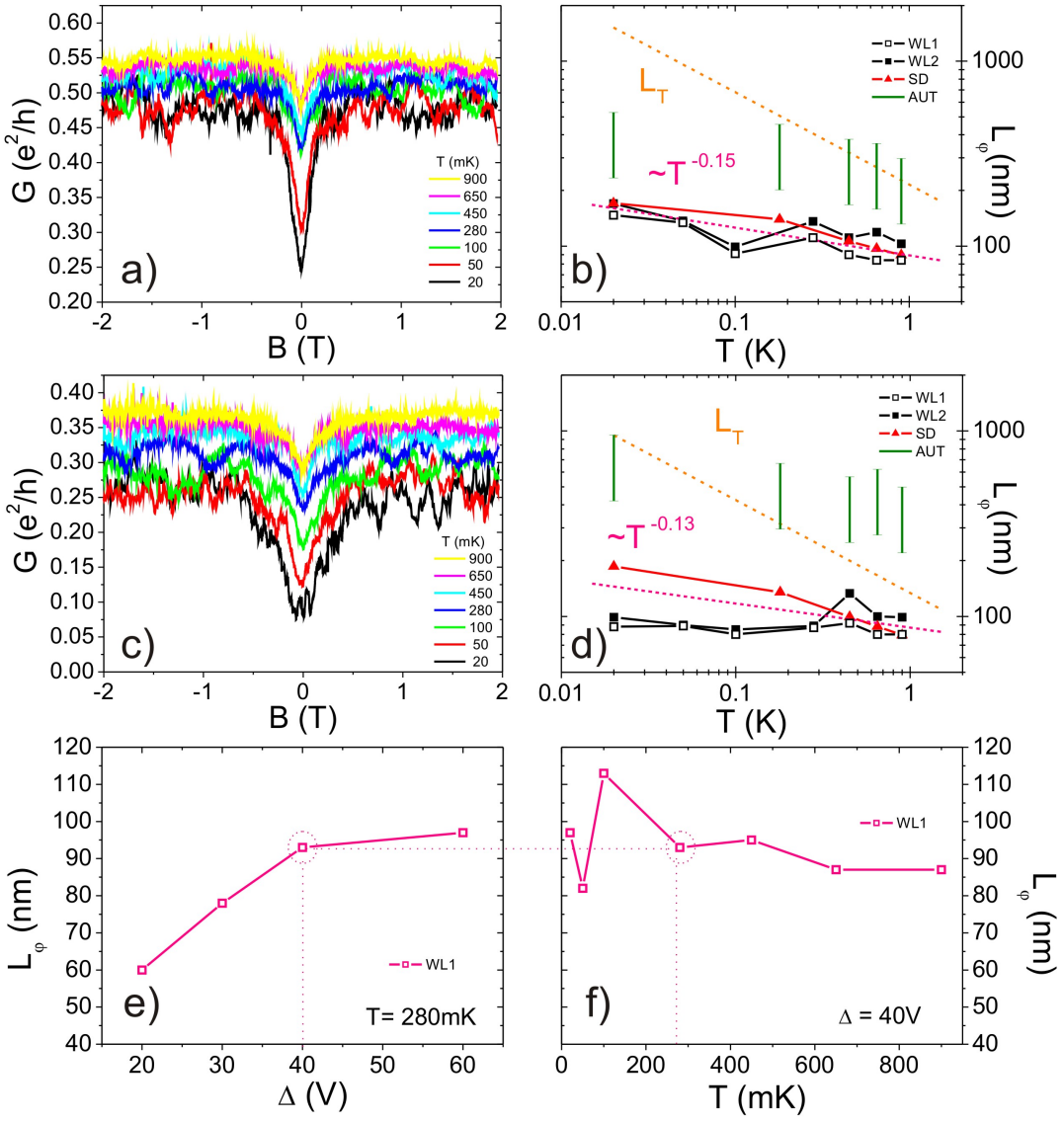

Figure 4.7: Two different arrays of GNRs, sample A3 and A4. (a) Magnetoconductance per ribbon of the array A3 (23 ribbons) at temperatures ranging from 20 mK to 900 mK at V_{bg} = -20 V. In (b) the corresponding phase coherence length L_φ was determined by fitting weak localization (WL), the amplitude of the UCFs (SD) and the autocorrelation function (AUT). The pink, dashed lines are fits of the temperature dependence of L_φ. The orange, dashed line corresponds to the thermal length L_T. Analogous panel (c) and (d) for the second array A4 (32 ribbons). (e) Phase coherence length depending on Δ at T = 280 mK for array A3. (f) Phase coherence length depending on T at Δ = 40 V for array A3.

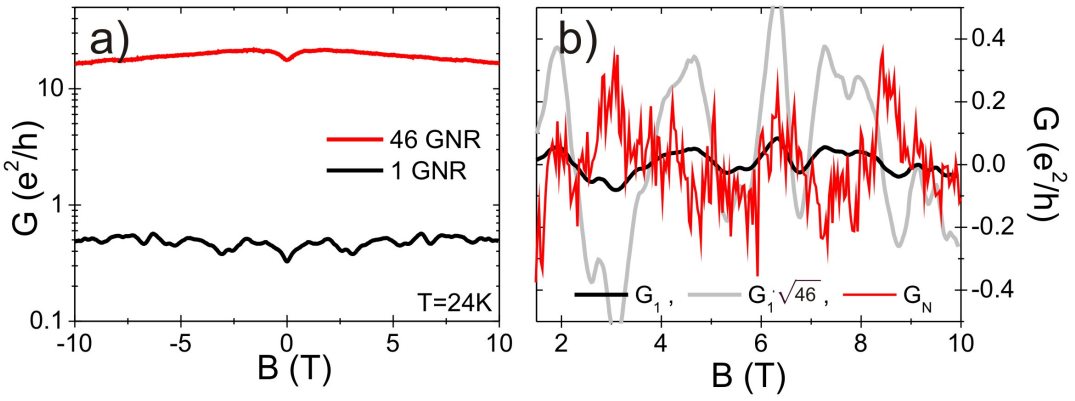

Figure 4.8: (a) Magneto-conductance of an individual graphene nanoribbon (*black*, sample R1, W= 40 nm) and of an array with 46 GNRs (*red*, sample A1, W= 40 nm) at 24 K. The absolute value G_N of the array is $\sim N$ times larger than G_1 of an individual ribbon. (b) Here, the magneto-conductance with subtracted background is plotted. G_N of the array is plotted in *red* and G_1 of the individual ribbon in *black*. Furthermore G_1 was multiplied by a factor of $\sqrt{N} = \sqrt{46}$, *gray* trace. Compared to the conductance of the array G_N, the amplitude of the UCFs *now* is similar. This proves that ensemble averaging increases the conductance amplitude by a factor $\sim \sqrt{N}$.

and $G_1 \cdot \sqrt{N}$ in *gray*. Compared to the conductance of the array G_N, the amplitude of the UCFs of $(G_1 \cdot \sqrt{N})$ is similar. This proves that ensemble averaging increases the conductance amplitude by a factor $\sim \sqrt{N}$. Thus, for the determination of L_φ by analyzing ΔG_{rms} of the array, one has to be aware of a factor of $\sqrt{N}$.
In Fig. 4.7(b) [4.7(d)] the temperature dependence of L_φ, determined by different methods, is shown. Comparing the results obtained by fitting the weak localization feature with the findings from other methods, one recognizes that the values obtained for L_φ are in agreement (WL1, WL2 and SD). Furthermore, for the arrays A3 and A4 the T-dependence of the phase coherence length is similar: $\sim T^{-0.15}$ for array A3 and $\sim T^{-0.13}$ for array A4.
Compared to individual ribbons the behavior of the arrays is the same: The temperature dependence of L_φ is about $\sim T^{-0.30}$ at Kelvin temperatures (e.g. sample A1) and gets weaker at lower temperatures $\sim T^{-0.15}$ (e.g. sample A3 and A4), suggesting a saturating behavior at low temperature.

4.3.3 Crossover from 1D to 2D

For **sample A5** (W_{GNR}= 70 nm) the resistance as a function of back-gate voltage V_{bg} was measured at zero magnetic field and B = 16 T, respectively [Fig. 4.9(a)]. The zero-field trace shows a sharp peak at V_{bg} = +15 V (*black* line), indicating the charge neutrality point. The mobility can be calculated to 450 cm^2/Vs. The gate-dependence at B = 16 T (*red* line) exhibits plateaux indicating that the sample is in the quantum Hall regime. In order to further analyze the Hall plateaux, the resistance as a function of magnetic field was measured at different gate voltages, Fig. 4.9(b). At low magnetic field WL is observed, additionally at higher field values

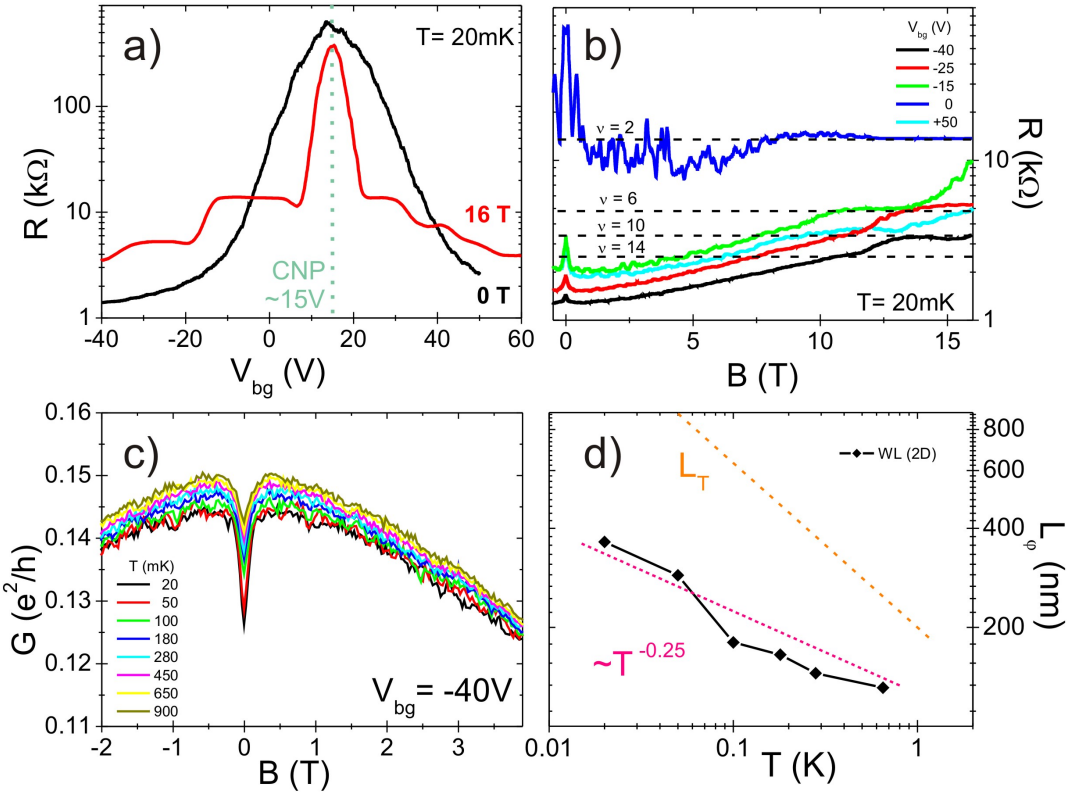

Figure 4.9: Array of 69 GNRs: sample A5. (a) Resistance of the GNR array as a function of back-gate voltage V_{bg} at zero magnetic field (*black*) and B= 16 T (*red*), respectively (at T= 20 mK). The graph shows the charge neutrality point at V_{CNP}= 15 V. For B = 16 T plateaux are visible. (b) Resistance of the array as a function of magnetic field at T = 20 mK and different gate voltages. Hall plateaux for ν = 2, 6, 10 and 14 are visible. (c) Magnetoconductance per ribbon of the array at temperatures ranging from 20 mK to 900 mK at V_{bg} = -40 V. In (d) the corresponding phase coherence length L_φ was determined by fitting weak localization with the 2D-formula [WL (2D)]. The pink, dashed line is a fit of the temperature dependence of L_φ. The orange, dashed line corresponds to the thermal length L_T.

Hall plateaux for ν = 2, 6, 10 and 14 are visible, indicating that the sample is made of single layer graphene.

Focussing on the low field data, we analyzed the weak localization feature in order to determine the phase coherence length. Fig. 4.9(c) shows the magneto-conductance per ribbon at temperatures ranging from 20 mK to 900 mK. Trying to fit the WL feature to Eq. 4.3 or Eq. 4.4, one fails: Since the phase coherence length controls the narrowness as well as the amplitude of the WL feature, the fitting of the width of the dip requires a phase coherence length which results in much too high amplitudes for the WL feature. In contrast, fitting the data to Eq. 4.1, which is the formula for two-dimensional (bulk) graphene, leads to realistic values for L_φ [Fig. 4.9(d)].

The behavior of this sample was very different to the samples measured before. In order to better comprehend the observed behavior we tried to fit the weak localization data of the previous samples to Eq. 4.1 but we failed. The amplitude of the feature never matched. This suggests that sample A5 is different compared to the previous

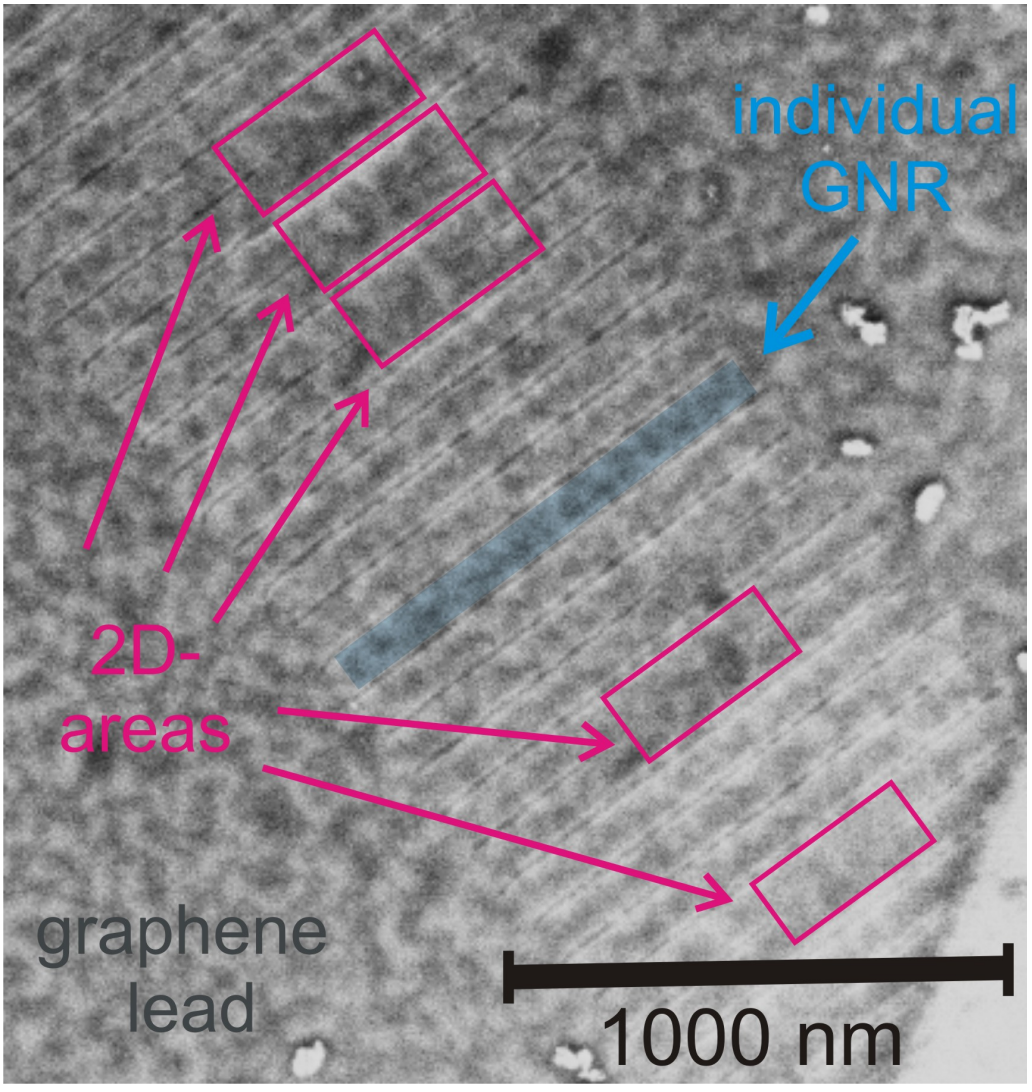

Figure 4.10: Scanning electron microscope image of a part of the GNR array of sample A5. Some etched lines, which define the ribbons of the array, were not successfully etched, so that areas of two-dimensional graphene develop. They are highlighted by the pink frames.

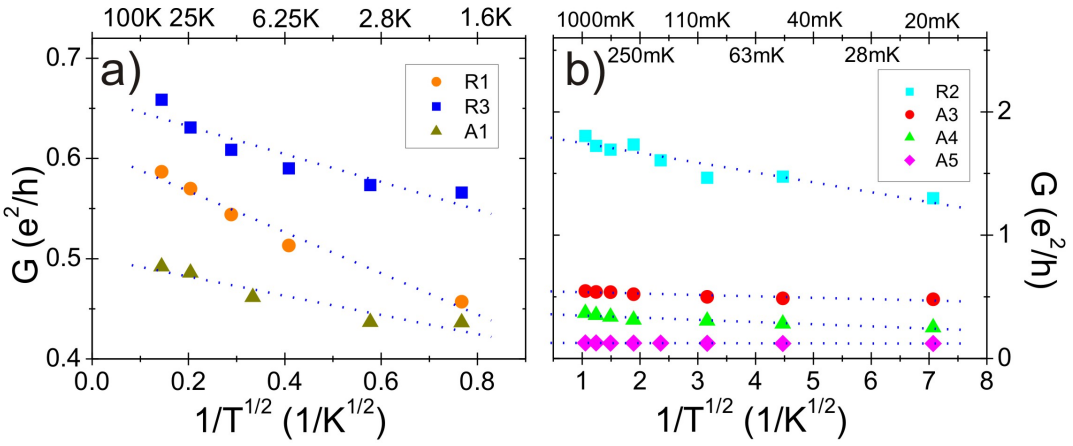

Figure 4.11: Conductance as a function of temperature ($1/\sqrt{T}$) for different samples. The straight dotted blue lines are a guide for the eyes, depicting the expected linear dependence of δG on $1/\sqrt{T}$ in 1D, namely following Ref. [44]: $\delta G_{ee} = -\frac{e^2}{\sqrt{2}\pi\hbar L} g_{1D} \frac{L_T}{W}$ for $W \ll L_T \ll L$ and g_{1D} the effective interaction parameter.

devices. Seeing quantum Hall plateaux, as well as fitting the data with the 2D-WL formula (Eq. 4.1) suggests that sample A5 shows two-dimensional properties. Having a closer look at a scanning electron microscope image of the GNR array, we recognized that some etched lines, which define the ribbons of the array, were not successfully etched, so that those GNR definition-lines are broken, cf. figure 4.10. Altogether five of those regions could be detected. The observation of those 2D-areas (with a width of $\approx$ 180 nm) suggests that already a few, small 2D-areas in the array strongly influence the electron transport properties of the device. Also the observation of quantum Hall states, which were never observed in individual ribbons nor in *true* (that means 2d-area-free) arrays of GNRs at such low magnetic fields, confirm this statement. Only at much higher magnetic fields ($B > 20$ T) Shubnikov-de Haas oscillations in GNRs were observed at Dresden High Magnetic Field Laboratory, cf. Chap. 5.

4.4 Electron Electron Interaction

In addition to the weak localization conductivity correction, the Coulomb interaction of the conduction electrons also leads to a quantum correction. A perpendicular magnetic field can be used to distinguish the two quantum corrections, which have a different field dependence. Therefore, to eliminate an influence of the weak localization, the conductance correction due to electron-electron interaction (EEI) was measured at an external perpendicular magnetic field of 4 T for all samples, except for the two arrays A3 and A4 which were analyzed at about 2 T (for those arrays the WL feature appeared at $|B| < 0.5$ T, therefore a field of 2 T is still appropriate for analyzing the EEI). The electron-electron interaction gives a conductance correction in 1D of $\delta G \propto -1/\sqrt{T}$. In figures 4.3 - 4.7 and 4.9 one clearly observes a decrease of

the absolute conductance with decreasing temperature. Fitting the EEI conductance correction, δG shows the expected linear dependence on $1/\sqrt{T}$, compare Fig. 4.11. This proves that the saturation of L_φ at lowest temperature is not due to unintentional heating of the electrons by a too large bias current or unwanted r.f. coupling.

4.5 Summary

In conclusion, we have performed magneto-transport measurements in graphene nanoribbons as well as in arrays of GNRs. The observation and analysis of weak localization and universal conductance fluctuations allow us to determine the phase coherent properties of those graphene nanostructures.

Fitting weak localization with the standard fitting formula for narrow wires (Eq. 4.3) was appropriate only at low temperature, but reaches its limit of applicability at Kelvin temperature. Therefore we expanded the standard formula to Eq. 4.4. At high temperature, the corresponding fits describe the measured data much better. At mK-temperature universal conductance fluctuations mask the WL feature. Different averaging methods (gate- and ensemble-averaging) allow us to still analyze the sample properties. Furthermore the amplitude and the autocorrelation function of the universal conductance fluctuations themselves were analyzed. The determined phase coherence lengths are comparable to the values of L_φ obtained by fitting the weak localization, whereas the values of L_φ determined by the autocorrelation function are always slightly higher than those obtained from other methods.
In contrast to Ref. [53], analyzing the conductance fluctuations obtained by sweeping the magnetic field or back-gate voltage we do not observe a breakdown of the Ergodic hypothesis. Rather, as expected, we find similar fluctuation amplitudes of about 0.4 e^2/h (cf. Fig. 9.11) and thus the values of L_φ deduced from $\Delta G_{rms}(V_{bg})$ and $\Delta G_{rms}(B)$ match extremely well.
The temperature dependence of L_φ is about $\sim T^{-0.30}$ at Kelvin temperatures and gets weaker at lower temperatures, suggesting a saturating behavior at a few-hundred nanometers for mK-temperature. Thus L_φ clearly exceeds the ribbon width for most of our samples, suggesting that the etching process (at the GNR fabrication) does not destroy the phase coherent properties of the sample.

However, the values of L_φ in graphene nanoribbons (and graphene antidot lattices [54]) seem to be smaller than in bulk graphene. Since localized spins at the ribbon edges may lead to a de-phasing by spin flip scattering and thus lower the phase coherence length, an experiment to be done would be to first saturate the spins in a parallel magnetic field (in order to avoid spin flip scattering) and afterwards to determine L_φ. The values of the phase coherence length will give information about the presence of spin flip processes and might explain the lower values of L_φ in graphene nanoribbons compared to bulk graphene.

5 Magneto-Transport Measurements on Graphene Nanoribbons at High Magnetic Fields

For the application of graphene in nanoelectronics one has to understand the behavior of graphene nanostructures, in particular graphene nanoribbons. They were theoretically predicted to show either metallic or insulating behavior around the charge neutrality point, depending on their crystallographic orientation. In experiment, however, GNRs always exhibit an insulating state close to the charge neutrality point [35], which is dominated by disorder rather than a confinement-induced gap in the spectrum [33, 55]. A clear proof of conductance quantization only appeared very recently in ultra-clean suspended nanoribbons [56]. Furthermore, in clean zigzag edges, a magnetic state has been predicted [57, 58], but so far it has remained elusive in transport experiments. At present, therefore, the behavior of GNRs is mainly governed by extrinsic defects rather than their intrinsic properties, and information on the nature of those defects is highly desired.

In previous experiments, large disorder was attributed to cause strong localization effects which influence the magnetoconductance [36]. Poumirol *et al.* report a large positive magnetoconductance and explain this by simulations which take into account different types of disorder. They affirm the qualitative behaviour, but the computed conductance remains larger than the experimental ones. Also, an unambiguous separation of bulk and edge disorder was not possible [59].

In this chapter we show magneto-transport measurements at fields up to 60 T done at Dresden High Magnetic Field Laboratory and corresponding numerical simulations, done by Jürgen Wurm from the University of Regensburg, which explain the observed features and give new understandings about disorder phenomena, which influence the electron transport in our samples.

[0]The contents of this chapter will be published in *Physical Review B*, publication is already accepted. S. Minke, S. H. Jhang, J. Wurm, Y. Skourski, J. Wosnitza, C. Strunk, D. Weiss, K. Richter, and J. Eroms, *Magnetotransport through graphene nanoribbons at high magnetic fields.*

5.1 Magneto-Transport Measurements and Numerical Simulations

The DC magneto-transport measurements with 10 mV DC bias were done in pulsed, perpendicular magnetic fields up to 60 T at temperatures between 1.8 and 125 K. The magnetic-field pulse resulted from the discharge of a large capacitor bank with a capacitance of 30 mF and a voltage up to 20 kV and lasted typically between 100 and 300 ms. During the pulse the current through the GNR was converted to a voltage signal by a current-to-voltage amplifier and recorded by a high-speed oscilloscope and data recorder. In total two single layer GNRs have been measured which show similar behavior. In this section, we focus on data obtained for **sample D1**,in Sect. 5.3 we shortly present the data of the second single layer GNR (D2) and additionally of a bilayer GNR device (D3), for sample images see Chap. 9. Fig. 5.1(a) shows the two-terminal resistance of the GNR as a function of the applied back-gate-voltage V_{bg} at $T = 25$ K. The sharp peak at $V_{bg} = V_{CNP} = -4.4$ V indicates the charge neutrality point (CNP). The hole mobility μ of the ribbon is about 590 cm^2/Vs at V_{bg}= -15 V[1]. Figure 5.1(b) shows a magnetoresistance curve taken at high carrier density. A quantum Hall plateau at $\nu = 6$ and Shubnikov-de Haas oscillations for $\nu = 10$ and 14 are observed. The corresponding filling factors ν could be assigned to the features by $R = B/(ne) = 25813\ \Omega/\nu$, with the carrier density n and the elementary charge e.

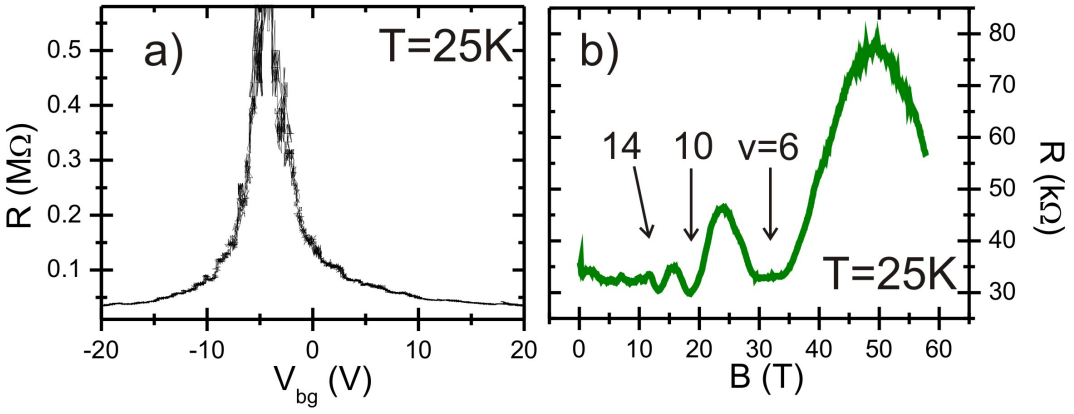

Figure 5.1: (a) Two-terminal resistance as a function of V_{bg} at T= 25 K and zero magnetic field. (b) Magnetoresistance trace at V_{bg} = -20 V, showing the quantum Hall features at $\nu = 6$, 10 and 14.

Since the gate coupling C_g and consequently n strongly depends on the geometrical properties of the ribbons, it was calculated by Comsol, cf. Chap. 3.2. For a 70 nm wide ribbon one has to account a factor of 5.02, which results in $C_g = 576$ aF/μm^2. For this sample the plotting of the fan diagram of the minima of the Shubnikov-de Haas (SdH)

[1]This value does not change significantly if a contact resistance of up to 4 kΩ is taken into account. Our palladium contacts usually have a contact resistance of 1 kΩ or less.

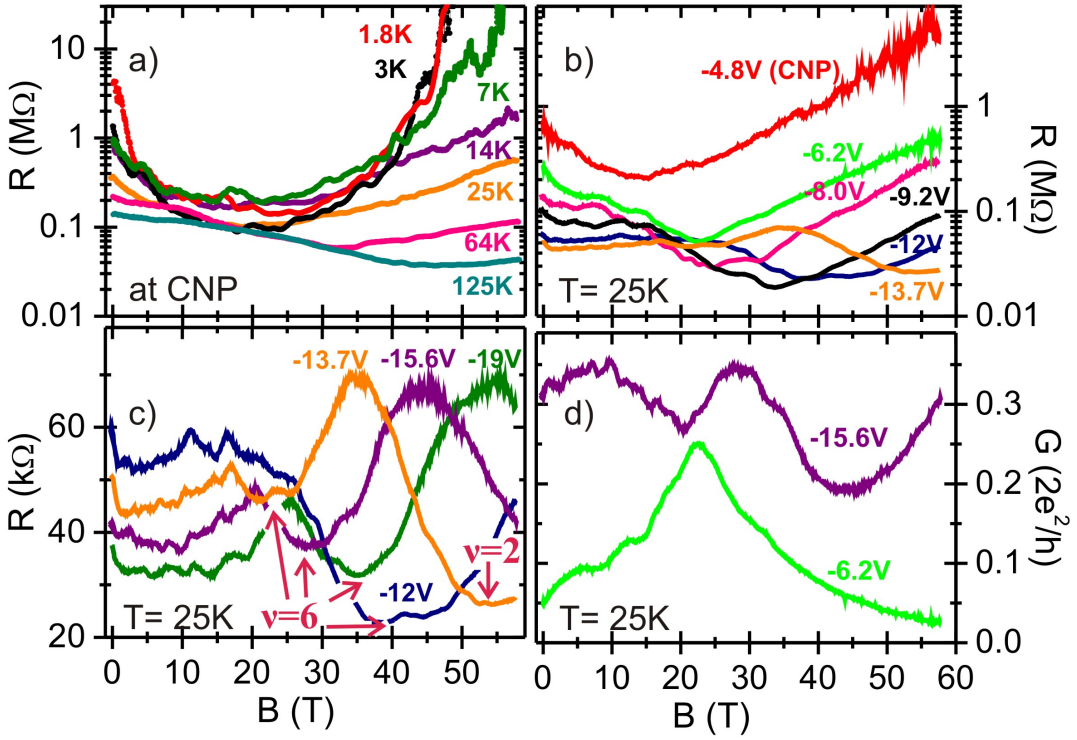

Figure 5.2: (a) Magnetoresistance of the GNR for various temperatures at the charge neutrality point. (b) Magnetoresistance for different gate voltages close to the CNP and (c) further away from the CNP at T= 25 K. The arrows and the numbers indicate the corresponding filling factors ν of the quantum Hall state, ν= 2 and 6. (d) Conductance as a function of magnetic field for V_{bg}= -15.6 V and -6.2 V.

oscillations gives a coupling C_g of 560 aF/μm^2, which matches the calculated value well. Therefore, the carrier density is estimated as $n \approx 3.5 \times 10^{15}$ m^{-2} $\times (V_{bg} - V_{CNP})$ and the Fermi-energy scales as $E_F \approx 69$ meV $\times \sqrt{|V_{bg} - V_{CNP}|}$, where V_{bg} and V_{CNP} are given in Volts.

Next we will focus on the transport properties at gate voltages close to the CNP. For all temperatures we tuned the backgate voltage such that the samples remained as close as possible to the CNP. In Fig. 5.2(a), the magnetoresistance is plotted for various temperatures ranging from 1.8 to 125 K. For all temperatures a resistance decrease is observed for fields up to about 20 T, so that the ribbon crosses over from a highly resistive state to a metallic regime. Subsequently, it is followed by a prominent resistance increase. The divergent form of the latter increase suggests that the nanoribbon approaches a field-induced insulating state.

In order to better comprehend the observed behavior, we studied the magnetoresistance for different gate voltages at T= 25 K, Fig. 5.2(b) and (c). Clearly different results are observed whether the measurement was done close or further away from the charge neutrality point. As one can see in panel (b), the observed divergence of the resistance at very high fields only appears for gate-voltages close to the CNP ($|V_{bg} - V_{CNP}| < 9$ V). Whereas at higher densities [panel (c)] we observe

weak localization at fields up to 1 T[2] , a fairly constant resistance up to about 20 T and then pronounced resistance oscillations. These oscillations can be identified as Shubnikov-de Haas oscillations, which can be assigned to Hall-plateau values of single layer graphene ($\nu = 2$ and 6).
Representative for the low- and high-carrier-density regime, Fig. 5.2(d) shows the conductance G as a function of magnetic field for two different carrier densities. The high-carrier-density conductance (V_{bg}= -15.6 V, purple) shows the oscillating behavior as described before, the low-density trace (V_{bg}= -6.2 V, green) exhibits first a conductance increase followed by a conductance decrease.

The experimental data give us important insight into the nature of the defects relevant in our GNRs. To this end, Jürgen Wurm from the University of Regensburg performed numerical magnetotransport simulations of (armchair) graphene nanoribbons with realistic sizes ($L = 320\,\mathrm{nm}$, $W \sim 25\,\mathrm{nm}$). For more details see [60]. Since Ohmic scaling is not applicable at those length scales [61] we do not expect a full quantitative match between theory and experiment. However, the qualitative behavior will be well reproduced by the simulations since the system size is of the same order as the experimental samples. The well known graphene tight-binding Hamiltonian in nearest neighbor (n.n.) approximation was used.

To appropriately describe the experimental situation, different types of disorder were considered. Since the fabrication process certainly leads to disordered edges, we took this into account also in the numerical simulations. To this end, 'chunks' of about 4 nm were cut out of the graphene lattice at random positions close to the edge, which simulates the large-scale edge roughness that occurs due to e-beam resist roughness and the random nature of reactive ion etching. Additionally, edge roughness on a smaller scale of a few lattice constants was accounted for by using a model introduced in Ref. [31]: About 10 percent of the edge atoms are randomly removed and subsequently dangling bonds are additionally removed. This procedure was repeated 5 times to yield an edge roughness of a few lattice constants. In the following, in the case of edge disorder, both mechanisms will always be included. The inset in Fig. 5.3(a) shows a section of the resulting edge.
In addition to the edge disorder, we studied two types of bulk potential disorder. On the one hand, we modeled so-called electron-hole puddles, *i. e.*, long range potential fluctuations due to charged impurities trapped beneath the graphene ribbon in the silicon-oxide substrate. Second, we also consider shorter-ranged impurity potentials, that can arise due to adsorbates, defects or charged impurities. In both cases, Gaussian on-site potentials were added to the tight-binding Hamiltonian. For the puddles, Gaussians with a decay length of $\sim 8.5\,\mathrm{nm}$ and a total height of $\sim 80\,\mathrm{meV}$ were used, which is comparable to the experimentally determined values [63]. The impurities were modeled by Gaussians with a decay length of $\sim 0.44\,\mathrm{nm}$ [64].

In Fig. 5.3, we present the numerical results for magnetotransport through disordered nanoribbons at relatively high ($E_F \approx 226\,\mathrm{meV}$) and lower ($E_F \approx 92\,\mathrm{meV}$) carrier densities, corresponding to the Fermi energies of the experimental data in Fig. 5.2(d). First, we consider ribbons with edge disorder only [Fig. 5.3(a)]. We find that while the zero-field conductance for low densities is comparable to the

[2]Fitting the WL feature, using Eq. 4.3, yields a phase coherence length between 35 nm and 55 nm for V_{bg} between -12 V and -19 V [Fig. 5.2(c)].

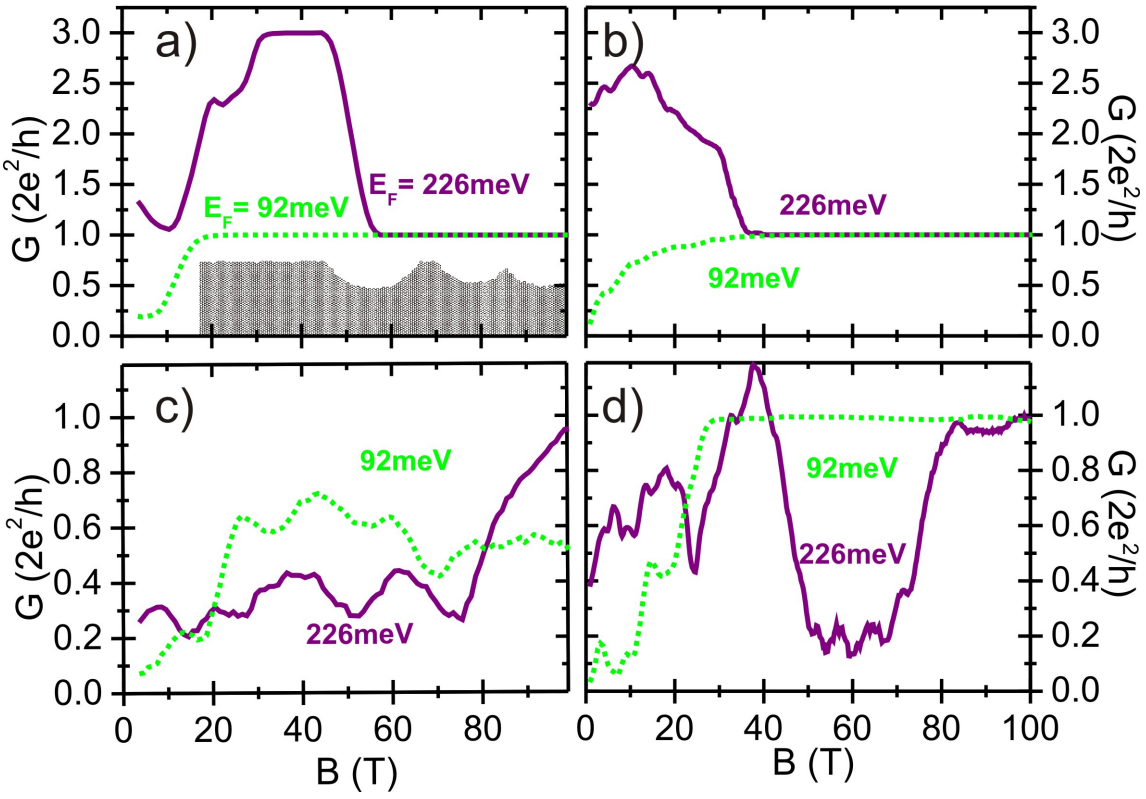

Figure 5.3: Magnetoconductance of armchair GNRs ($L = 320\,\text{nm}$, $W \sim 25\,\text{nm}$) calculated numerically, using tight-binding simulations [62] and different disorder models (Courtesy of Jürgen Wurm). (a) Edge disorder (see inset and text). (b) Long-range Gaussian disorder. (c) Short-range impurities. (d) Edge disorder and short-range Gaussian disorder.

experiment, this is not the case for the high-density result. Upon increasing the field, the wavefunctions become more localized close to the edges. Without bulk disorder, backscattering is strongly suppressed, so that calculations yield nearly perfect quantum Hall plateaus for all densities already at moderate fields, in contrast to the experimental findings. This means that edge disorder alone cannot explain the experiment. Considering only long-range Gaussian disorder [panel (b)], we find that the puddles are rather effective scatterers at low density, while they affect G only little at high densities. This is quite understandable, because the small energies are of the same size than the potential fluctuations and the charge carriers are influenced quite much. In contrast for energies several times higher than the fluctuations the carriers are not influenced by backscattering. Simulations where only the short-range impurities are taken into account [panel (c)], show that indeed for strong enough scattering potentials, the zero-field conductance can be very close to the experimental data. However, such strong bulk disorder leads to backscattering even for very high magnetic field, so that at high density no SdH oscillations can be observed. This implies that indeed a combination of bulk *and* edge disorder is necessary to describe the high-field experiments. In panel (d), we show the results for ribbons with disordered edges and short-range bulk disorder. In this case, the experimental findings for low and moderate field are reproduced semi-quantitatively. For low density we find a strong increase of G due to the formation of edge channels, while

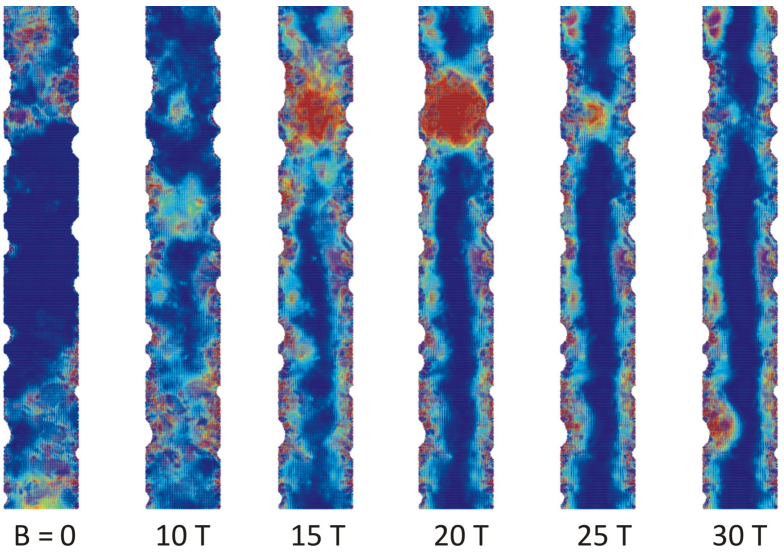

Figure 5.4:
Local particle density in GNRs with edge and bulk disorder for low energies and different magnetic fields (Courtesy of Jürgen Wurm). Red corresponds to high and blue to low densities. The particles enter the ribbon from the bottom, so that at high fields the quantum Hall edge channels form at the left edge [60].

clear SdH oscillations are obtained at higher densities. In Fig. 5.4 the particle density at different magnetic fields is shown, confirming this picture [60]. Also the zero-field conductance [Fig. 5.3(d)] fits well with the experiment. In contrast, in simulations that additionally include the long-range puddles, the difference in the zero-field conductance for high and low densities is much too high, thus we conclude that puddles are not the dominant scatterers in our samples. We note that beyond this disorder model interaction effects may further influence the measured conductance.

We now turn our attention to the sample properties at high magnetic fields near the CNP. As shown in Fig. 5.2(a), the resistance at low temperatures initially decreases with B and then diverges steeply by several orders of magnitude for $B > 20$ T. While the initial negative magnetoresistance at low densities is explained in the previous section by the formation of edge channels related to the zero-energy Landau level (LL) in graphene, a crossover to a divergent resistance for $B > 20$ T requires another transport mechanism. The zero-energy state in bulk graphene has been investigated by several research groups, and a strong increase in R at the CNP and intense magnetic fields has been observed, resulting in a B dependent LL splitting [65, 66] and eventually a strongly insulating state [67, 68], the exact nature of which is still under debate [69]. Adopting a simple model involving the opening of a field-dependent spin gap [65], we can fit the temperature dependence of R for $T \geq 14$ K in an Arrhenius plot for distinct magnetic-field values (inset of Fig. 5.5). In Fig. 5.5, energy gaps Δ are extracted from a linear fit to the Arrhenius plot. The gap Δ shows a linear dependence on B (Fig. 5.5, *red, dashed* line), consistent with spin splitting of the zero-energy LL, with the gyromagnetic factor g=1.73. However, another origin of the gap can also be considered. Following for example Ref. [70], we can fit $\Delta \propto C \cdot (B - B_c)^{0.5}$ with $B_c \approx 29$ T and $C \approx 11$, cf. *blue solid* line Fig. 5.5, suggesting a chiral symmetry breaking transition. Comparing those different models we conclude that both mechanism are compatible with our data, but the exact nature of the gap can not be determined experimentally. For lower temperatures ($T \leq 7$ K), however, the resistance diverges strongly with B, and a simple activated behavior can no longer explain our data. This divergent behavior of R in our GNRs resembles

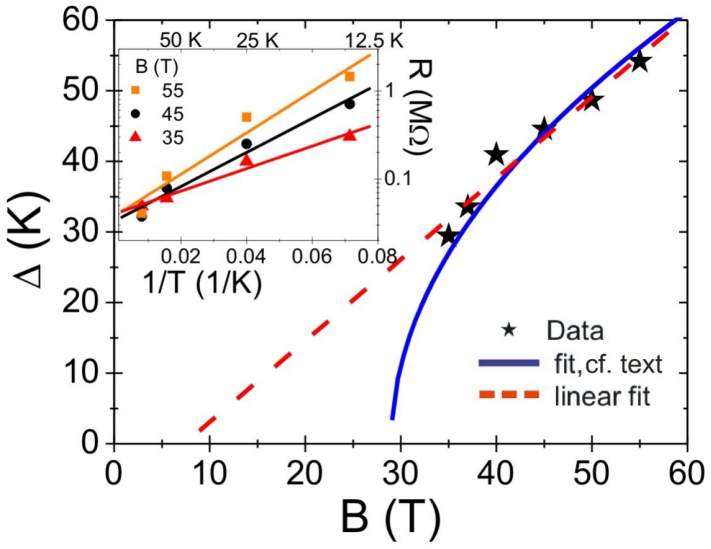

Figure 5.5:
Energy gaps Δ extracted from the slope of the Arrhenius plot for $T \geq 14$ K (inset). Different fits to the data points. The (red) dotted line fits the Zeeman splitting $\Delta = (g\mu_B B)/k_B - 8.9$ K with the Bohr magneton μ_B, the Boltzmann constant k_B and a gyromagnetic factor of $g = 1.73$. The (blue) continuous line is a fit following Ref. [70], cf. text.

a field-induced transition to a strongly insulating state reported in bulk graphene at low T [67, 68]. In cleaner samples the transition to the insulating state occurred at significantly lower fields.

Given the typical sample geometry [Fig. 9.5(a)], we note that (bulk) graphene leads are attached to the GNR. Since our GNRs, after patterning, have lower mobility than the bulk graphene leads the field required for the B-induced insulating state is expected to be also higher. Therefore, the observed divergent R at very high B and low densities is tentatively attributed to the leads: when we apply high B-fields the leads become insulating and mask the electron transport in the GNR.

5.2 Additional analysis

In order to get further information about our samples we analyzed the temperature dependence of the resistance at zero magnetic field and at the charge neutrality point. The corresponding resistance values $R(0)$ were plotted as a function of T^{-x}, where the value of x determines the mechanism present in our system [71, 72].
For thermally activated behavior $x = 1$ and $R(T) \propto \exp(\Delta\epsilon/2k_BT)$. As clearly shown in Fig. 5.6 (*black*), our data is not described by the thermal activation law over the whole temperature range. The slope of $\log R$ vs. $1/T$ decreases with decreasing temperature T, suggesting the presence of hopping. When we re-analyze the data in terms of Efros-Shklovskii variable range hopping, where $R(T) \propto \exp(T_0/T)^{1/2}$, we can not fit the data very well either (*red*). A further analysis model is the two-dimensional Mott variable range hopping (2D-VRH). In this model the dependence of R is given by $R(T) \propto \exp(T_0/T)^{1/3}$. Comparing the fits of the different models, the Mott 2D-VRH model (*green*) might be the most appropriate. Since there are still deviating data points we rather suppose that no clear preference for a particular law can be deduced from the data and thus no statement about the exact mechanism

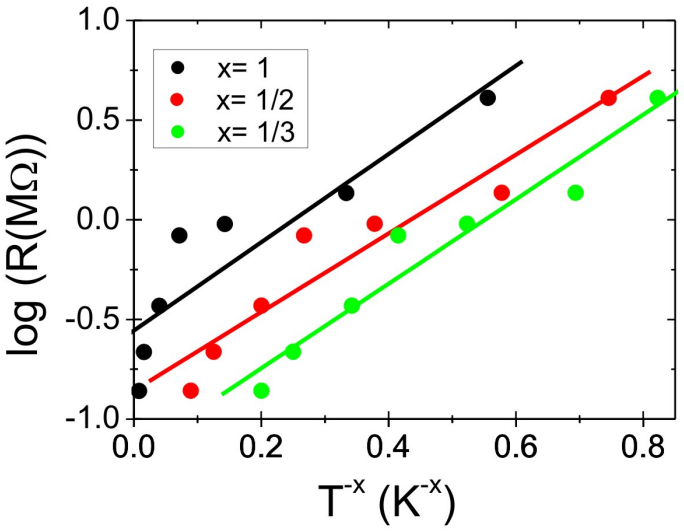

Figure 5.6: Resistance R of the GNR at the charge neutrality point and zero magnetic field plotted as a function of T^{-x}. The solid lines represent fits to the experimental data where x=1 for thermal activated transport, x=1/2 for Efros-Shklovskii variable range hopping and x=1/3 for two-dimensional Mott variable range hopping.

present can be given. Since in our measurements we used a rather high bias voltage, dictated by the need to record a full magneto-transport curve at an acceptable signal to noise ratio within $\sim$ 100 ms, they probably mask the T-dependence, particular at low temperatures.

Another possibility of getting information about the nature of the impurities present in the sample, is the analysis of the transport time τ_{tr} and the elastic scattering time τ_e [73]. Generally $\tau_{tr} \neq \tau_e$, the transport time τ_{tr} governs the current relaxation and the elastic scattering time τ_e is the lifetime of a plane wave state. For a 2D electron gas confined to GaAs/GaAlAs heterojunctions with the scattering potential produced by remote charged Si donors the ratio τ_{tr}/τ_e is found to be larger than 10. For single-layer and bilayer graphene it was found to be about 2. Following Ref. [73] we can analyze our data by fitting the magneto-resistance traces to the following equation (for single-layer graphene). Thus τ_e can be extracted as the only fit parameter.

$$\delta R(B)/R_0 = -4D_T \exp\left(-\frac{\pi}{\omega_c \tau_e}\right) \cos\left(\frac{\pi E_F}{\hbar\omega_c} - \pi\right), \tag{5.1}$$

with $\delta R(B)/R_0$ the normalized resistance, the cyclotron frequency $\omega_c = eB/m^*$, the cyclotron mass $m^* = \hbar k_F/v_F$, the Fermi energy $E_F = \hbar k_F v_F$ and the Fermi wave vector $k_F = \sqrt{\pi n_s}$. The prefactor $D_T = \gamma/\sinh(\gamma)$ with $\gamma = 2\pi^2 k_B T/(\hbar\omega_c)$ describes the thermal damping of the oscillations. From the analysis of the magneto-resistance trace at V_{bg} = -20 V and T = 25 K, we extract $\tau_e = 1.46 \cdot 10^{-14}$ s, cf. Fig. 5.7. Calculating the transport time $\tau_{tr} = \mu m^*/e$, with the mobility μ, we also obtain $1.46 \cdot 10^{-14}$ s. Thus the ratio $\tau_{tr}/\tau_e = 1$ in contrast to the findings of Ref. [73], where it was 2 for single-layer graphene.
This deviation can be explained by the study of graphene nanoribbons instead of single-layer (bulk) graphene. In GNR impurity scattering is *enhanced* due to edge

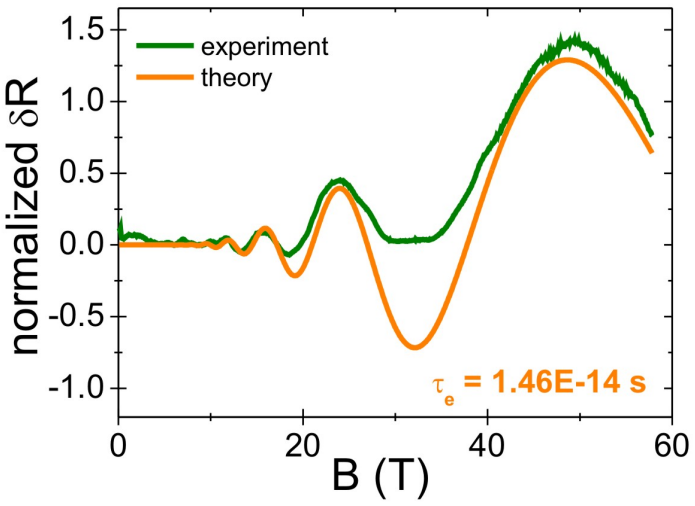

Figure 5.7: Analysis of the magneto-resistance trace at V_{bg} = -20 V and T = 25 K [Fig. 5.1(b)], which shows the quantum Hall features at ν = 6, 10 and 14. The *orange* line is fit according to Eq. 5.1.

scattering and thus the transport time τ_{tr} is *reduced*, leading to $\tau_{tr}/\tau_e = 1$. Also the appearance of the quantum Hall features, at lower field values than expected, can be explained by this. From the zero field mobility and the condition $\mu B \gg 1$ we would expect to observe the quantum Hall features only beyond 20 Tesla, but the quantum Hall feature at $\nu = 14$, at 13 Tesla, is clearly resolved. Although the mobility only is determined by the transport time τ_{tr}, edge scattering does not destroy the quantum Hall state (cf. theoretical findings) and quantum Hall features can be observed at at lower fields than expected from the simple condition $\mu B \gg 1$.

5.3 Other Samples

In addition to the sample shown in the previous section, here, we present another single layer device (**sample D2**), confirming the observed behavior: In Fig. 5.8(a) the magnetoresistance of the nanoribbon is shown for different temperatures at V_{bg} = 46 V, which corresponds to the low-carrier-density regime ($V_{CNP} \geq 70$ V, cf. inset). Although fluctuations are superimposed on the data, we clearly observe first a resistance decrease for fields up to 25 T, followed by a resistance increase. This is in agreement to the observations of the previous device. Equally, the increase shows a divergent form, especially for low temperatures. Performing magneto-resistance measurements at different back-gate values at 4.2 K, we can affirm that the resistance increase only appears for low carrier densities. For higher densities ($V_{bg} \leq 20$ V) we only observe the initial resistance decrease archiving almost constant values at high magnetic fields, cf. Fig. 5.8(b).

However, for the bilayer graphene device (**sample D3**) observations are different. Fig. 5.8(c) shows the two-terminal magneto-resistance for T = 4.2 K and 77 K at zero magnetic field close to the CNP ($V_{CNP} \sim 25$ V). As in single layer GNRs, for fields up to 20 T we observe a resistance decrease. But subsequently we do *not* observe a

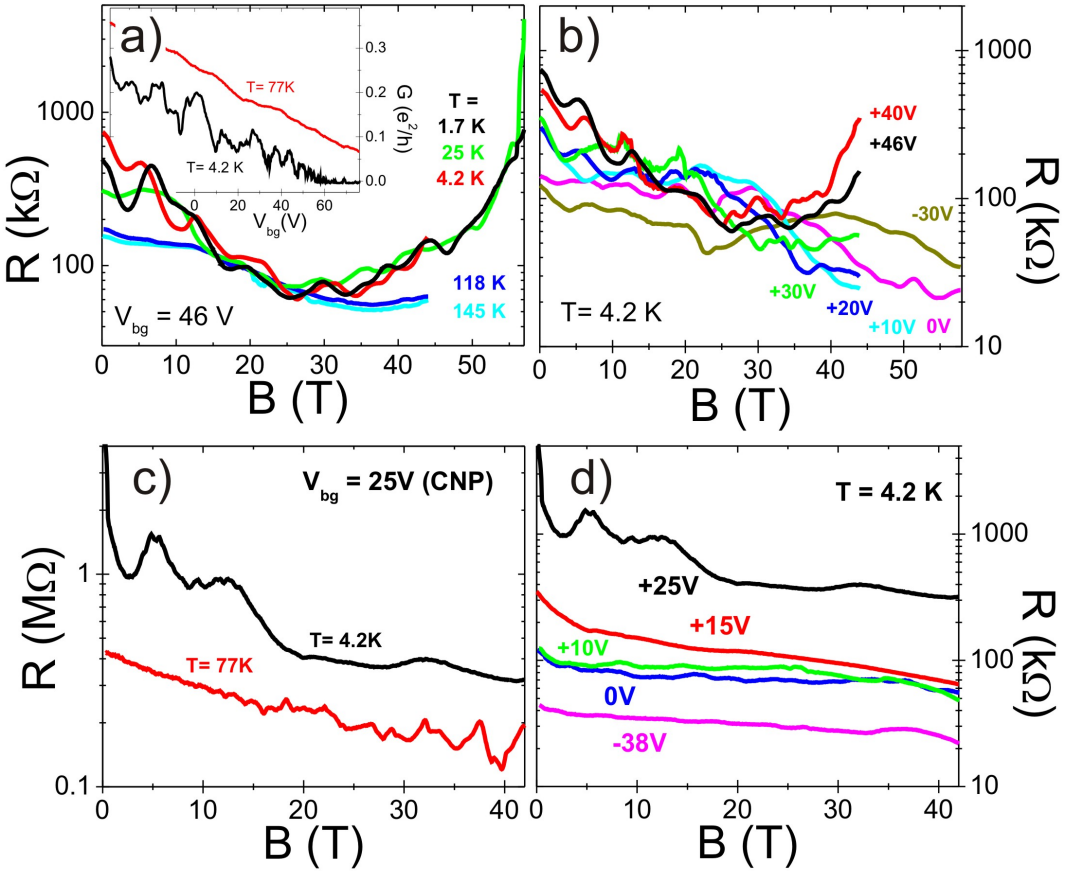

Figure 5.8:
Sample D2 (single-layer GNR): (a) Magneto-resistance of the GNR for various temperatures at $V_{bg} = 46$ V. (inset) Conductance as a function of V_{bg} at $T = 4.2$ K and 77 K and zero magnetic field. (b) Magneto-resistance for different gate voltages at $T = 4.2$ K.
Sample D3: (bilayer GNR): (c) Magneto-resistance of the bilayer GNR for $T = 4.2$ K and 77 K close to the charge neutrality point. (d) Magneto-resistance at different gate voltages and a temperature of 4.2 K.

resistance increase, rather the resistance further slightly decreases up to 43 T, even for the lowest temperature of 4.2 K. Similar magnetic field dependence of the resistance was found for all measured gate voltages, cf. Fig. 5.8(d). The observed behavior is in contrast to the single layer one. Possibly for bilayer devices such a transition to an insulating state does not exist. Or the transition field is at much higher magnetic field values which we can not achieve in our experimental setup. Since the examination of the different behavior in single- and bilayer graphene nanoribbons was not subject of this thesis, it is only addressed briefly here for completeness.

5.4 Summary

In conclusion, we have performed transport experiments in graphene nanoribbons in pulsed high magnetic fields and corresponding transport simulations, based on a tight-binding model. This allows us to separate the contributions of different disorder types to magnetotransport. At least a combination of edge disorder and short-range bulk impurities is needed to reproduce the experimental results semi-quantitatively. The short-range bulk disorder is responsible for the partial suppression of the quantum Hall effect, while the edge disorder, together with the bulk disorder, provides sufficient backscattering to explain the observed high resistance at zero field for all carrier densities. Additionally, we observe a magnetic-field-induced insulating state at very low densities, which presumably originates from the bulk graphene leads.

6 Stacking-Order Dependent Transport Properties of Trilayer Graphene

In few-layer graphene (FLG), the stacking order offers an extra degree of freedom. The electronic structure and the Landau level spectrum differ significantly depending on the stacking order in FLG [4, 6, 20, 21, 74]. For instance, Bernal (ABA)-stacked trilayer exhibits an electric-field tunable band overlap [7, 11], while rhombohedral (ABC)-stacked trilayer is predicted to present a tunable band gap [6, 20, 74, 75], cf. Chap. 2.1. Here, we report stacking-dependent transport properties of double-gated trilayer graphene, combined with Raman spectroscopy. We show that the effects of applied electric and magnetic fields on the ABC-stacked trilayers are strikingly different from those on the ABA-stacked trilayers [12].

6.1 Raman Measurements

Raman spectroscopy can be used to determine the number of graphene layers and stacking order as well as the density of defects and impurities. The three most prominent peaks in the Raman spectrum of graphene and other graphitic materials are the G band, the 2D band and the disorder-induced D band, which can be used to characterize the number of defects in a graphene sample [76].
Raman measurements were done by Monica Craciun at the Centre for Graphene Science (University of Exeter, England). We used an excitation laser with a wavelength of 532 nm and a spot size of 1.5 μm in diameter. The Raman spectra of mechanically exfoliated graphene shows the G band and the 2D (G′) band at respectively 1580 cm^{-1} and 2700 cm^{-1} [Fig. 6.1(a)]. The G band is due to the first-order Raman scattering by the double degenerate E_{2g} phonon mode at the Brillouin zone center, while the 2D band originates from a second-order process, involving two intervalley optical phonons near the boundary of the Brillouin zone [77]. The peak at 520 cm^{-1} (labeled as Si) is due to the first-order Raman scattering by optical phonons of the Si substrate.

[0]The contents of this chapter have been published in *Physical Review B*:
S. H. Jhang, M. F. Craciun, S. Schmidmeier, S. Tokumitsu, S. Russo, M. Yamamoto, Y. Skourski, J. Wosnitza, S. Tarucha, J. Eroms, and C. Strunk, *Stacking-order dependent transport properties of trilayer graphene.* Phys. Rev. B **84**, 161408(R) (2011) [12]

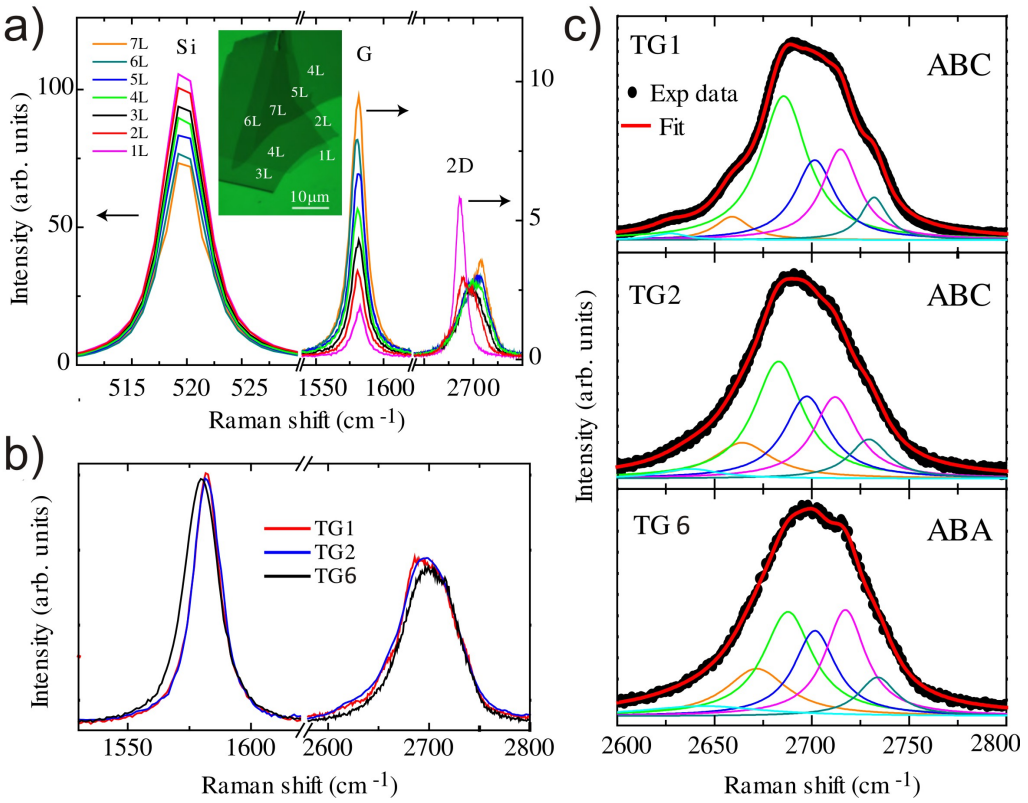

Figure 6.1: (a) Raman spectra for graphene samples with different number of layers. The inset shows the optical microscope picture of the flake containing up to 7 layers used for these measurements. The labels 1L to 7L indicate the number of layers. (b) Raman spectra of trilayer samples TG1, TG2 and TG6. (c) The 2D Raman band of graphene trilayers with *ABC* stacking (TG1 and TG2) and *ABA* stacking (TG6). The red lines are fits by 6 Lorentzian functions and the lines of other colors are the Lorentzian components of the fits.

A reliable approach to count the number of layers (N) of FLG deposited on Si/SiO_2 substrates is based on the ratios of the intensities of the G peak and the Si peak, I_G/I_{Si} [78]. As shown in Fig. 6.1(a), for a flake containing up to 7 layers, the intensities of the G and Si peaks clearly change with N. We find that I_G/I_{Si} increases monotonically and discretely with N due to an increase of the intensity of the G peak and a decrease of the intensity of the Si peak. Our findings are in agreement with recent observations, which attribute this behavior to enhanced absorption and Raman scattering of light by thicker graphene layers [78]. In Figure 6.1(b), we show the Raman spectra of the trilayer **samples TG1** (sample M9_D2), **TG2** (M9_D3) and **TG6** (SR1_D1), for sample images see Chap. 9. These samples have G and 2D peaks of similar intensities and their I_G/I_{Si} is consistent with the typical values found for trilayer graphene.

An accurate determination of N for up to three layers is also possible from the 2D peak since its shape and position evolves with N [see Fig. 6.1(a)]. The 2D band is affected by the band structure of the material since it arises from a double-resonance process involving transitions among various electronic states. As trilayer graphene has three valence and three conduction bands, up to 15 electronic transitions can contribute to the 2D band. [79] However, many of these different processes have very

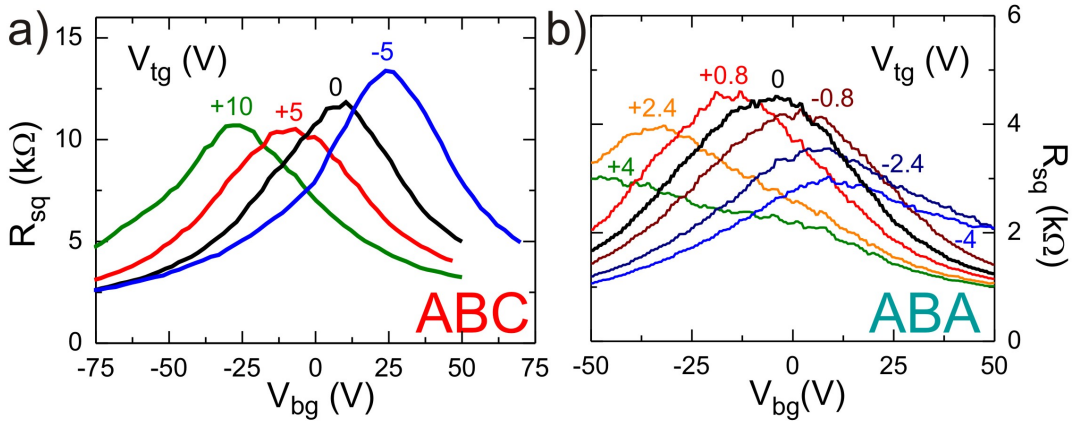

Figure 6.2: Square resistance R_{sq} as a function of back-gate voltage for different fixed values of top-gate voltage at 4.2 K, shown for (a) *ABC* trilayer and (c) *ABA* trilayer with thicknesses of top-gate dielectric of 90 and 15 nm, respectively.

close energy separations and experimentally it is found that the minimum number of Lorentzian functions necessary to correctly fit the 2D mode of trilayer graphene is six [79, 80]. Consistently, Fig. 6.1(c) shows that for all the trilayer samples a good fit can be achieved with 6 Lorentzian functions. The full width at half maximum of all the fitting Lorenztian functions is fixed to be the same as that of the 2D band of monolayer (24 cm^{-1}) and we only vary the peak positions and intensities.

Having determined the number of layers, we now address the stacking order in our trilayer samples. It has been recently demonstrated that an accurate and efficient method to characterize stacking order in FLG is based on the distinctive features of the Raman 2D peak. [80] We find that TG1 and TG2 show a more asymmetric 2D peak than TG6, compare Fig. 6.1(c), consistent with the reported differences between *ABC* and *ABA* stacking [80]. These differences in the 2D band feature are best captured by the Lorentzian components of their fits. In particular, the Lorentzians with the highest intensities - i.e., centered around 2685 cm^{-1} (green) and 2715 cm^{-1} (purple) - have very different intensities in the *ABC* samples (TG1 and TG2), whereas they have almost equal intensities in the *ABA* trilayers (TG3), in agreement with the observations reported in Ref. [80].

6.2 Transport Measurements

We now turn our attention to the transport properties of trilayer graphene in double-gated transistor structures. The DC magneto-transport properties were studied at liquid-Helium temperatures in pulsed perpendicular magnetic fields of up to 50 T. The magnetic-field pulse resulted from the discharge of a large capacitor bank with a capacitance of 30 mF and a voltage up to 20 kV, and lasted typically $\simeq$ 500 ms.

The device geometry allows the independent control of the Fermi energy and the external perpendicular electric field E_{ex} applied to the trilayers. In particular, the E_{ex} is given by $E_{ex} = V_{tg}/d_{tg} - V_{bg}/d_{bg}$ with V_{tg} and V_{bg} the top- and back-gate voltages

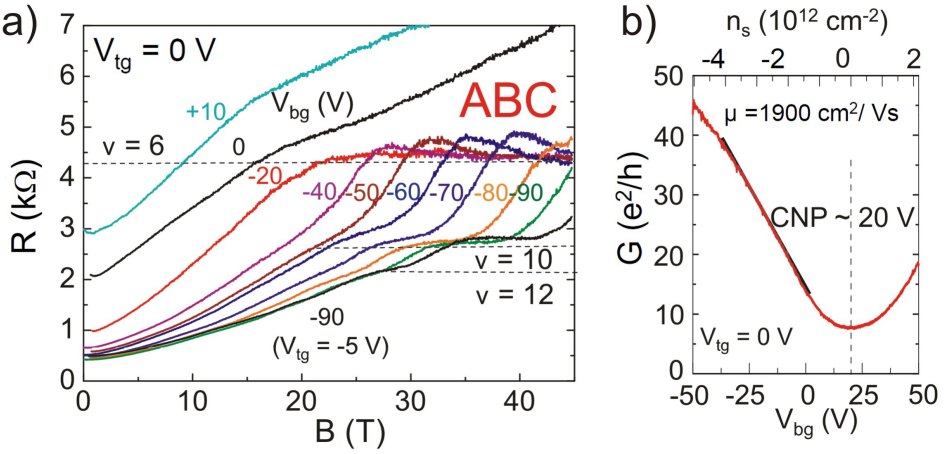

Figure 6.3: (a) Two-terminal magnetoresistance of the *ABC*-stacked trilayer (TG1) at 4.2 K, shown for various back-gate voltages at $V_{\mathrm{tg}} = 0$, except for a trace indicated. QHE plateaus develop at $\nu = 6$, 10, and 12 (dashed lines). The small deviations from the dashed lines reflect the contact resistance of our device. (b) Conductance G of the *ABC* trilayer device (TG1) as a function of V_{bg} (or carrier density n_{s}) at $V_{\mathrm{tg}} = 0$. The mobility, μ, is estimated from the linear V_{bg} dependence of G at large back-gate voltages.

respectively, and d_{tg} and d_{bg} the thicknesses of the top- and back-gate dielectric. Fig. 6.2 show the 2-terminal square resistance (R_{sq}) of trilayers with different stacking orders, measured for fixed values of V_{tg} as a function of V_{bg}. In all cases R_{sq} displays a maximum ($R_{\mathrm{sq}}^{\mathrm{max}}$) corresponding to the charge neutrality in the system. Clearly, the evolution of $R_{\mathrm{sq}}^{\mathrm{max}}$ with E_{ex} is markedly different for the two stacking orders. For *ABC* trilayer $R_{\mathrm{sq}}^{\mathrm{max}}$ increases with increasing E_{ex}, whereas the opposite behavior is observed for *ABA* trilayer, i.e. $R_{\mathrm{sq}}^{\mathrm{max}}$ decreases with increasing E_{ex}. In both cases the position in V_{bg} of $R_{\mathrm{sq}}^{\mathrm{max}}$ shifts linearly with V_{tg}, reflecting the changes in charge density induced by the two gates.

These results can be understood by the effect of the perpendicular electric fields on the band structure of *ABA* and *ABC* graphene trilayers. Theory predicts that the interlayer asymmetry induced by the electric field opens an energy gap in the band structure of *ABC* trilayers [Fig. 2.5(i)] [6, 20, 74, 75], whereas it causes a band overlap in *ABA* trilayers [Fig. 2.5(h)] [7].

6.2.1 *ABC* Trilayer Graphene

Fig. 6.3 up to Fig. 6.6 illustrate the effect of a perpendicular magnetic field on the transport properties of *ABC* and *ABA* trilayer graphene at $T = 4.2$ K.
For the *ABC*-stacked trilayer **sample TG1** ($\mu \approx 1900$ cm^{2}V^{-1}s^{-1}) the 2-terminal magnetoresistance indicates QHE plateaus at $\nu = 6$ and 10 for $B > 20$ T [Fig. 6.3(a)]. The filling factor $\nu = n_{\mathrm{s}}\phi_0 B^{-1}$, where ϕ_0 is the flux quantum, matches well with the carrier density $n_{\mathrm{s}} = \alpha(V_{\mathrm{bg}} - V_{\mathrm{CNP}})$ calculated using $\alpha = 7.2 \times 10^{10}$cm^{-2}V^{-1}. The observed plateaus are expected from the 3-fold degenerate zero-energy LLs of the *ABC* trilayer graphene ($E_n \propto B^{3/2}\sqrt{n(n-1)(n-2)}$) with 4-fold spin and valley degeneracy (cf. Chap. 2.2). We find QHE plateaus only away from the charge neutrality point (CNP) located at $V_{\mathrm{CNP}} \sim 20$ V for $V_{\mathrm{tg}} = 0$ [Fig. 6.3(b)]. An additional

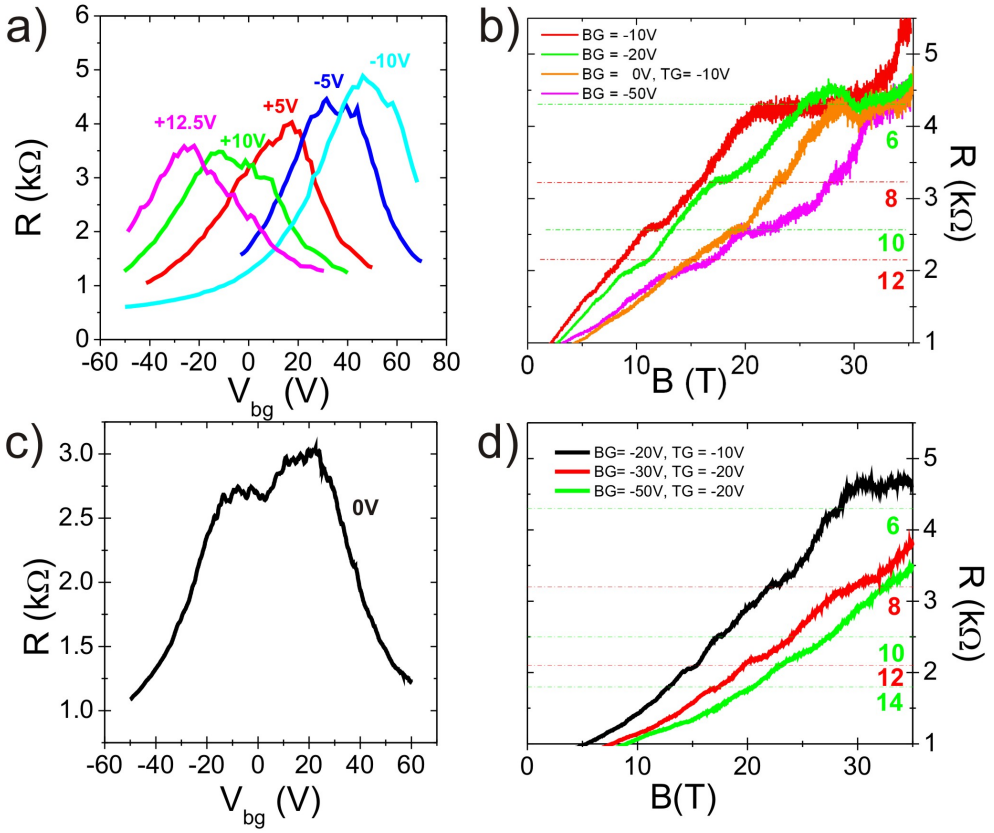

Figure 6.4: (a) Resistance R of the ABC trilayer device TG3 as a function of backgate voltage V_{bg} for different topgate voltages. (b) Magnetoresistance of this sample for different back- and topgate voltages. QHE plateaus develop at $\nu = 6$, 8, 10, and 12 (red and green dashed lines). (c) Resistance R of the ABC trilayer device TG4 as a function of backgate voltage V_{bg} at zero topgate voltage. (d) Magnetoresistance of this sample for different back- and topgate voltages. QHE plateaus develop at $\nu = 6$, 8, 10, 12 and 14 (red and green dashed lines).

plateau develops at $\nu = 12$, rather than at the expected $\nu = 14$, upon further increase of E_{ex} (for example at V_{bg} = -90 V with V_{tg} = -5 V). This observation suggests lifting of the valley degeneracy induced by the interlayer potential asymmetry [23], imposed by the top and back gates.

In order to confirm this indication we examined further samples (for sample images see Chap. 9), whereas for all samples Raman measurements proved that they are ABC trilayers. Fig. 6.4 shows the measurements of the samples TG3 and TG4. The expected trilayer plateaus ($\nu = 6$, 10 and 14) are indicated by *green* dashed lines, additional plateaus ($\nu = 8$ and 12) by *red* dashed lines, whereas the corresponding filling factors are indicated by corresponding numbers.
In Fig. 6.4(a) the typical ABC behavior of the backgate traces for different topgate values is observed for **sample TG3** (C2_D2): R^{max} increases with increasing E_{ex}, showing the characteristic behavior of a tunable bandgap. This high mobility sample ($\mu = 1800$ cm^2/Vs) shows again an indication for a plateau at $\nu = 12$, in addition to

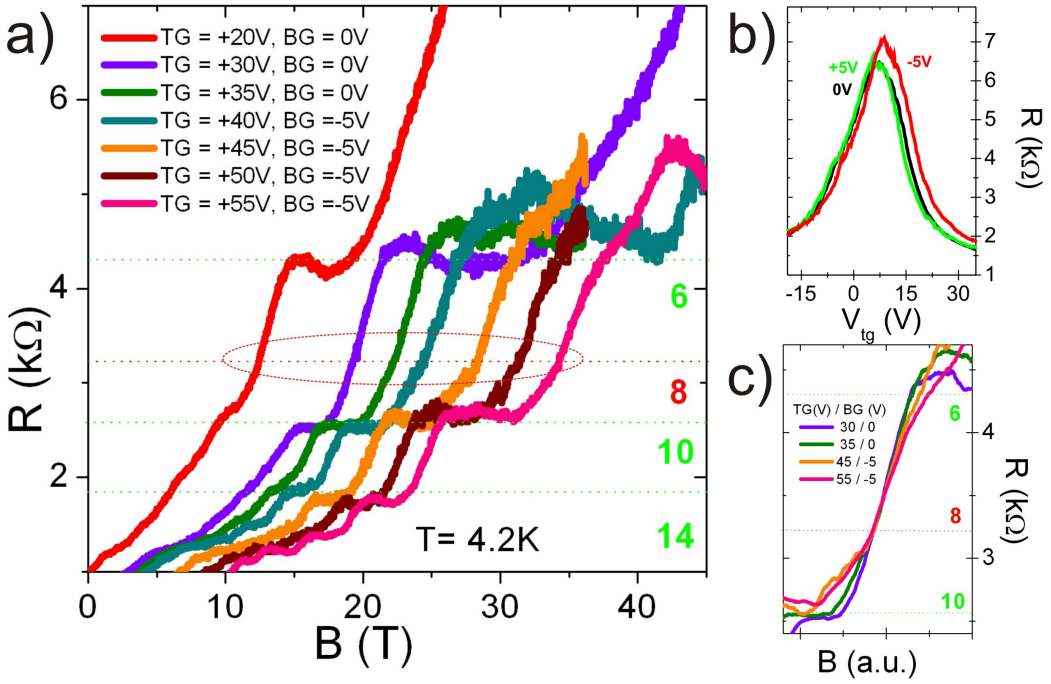

Figure 6.5: (a) Magnetoresistance of the sample TG5 for different back- and topgate voltages. QHE plateaus at $\nu = 6$, 10 and 14 (dashed lines), at $\nu = 8$ an additional plateau starts to develop (encircled in red). (b) Resistance R of the ABC trilayer device as a function of topgate voltage TG for different backgate voltages. (c) Shifted magnetoresistance of panel (a) in order to show better the development of plateau $\nu = 8$.

the expected plateaux at $\nu = 6$ and 10 [panel (b)]. Thus sample TG3 approves the observations of sample TG1. Additional a more pronounced plateau at filling factor $\nu = 8$ is observed (green and orange trace).
The same additional plateaux, namely $\nu = 8$ and 12, are present in the low mobility ($\mu = 500$ cm^2/Vs) **sample TG4** (K3_D2). Though the charge neutrality point shows a double-peaked structure [panel (c)], which is a reference to the inhomogeneity of this sample, we still observe plateaus at $\nu = 6$, 8, 10 and 12 for different combinations of back- and topgate voltages [panel (d)].

In contrast to sample TG1 - TG4, where particularly the variation of the back-gate voltage was used for introducing valley splitting, in **sample TG5** (K6_D3, $\mu = 1000$ cm^2/Vs) the back-gate was not working for voltages higher than about $\pm$ 5 V, therefore we had to vary the top-gate voltage. The charge neutrality point is at about $V_{\mathrm{CNP}} \sim 7$ V for $V_{\mathrm{tg}} = 0$ [cf. Fig. 6.5(b)], and the characteristics of a tunable bandgap are observed. We again notice very well defined Hall plateaus, both for electron and hole side of the charge neutrality point. Compare e.g. Fig. 6.5(a), where clear Hall plateaus can be seen at filling factor $\nu = 6$, 10, 14, 18 and 22. For better visibility, the plateau position of 6, 10 and 14 are indicated by *green*, dashed lines. Equally to previous samples, an additional plateau starts to develop at filling factor $\nu = 8$ (*red*, dashed line). For better conspicuousness we shifted the curves to the same B-field value [panel (c)]: increasing the external electric field we see that line slope starts to have some kink, indicating that a plateau starts to develop.

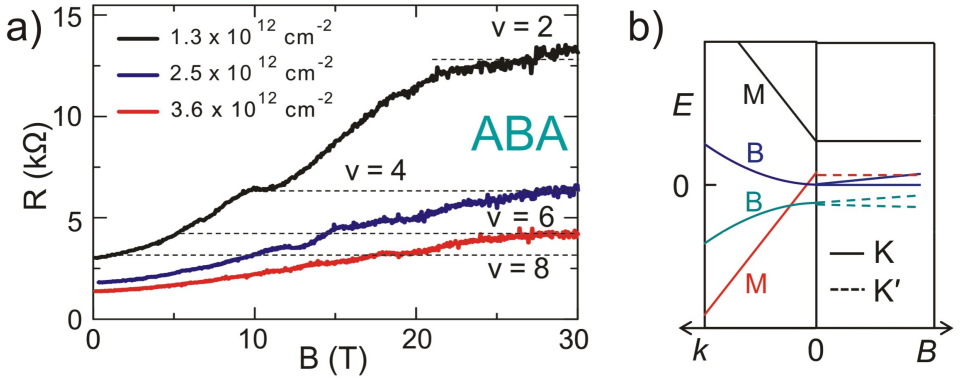

Figure 6.6: (a) Magnetoresistance of ABA-stacked trilayer (TG6) shown for three different carrier densities at 4.2 K. (b) Schematic low-energy band structure (left) and zero-energy LLs (right) of ABA trilayer graphene with all hopping parameters $\gamma_0 - \gamma_5$ included. The next-nearest layer couplings γ_2 and γ_5 shift the energy of monolayer-like (M) and bilayer-like (B) bands relative to each other, and also split zero-energy LLs into valleys.

Therefore, we can claim that we observe additional plateaus at filling factor $\nu = 8$ and 12 developing in ABC trilayer samples due to the breaking of valley degeneracy, as seen in TG1 - TG5.

6.2.2 ABA Trilayer Graphene

By contrast, the ABA-stacked trilayer **sample TG6** ($\mu \approx 1100$ cm^{2}V^{-1}s^{-1}) develops QHE plateaus at $\nu = 2$, 4, 6, and 8 with a step of $\Delta\nu = 2$ [Fig. 6.6(a)]. This observation is consistent with a recent theoretical prediction which includes the complete set of hopping parameters up to the next-nearest layer couplings γ_2 and γ_5 [81], cf. Chap. 2.1. This extended model predicts relative energy shifts of the monolayer-like and bilayer-like LLs in the ABA trilayer and a valley split of the zero-energy LLs by the γ_2 and γ_5. As a result, the 12-fold zero-energy levels (4 and 8 zero-energy levels from the monolayer-like and the bilayer-like subbands, respectively) split into 6 different energies with twofold spin degeneracy [Fig. 6.6(b)], leading to the QHE plateaus at filling factor intervals of $\Delta\nu = 2$. In addition, the presence of the external electric field generally splits the valley degeneracy of the LLs by the induced interlayer asymmetry [23]. As opposed to the case of ABA trilayer, the electric-field-induced valley splitting is expected to be smaller for the inversion-symmetric ABC trilayer. Therefore, the 4-fold spin and valley degeneracy is retained for the ABC trilayer device, resulting in QHE plateaus at $\nu = 6$ and 10. Under the large external electric field, however, the valley splitting leads to the QHE plateau at $\nu = 12$.

6.3 Summary

Our results are in agreement to existing experiments dealing with QHE in ABA [82] and ABC trilayers [8, 83, 84]. In Ref. [82], QHE plateaus in the ABA trilayer are observed at $\nu = \pm 2, \pm 4$, -6 but not at $\nu = +6$. The absence of a plateau at $\nu = +6$ is attributed to LL crossing. As pointed out in the Ref. [82], actual plateaus developing in the ABA trilayer can depend on a specific B (or in our case V_{bg}) where measurements are performed, due to the LL crossing between the monolayer-like and the bilayer-like subbands. For the ABC trilayer, Refs. [83] and [8] report QHE plateaus at $\nu = \pm 6, \pm 10, \pm 14...$, consistent with our results except the plateau at $\nu = 12$, whereas Ref. [84] observed rather unexpected plateaus at $\nu = \pm 9, \pm 18$, and -30.

In summary, we have investigated transport properties of trilayer graphene with different stacking order. Samples with ABA and ABC stacking differ characteristically in the sequence of quantum Hall plateaus, in agreement with recent theory. Whereas the splitting of the bands starts already at low magnetic field for ABA samples, with all hopping parameters included [81], in ABC trilayer graphene the 4-fold degeneracy is more preserved. The stacking order provides an additional degree of freedom to tune the electronic properties of trilayer graphene, combined with the interlayer asymmetry controlled by top and back gates.

7 Summary

The focus of this work has been the experimental investigation of graphite materials. Transport measurements were performed on both trilayer graphene and graphene nanoribbon (GNR) devices.

In the past, extensive studies have been performed on phase coherent effects in bulk graphene. Little attention, however, has been paid to phase coherent behavior in graphene nanoribbons. Here, for the first time, phase coherent effects in graphene nanoribbons are analyzed in detail. In contrast to bulk graphene, graphene nanoribbons mostly show weak localization (WL) due to the presence of edge scattering. Fitting the weak localization feature to the standard formula for narrow wires [42] was appropriate at low temperatures, but not at high temperatures. Therefore we expanded the standard formula including all scattering rates present in bulk graphene and got a better match between the experimental observations and theory.
Since universal conductance fluctuations are superimposed on weak localization at low temperatures, different averaging methods like gate-averaging and ensemble-averaging were used to suppress these fluctuations allowing us to again fit the (preserved) WL feature. Furthermore, analyzing the universal conductance fluctuations (on the one hand the amplitude, on the other hand the autocorrelation function) and thus determining the phase coherence length by an independent way allows us to verify our results from fitting the WL: primarily the phase coherence length increases with decreasing temperature and then saturates at a few hundred nm at mK-temperature. Excluding heating effects to be responsible for the saturation of L_φ, we rather suppose the occurrence of spin flip scattering at the ribbon edges. Therefore we recommend the performance of magneto-transport measurements at tilted magnetic fields.

Furthermore we had the outstanding possibility to measure graphene nanoribbon samples at Dresden High Magnetic Field Laboratory, were high pulsed magnetic fields up to 60 T are available. We performed magneto-transport measurements and corresponding numerical simulations [85] enabling us to conclude what kind of disorder is present in our devices. In comparison to previous work on GNRs in high magnetic fields [59, 86], our results are largely consistent with these results. Additional in our work, we have two separate experimental signatures, namely the visibility of the quantum Hall features and the zero field conductance value, in connection with the negative magneto-resistance, which enables us to state that at least edge disorder and short-range bulk impurities are needed to reproduce the experimental results.

We additionally measured trilayer graphene devices at Dresden High Magnetic Field Laboratory in collaboration with the University of Tokyo (Japan) and the Centre for Graphene Science at the University of Exeter (England), where the samples were fabricated and characterized by Raman measurements. The magneto-transport measurements show that the stacking-order of trilayer graphene has a high importance and determines the transport properties of the sample. For example, Bernal (ABA)-stacked trilayer exhibits an electric-field tunable band overlap, while rhombohedral (ABC)-stacked trilayer presents a tunable band gap. In double-gated trilayer graphene, we showed that the effects of applied electric and magnetic fields on the ABC-stacked trilayers are strikingly different from those on the ABA-stacked trilayers.

In summary, this thesis gives insight to the manifold diversity of graphite materials. Magneto-transport experiments on GNRs as well as on trilayer graphene devices demonstrate interesting phenomena which determine the properties of the devices and motivate further experiments on all members of the few layer graphene family.

8 Recipes

1. Preparation of the substrate
   - At the Regensburg, University of Applied Sciences coordinate systems were patterned by optical lithography on p++ doped silicon substrates with 300 nm SiO_2. In the following patterning processes these alignment marks enable us to detect the position of the graphene with respect to the coordinates.
   - Leybold Univex 450A: thermal evaporation of chromium (5 nm) and gold (60 nm), base pressure $5 \cdot 10^{-6}$ mbar
   - Lift-off in hot acetone (30 min hot plate 60° C), 5-10 s ultrasonic and subsequent cleaning with acetone and isopropanol
   - Spin-on of protection resist
   - Cleaving of the wafers into square pieces of 4.5 mm lateral length. In the following these pieces will be called chips.
2. Fabrication of graphene
   - Cleaning of the chips: 6 min acetone and ultrasonic, subsequent 6 min hot plate 60° C, 3 min ultrasonic in acetone, then cleaning in acetone and propanol
   - Plasma asher: Pressure 1.3 - 1.9 mbar, power 30%, 5 min
   - Exfoliation of the graphene with Scotch Magic Tape technique, rub the tape with a plastic cap for 4 min onto the silicon chips
   - Cleaning with acetone and isopropanol
3. Identify, characterize and localize the graphene with respect to the coordinate system with an optical microscope. First information of the layer thickness can be received from the grayscale contrast, see Fig.8.1.
4. Fabrication of test ribbons made of $Au_{40}Pd_{60}$
   - Spin-on resist: PMMA 950k 1%, 6 min hot plate 150° C
   - Electron-beam lithography (EBL): EHT 30 kV, aperture 30 μm, dose test (650-1200 pC/cm, spacing 10 nm)
   - Developing: MIBK/propanol (1:3) 20 s + 45 s propanol
   - Leybold Univex 450A: thermal evaporation of $Au_{40}Pd_{60}$, $5 \cdot 10^{-6}$ mbar
   - Lift-off in hot acetone (30 min hot plate 60° C)

5. Fabrication of graphene nanoribbons and GNR arrays
   - Spin-on resist: PMMA 950k 1%, 6 min hot plate 150° C
   - EHT 30 kV, aperture 30 μm, choose the dose corresponding to the results of the test (about 700 pC/cm), spacing 10 nm
   - Developing: MIBK/propanol (1:3) 20 s + 45 s propanol
   - Reactive ion etching
     - Cleaning the chamber: O_2, 100 sccm, 100 mTorr, 150 W, 8 min
     - Conditioning: O_2, 100 sccm, 27 mTorr, 50 W, 8 s
     - Etching: O_2, 100 sccm, 27 mTorr, 50 W, 8 s
   - Cleaning with acetone and isopropanol
6. Fabrication of the leads and contacts
   - Spin-on resist: PMMA 200k 7%, 6 min hot plate 150° C
   - Leads: EHT 30 kV, aperture 30 μm, dose: 280 μC/cm^2, spacing 10 nm
   - Contacts: EHT 30 kV, aperture 120 μm, dose: 280 μC/cm^2, spacing 30 nm
   - Developing: MIBK/isopropanol (1:3) 90 s + 30 s propanol
   - Thermal evaporation of 60 nm palladium mostly at Leybold Univex 450A (pump Univex over night, in order to get a pressure of $\approx 8 \cdot 10^{-7}$ mbar) and sometimes at the UHV sputtering and evaporation system of the group of Prof. Dr. Christoph Strunk
   - Lift-off in hot acetone (30 min hot plate 60° C)

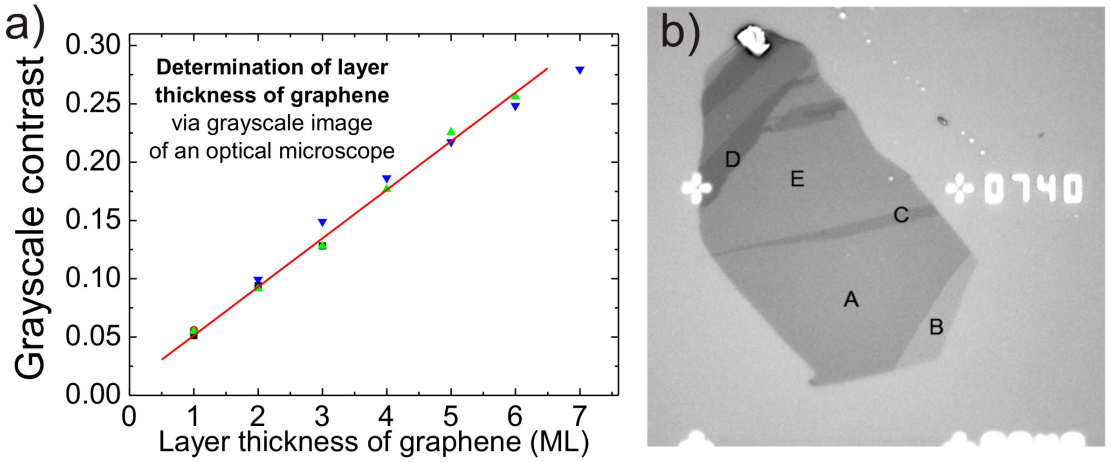

Figure 8.1: (a) Determination of the layer thickness by grayscale contrast in optical microscope [87]. (b) In a grayscale image converted microscope image showing a graphene flake with singlelayer (area B), bilayer (A, E), trilayer (C) and multilayer (D) graphene areas. The contrast of the image is increased for better visibility of the different graphene layers. The thickness was approved by Raman measurements [88].

9 Samples

9.1 Measurement Setup

In this section simple schematics explain the setups which were used for the measurements. Fig. 9.1 shows the two-terminal setup for the DC magneto-transport measurements used for the GNR and trilayer samples at Dresden High Magnetic Field Laboratory. Fig. 9.2 shows the two-terminal setup for the magneto-transport measurements for the GNR samples at the University Regensburg.

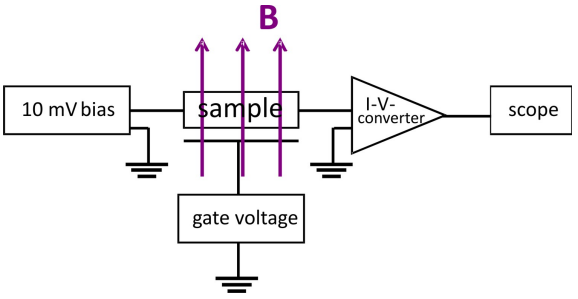

Figure 9.1: Schematic two-terminal setup for the DC magneto-transport measurements at Dresden High Magnetic Field Laboratory.

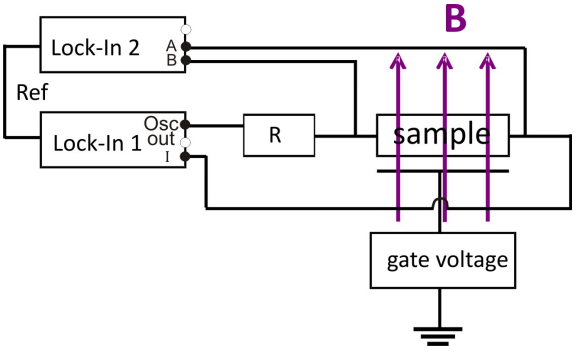

Figure 9.2: Schematic two-terminal setup for the magneto-transport measurements at the University of Regensburg. A series resistor R was used in order to measure at constant current. Lock-In 1 was used for current measurement, Lock-In 2 for voltage measurement.

9.2 Measured Samples and Additional Measurements

In this section sample details are summarized. First, table 9.1 summarizes all the sample properties of the (individual) GNRs and the GNR arrays. Second, images of all measured samples are shown: Fig. 9.3 shows the individual graphene nanoribbons and Fig. 9.4 the arrays of graphene nanoribbons, respectively, used for the measurements at the University of Regensburg. Fig. 9.5 shows the graphene nanoribbons measured at Dresden High Magnetic Field Laboratory. Fig. 9.6 and Fig. 9.7 the trilayer samples, which were also measured at HLD. Third of all, additional measurements are presented in Fig. 9.8 - 9.11.

Sample	Name	Width (nm)	GNRs	V_{CNP} (V)	Moblility (cm^2/Vs)
R1	2008-03-14_A	40	1	N/A[1]	N/A
R2	2010-05-17_D	40	1	$\geq$+50	330
R3	2008-11-20_D	40	1	N/A	N/A
R4	2008-09-15_B	40	1	N/A	N/A
R5	2010-05-06_C1	40	1	$\geq$+80	20
A1	2010-05-25_F	40	46	+35	680
A2	2010-05-06_A1	30	56	+10	30
A3	2010-05-17_C1_a	80	23	+40	500
A4	2010-05-17_C1_b	80	32	+20	240
A5	2010-05-17_D	70	69	+15	450
D1	2010-05-12_B_2565	70	1	-4.4	590
D2	2009-09-17_B_1760	70	1	$\geq$+70	25
D2	2009-10-06_A_2634	70	1	+25	N/A

Table 9.1: Different (individual) GNR samples and GNR arrays: Devices measured in Regensburg, with individual GNRs are named R1 - R5 and with arrays of GNRs A1 - A5. Devices with individual ribbons, measured at Dresden High Field Laboratory, are labeled as D1 - D3.

[1]For the samples from the first generation, named 2008-xx-xx_x, n++ doped silicon substrates were used. In most of the samples however, due to insufficient doping, its functionality as a back-gate could not be utilized. In order to be able to use the substrate as a back-gate down to very low temperature another substrate with higher doping (p++) was used, those samples are denominated as 2010-xx-xx_x

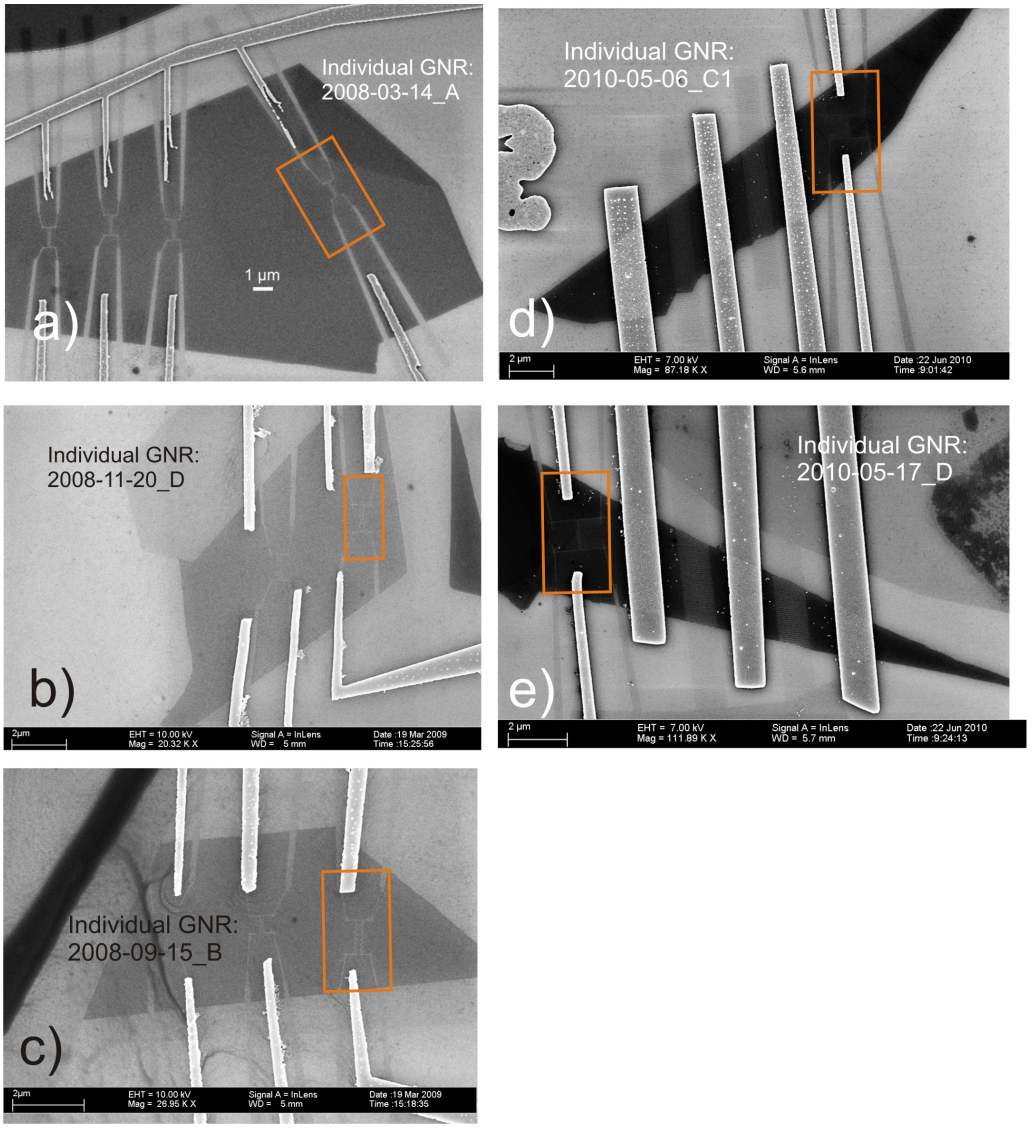

Figure 9.3: (a) Individual GNR sample: R1 (2008-03-14_A), (b) R3 (2008-11-20_D), (c) R4 (2008-09-15_B), (d) R5 (2010-05-06_C1) and (e) R2 (2010-05-17_D). All samples were measured at the University of Regensburg. The measured devices are highlighted in orange frames.

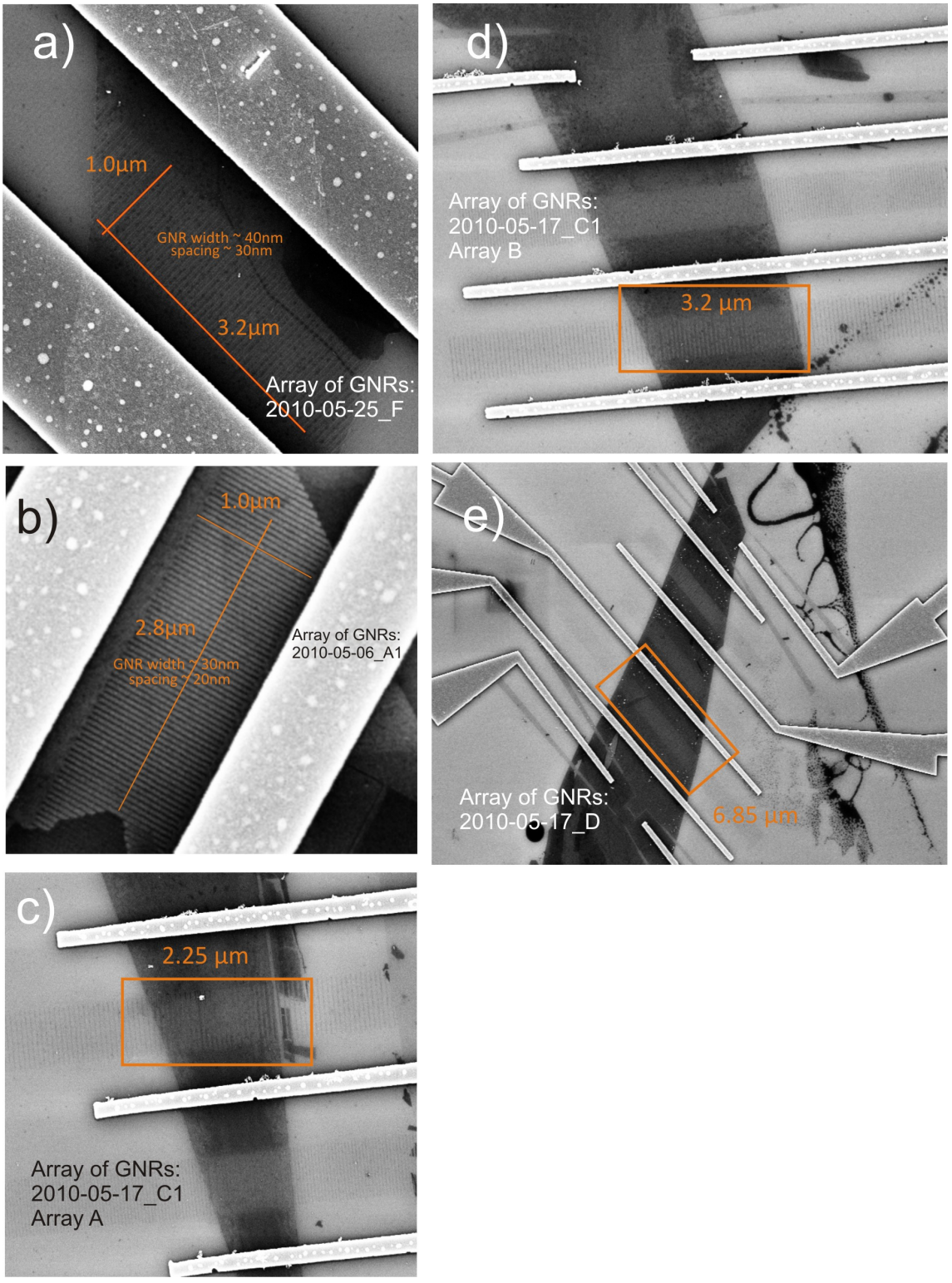

Figure 9.4: (a) Arrays of GNRs: sample A1 (2010-05-25_F), (b) A2 (2010-05-06_A1), (c) A3 (2010-05-17_C1 array A), (d) A4 (2010-05-17_C1 array B), and (e) A5 (2010-05-17_D). All samples were measured at the University of Regensburg. In panels (c, d and e) the measured devices are highlighted in orange frames.

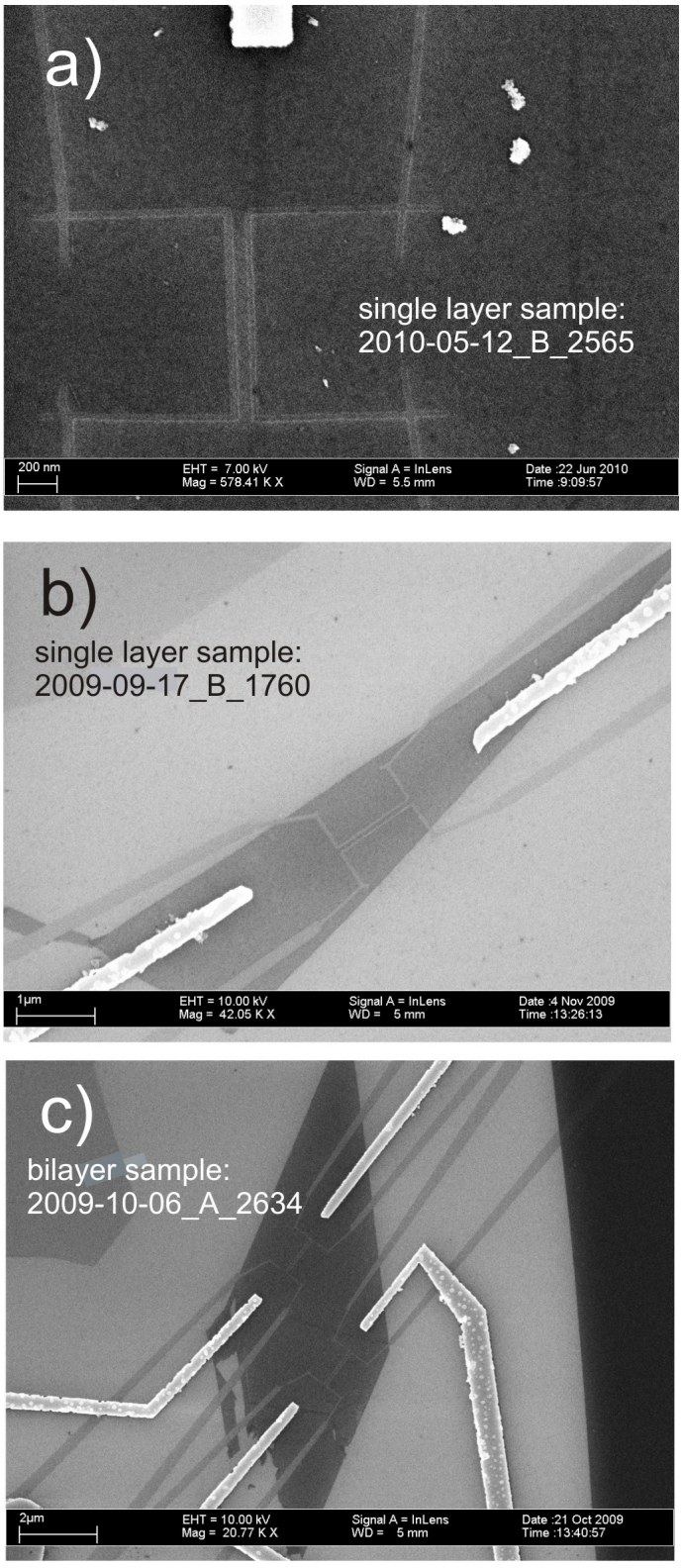

Figure 9.5: (a) Single layer sample: D1 (2010-05-12_B_2565), (b) single layer sample: D2 (2009-09-17_B_1760) and (c) bilayer sample: D3 (2009-10-06_A_2634). All samples measured at Dresden High Magnetic Field Laboratory in pulsed fields up to 60 T.

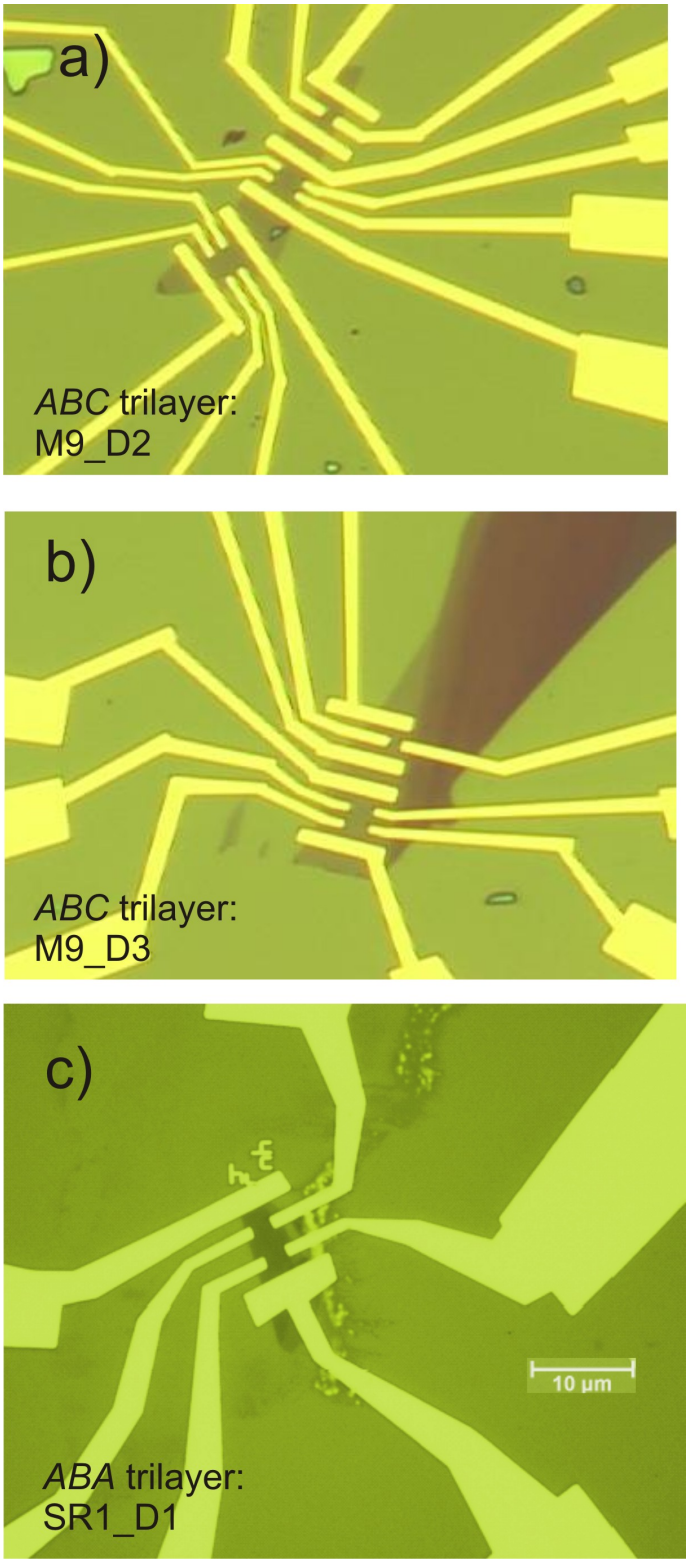

Figure 9.6: (a) *ABC* trilayer samples: TG1 (M9_D2) and (b) TG2 (M9_D3). Both samples are shown after the evaporation of the electrodes, before etching and before top gate evaporation. (c) *ABA* trilayer sample TG6 (SR1_D1). All of those samples were measured at Dresden High Magnetic Field Laboratory in pulsed fields up to 50 T.

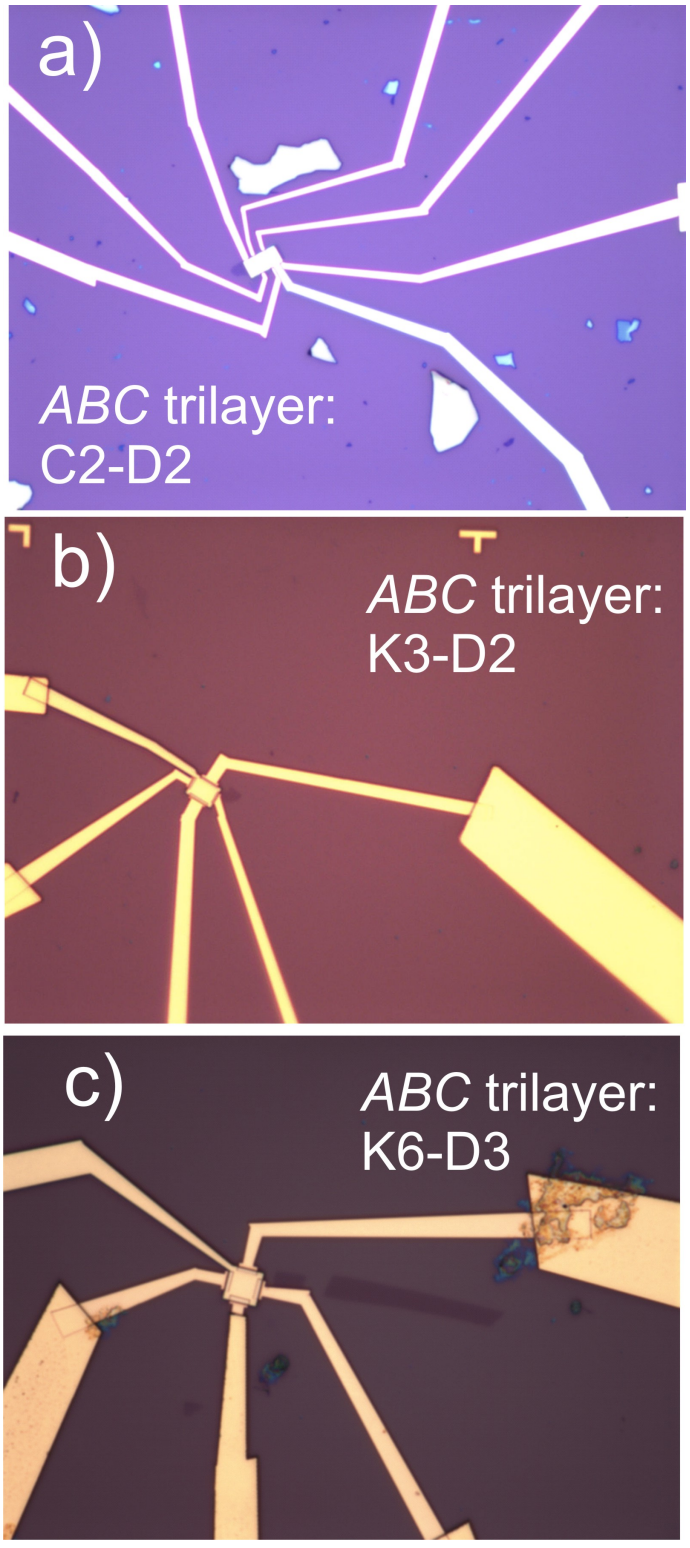

Figure 9.7: Further *ABC* trilayer samples: (a) TG3 (C2_D2), (b) TG4 (K3_D2) and (c) TG5 (K6_D3). All samples are shown after the evaporation of the electrodes and the top gate. All of them were measured at Dresden High Magnetic Field Laboratory in pulsed fields up to 50 T.

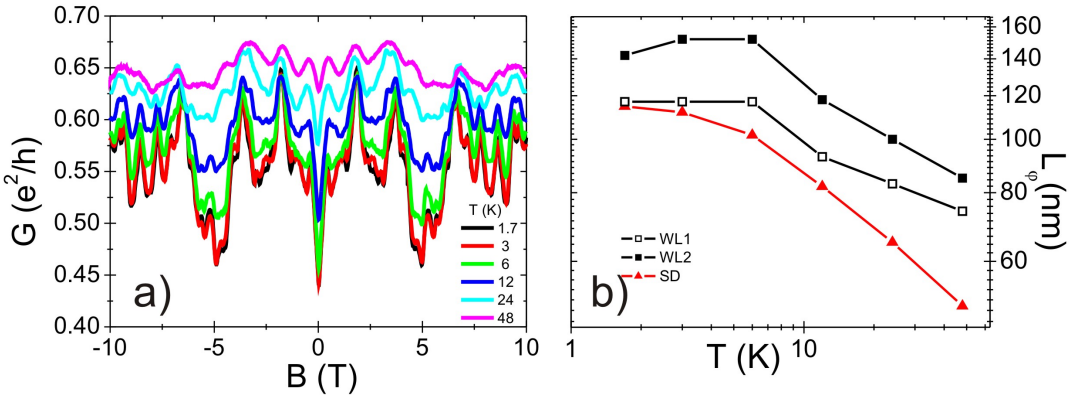

Figure 9.8: Individual GNR: sample R3 (W =40 nm). Magnetoconductance of the sample at temperatures ranging from 1.7 K to 48 K (a). In (b) the phase coherence length L_φ was determined by different methods like fitting weak localization (WL1 and WL2) and the amplitude of the UCFs (SD). However, strong UCFs are superimposed on the WL feature and it is difficult to fit, therefore the obtained values of L_φ can only be seen as a rough estimation.

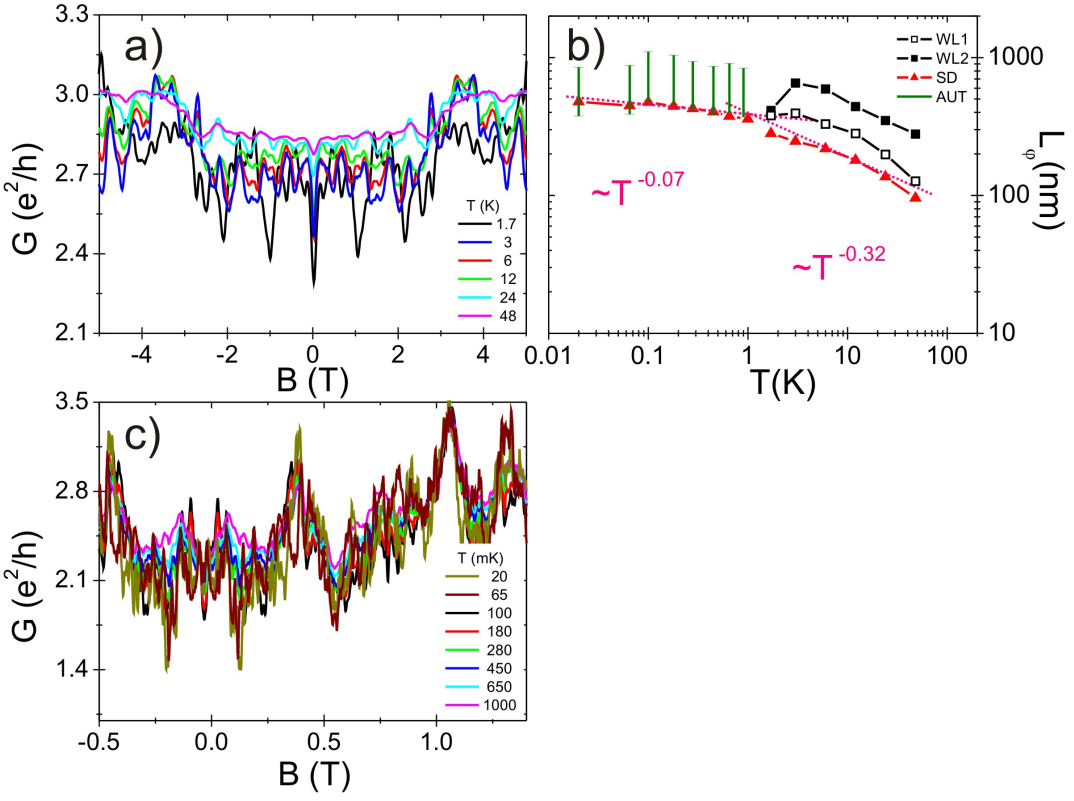

Figure 9.9: Individual GNR: sample R4 (W =40 nm). Magnetoconductance of the sample at temperatures ranging from 1.7 K to 48 K (a) and 20 mK to 1000 mK (c), respectively. In (b) the phase coherence length L_φ was determined by different methods like fitting weak localization (WL1 and WL2), analyzing the amplitude of the UCFs (SD) and calculating the autocorrelation function (AUT). Also here strong UCFs are superimposed on the WL and the WL-determined L_φ values can only be seen as a rough estimation. The pink, dashed lines are fits of the T-dependence of L_φ.

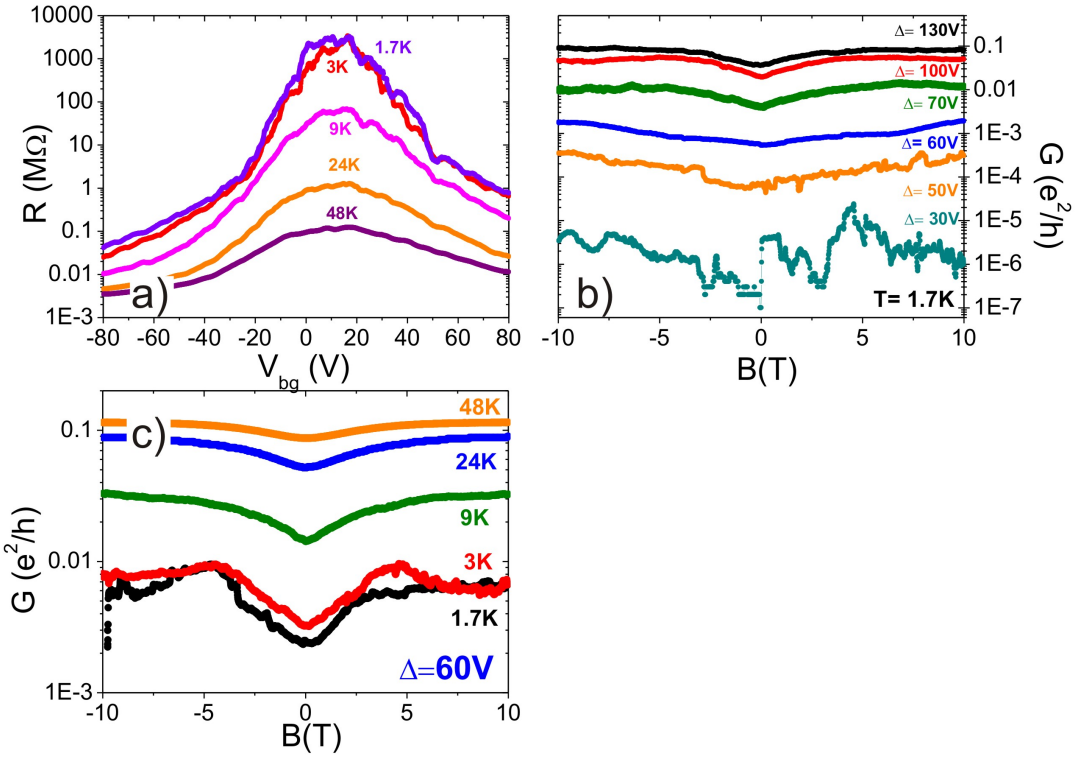

Figure 9.10: Array of 56 GNRs: sample A2 (W_{GNR} =30 nm). (a) Gate dependence of the resistance of the whole array at different temperatures ranging from 1.7 K to 48 K. (b) Magnetoconductance per single ribbon at different carrier densities at 1.7 K. (c) Magnetoconductance per single ribbon at temperatures ranging from 1.7 K to 48 K and Δ = 60 V away from the charge neutrality point.

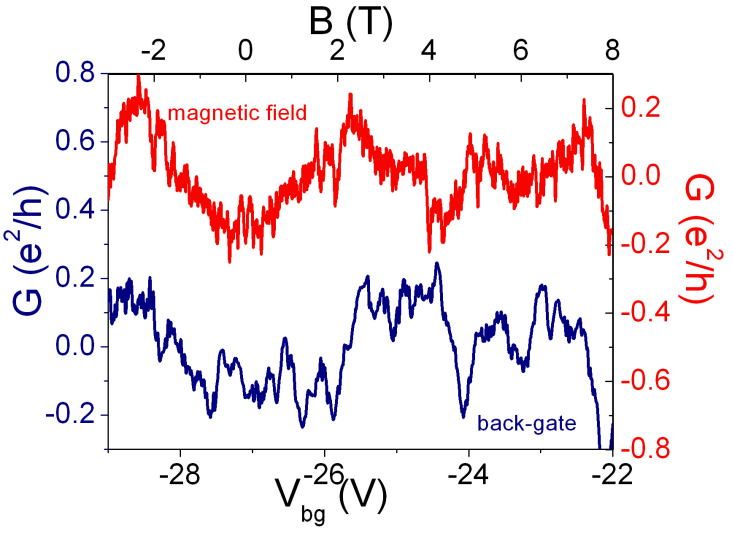

Figure 9.11: Comparison of the conductance fluctuations of sample R2 at 280 mK obtained by sweeping magnetic field (*red*) and back-gate voltage (*blue*), respectively. The background was subtracted from the measurement curves, as explained in Chap. 4.3. Clearly one can see, that the amplitude of the conductance fluctuations is the same (about 0.4 e^2/h).

Bibliography

[1] http://www.nobelprize.org/.

[2] A. K. Geim, *Science* **324**, 1530 (2009).

[3] M. Mucha-Kruczynski, E. McCann, and V. I. Falko, *Semicond. Sci. Technol.* **25**, 033001 (2010).

[4] M. Koshino and E. McCann, *Phys. Rev. B* **80**, 165409 (2009).

[5] E. McCann and V. I. Fal'ko, *Phys. Rev. Lett.* **96**, 086805 (2006).

[6] M. Koshino, *Phys. Rev. B* **81**, 125304 (2010).

[7] M. Koshino and E. McCann, *Phys. Rev. B* **79**, 125443 (2009).

[8] A. Kumar, W. Escoffier, J. M. Poumirol, C. Faugeras, D. P. Arovas, M. M. Fogler, F. Guinea, S. Roche, M. Goiran, and B. Raquet, *Phys. Rev. Lett.* **107**, 126806 (2011).

[9] E. McCann and M. Koshino, *Phys. Rev. B* **81**, 241409 (2010).

[10] A. H. Castro Neto, F. Guinea, N. M. R. Peres, K. S. Novoselov, and A. K. Geim, *Rev. Mod. Phys.* **81**, 109 (2009).

[11] M. F. Craciun, S. Russo, M. Yamamoto, J. B. Oostinga, A. F. Morpurgo, and S. Tarucha, *Nature Nanotech.* **4**, 383 (2009).

[12] S. H. Jhang, M. F. Craciun, S. Schmidmeier, S. Tokumitsu, S. Russo, M. Yamamoto, Y. Skourski, J. Wosnitza, S. Tarucha, J. Eroms, and C. Strunk, *Phys. Rev. B* **84**, 161408 (2011).

[13] A. Kumar, W. Escoffier, J. M. Poumirol, C. Faugeras, D. P. Arovas, M. M. Fogler, F. Guinea, S. Roche, M. Goiran, and B. Raquet, *arXiv:1104.1020v1* .

[14] K. S. Novoselov, A. K. Geim, S. Morozov, D. Jiang, M. I. Katsnelson, I. V. Grigorieva, S. V. Dubonos, and A. A. Firsov, *Nature (London)* **438**, 197 (2009).

[15] y. Zhang, Y. Tan, H. L. Stormer, and P. Kim, *Nature (London)* **438**, 201 (2005).

[16] K. S. Novoselov, E. McCann, S. V. Morozov, V. I. Falko, M. I. Katsnelson, U. Zeitler, D. Jiang, F. Schedin, and A. K. Geim, *Nature Phys.* **2**, 177 (2006).

[17] E. V. Castro, K. S. Novoselov, S. V. Morozov, N. M. R. Peres, J. M. B. L. dos Santos, J. Nilsson, F. Guinea, A. K. Geim, and A. H. C. Neto, *Phys. Rev. Lett.* **99**, 216802 (2007).

[18] J. B. Oostinga, H. B. Heersche, X. Liu, A. F. Morpurgo, and L. M. K. Vandersypen, *Nat. Mater.* **7**, 151 (2008).

[19] Y. Zhang, T.-T. Tang, C. Girit, Z. Hao, M. C. Martin, A. Zettl, M. F. Crommie, Y. R. Shen, and F. Wang, *Nature (London)* **459**, 820 (2009).

[20] F. Guinea, A. H. Castro Neto, and N. M. R. Peres, *Phys. Rev. B* **73**, 245426 (2006).

[21] H. Min and A. H. MacDonald, *Phys. Rev. B* **77**, 155416 (2008).

[22] M. Ezawa, *Physica E* **40**, 269 (2007).

[23] M. Koshino and E. McCann, *Phys. Rev. B* **81**, 115315 (2010).

[24] C. Stampfer, S. Fringes, J. Güttinger, F. Molitor, C. Volk, B. Terrés, J. Dauber, S. Engels, S. Schnez, A. Jacobsen, S. Dröscher, T. Ihn, and K. Ensslin, *Frontiers of Physics* **6**, 271 (2011).

[25] X. Li, X. Wang, L. Zhang, S. Lee, and H. Dai, *Science* **319**, 1229 (2008).

[26] S. S. Datta, D. R. Strachan, S. M. Khamis, and A. T. C. Johnson, *Nano Lett.* **8**, 1912 (2008).

[27] A. L. Elías, A. R. Botello-Méndez, D. Meneses-Rodríguez, V. J. González, D. Ramírez-González, L. Ci, E. Muñoz-Sandoval, P. M. Ajayan, H. Terrones, and M. Terrones, *Nano Lett.* **10**, 366 (2010).

[28] D. V. Kosynkin, A. L. Higginbotham, A. Sinitskii, J. R. Lomeda, A. Dimiev, B. K. Price, and J. M. Tour, *Nature* **458**, 872 (2009).

[29] L. Jiao, L. Zhang, X. Wang, G. Diankov, and H. Dai, *Nature* **458**, 877 (2009).

[30] K. Nakada, M. Fujita, G. Dresselhaus, and M. S. Dresselhaus, *Phys. Rev. B* **54**, 17954 (1996).

[31] E. R. Mucciolo, A. H. Castro Neto, and C. H. Lewenkopf, *Phys. Rev. B* **79**, 075407 (2009).

[32] M. Evaldsson, I. V. Zozoulenko, H. Xu, and T. Heinzel, *Phys. Rev. B* **78**, 161407 (2008).

[33] P. Gallagher, K. Todd, and D. Goldhaber-Gordon, *Phys. Rev. B* **81**, 115409 (2010).

[34] S. Dröscher, H. Knowles, Y. Meir, K. Ensslin, and T. Ihn, *Phys. Rev. B* **84**, 073405 (2011).

[35] M. Y. Han, B. Özyilmaz, Y. Zhang, and P. Kim, *Phys. Rev. Lett.* **98**, 206805 (2007).

[36] J. B. Oostinga, B. Sacepé, M. F. Craciun, and A. F. Morpurgo, *Phys. Rev. B* **81**, 193408 (2010).

[37] K. S. Novoselov, *Angew. Chem., Int. Ed.* **50**, 6986 (2011).

[38] Homepage of the Dresden High Field Laboratory: http://www.hzdr.de/db/Cms?pNid=580.

[39] Homepage of the EuroMagNET II: http://www.euromagnet2.eu/.

[40] T. Herrmannsdörfer and J. Wosnitza, *Physik in unserer Zeit* **38**, 242 (2007).

[41] F. V. Tikhonenko, A. A. Kozikov, A. K. Savchenko, and R. V. Gorbachev, *Phys. Rev. Lett.* **103**, 226801 (2009).

[42] E. McCann, K. Kechedzhi, V. I. Fal'ko, H. Suzuura, T. Ando, and B. L. Altshuler, *Phys. Rev. Lett.* **97**, 146805 (2006).

[43] F. V. Tikhonenko, D. W. Horsell, R. V. Gorbachev, and A. K. Savchenko, *Phys. Rev. Lett.* **100**, 056802 (2008).

[44] C. W. J. Beenakker and H. van Houten, *Solid State Physics* **44**, 1 (1991).

[45] V. I. Falko, K. Kechedzhi, E. McCann, B. Altshuler, H. Suzuura, and T. Ando, *Solid State Communications* **143**, 33 (2007).

[46] Ç. Kurdak, A. M. Chang, A. Chin, and T. Y. Chang, *Phys. Rev. B* **46**, 6846 (1992).

[47] Thanks to Edward McCann, Lancaster University, for helpful communications.

[48] P. McConville and N. O. Birge, *Phys. Rev. B* **47**, 16667 (1993).

[49] K. Kechedzhi, O. Kashuba, and V. I. Fal'ko, *Phys. Rev. B* **77**, 193403 (2008).

[50] M. Y. Kharitonov and K. B. Efetov, *Phys. Rev. B* **78**, 033404 (2008).

[51] K. Kechedzhi, D. W. Horsell, F. V. Tikhonenko, A. K. Savchenko, R. V. Gorbachev, I. V. Lerner, and V. I. Fal'ko, *Phys. Rev. Lett.* **102**, 066801 (2009).

[52] http://en.wikipedia.org/wiki/Root_mean_square.

[53] G. Bohra, R. Somphonsane, N. Aoki, Y. Ochiai, R. Akis, D. K. Ferry, and J. P. Bird, *arXiv:1203.6385* .

[54] J. Eroms and D. Weiss, *New J. Phys.* **11**, 095021 (2009).

[55] C. Stampfer, J. Güttinger, S. Hellmüller, F. Molitor, K. Ensslin, and T. Ihn, *Phys. Rev. Lett.* **102**, 056403 (2009).

[56] N. Tombros, A. Veligura, J. Junesch, M. H. D. Guimarães, I. J. Vera-Marun, H. T. Jonkman, and B. J. van Wees, *Nature Physics* **7**, 697 (2011).

[57] M. Fujita, K. Wakabayashi, K. Nakada, and K. Kusakabe, *J. Phys. Soc. Jpn.* **65**, 1920 (1996).

[58] Y. W. Son, M. L. Cohen, and S. G. Louie, *Nature* **444**, 347 (2006).

[59] J.-M. Poumirol, A. Cresti, S. Roche, W. Escoffier, M. Goiran, X. Wang, X. Li, H. Dai, and B. Raquet, *Phys. Rev. B* **82**, 041413 (2010).

[60] Jürgen Wurm, PhD tesis, Dirac fermions in graphene nanostructures: Edge effects on spectral density and quantum transport.

[61] G. Xu, C. M. Torres, J. Tang, J. Bai, E. B. Song, Y. Huang, X. Duan, Y. Zhang, and K. L. Wang, *Nano Letters* **11**, 1082 (2011).

[62] M. Wimmer and K. Richter, *J. Comput. Phys.* **228**, 8548 (2009).

[63] J. Martin, N. Akerman, G. Ulbricht, T. Lohmann, J. H. Smet, K. von Klitzing, and A. Yacoby, *Nature Physics* **4**, 144 (2008).

[64] A. Castellanos-Gomez, R. H. Smit, N. Agraït, and G. Rubio-Bollinger, *Carbon* (2011).

[65] A. J. M. Giesbers, L. A. Ponomarenko, K. S. Novoselov, A. K. Geim, M. I. Katsnelson, J. C. Maan, and U. Zeitler, *Phys. Rev. B* **80**, 201403 (2009).

[66] L. Zhang, Y. Zhang, M. Khodas, T. Valla, and I. A. Zaliznyak, *Phys. Rev. Lett.* **105**, 046804 (2010).

[67] J. G. Checkelsky, L. Li, and N. P. Ong, *Phys. Rev. Lett.* **100**, 206801 (2008).

[68] J. G. Checkelsky, L. Li, and N. P. Ong, *Phys. Rev. B* **79**, 115434 (2009).

[69] S. Das Sarma, S. Adam, E. H. Hwang, and E. Rossi, *Rev. Mod. Phys.* **83**, 407 (2011).

[70] D. V. Khveshchenko, *Phys. Rev. Lett.* **87**, 206401 (2001).

[71] B. I. Shklovskii and A. L. Efros, *Electronic Properties of Doped Semiconductors*, 1984.

[72] N. F. Mott, *Philos. Mag.* **19**, 835 (1969).

[73] M. Monteverde, C. Ojeda-Aristizabal, R. Weil, K. Bennaceur, M. Ferrier, S. Guéron, C. Glattli, H. Bouchiat, J. N. Fuchs, and D. L. Maslov, *Phys. Rev. Lett.* **104**, 126801 (2010).

[74] A. A. Avetisyan, B. Partoens, and F. M. Peeters, *Phys. Rev. B* **81**, 115432 (2010).

[75] F. Zhang, B. Sahu, H. Min, and A. H. MacDonald, *Phys. Rev. B* **82**, 035409 (2010).

[76] D. R. Cooper, B. D'Anjou, N. Ghattamaneni, B. D. Harack, M. Hilke, A. Horth, N. Majlis, M. Massicotte, L. Vandsburger, E. Whiteway, and V. Yu, *ISRN Condensed Matter Physics* **x**, x (2011).

[77] A. C. Ferrari, J. C. Meyer, V. Scardaci, C. Casiraghi, M. Lazzeri, F. Mauri, S. Piscanec, D. Jiang, K. S. Novoselov, S. Roth, and A. K. Geim, *Phys. Rev. Lett* **97**, 187401 (2006).

[78] Y. K. Koh, M.-H. Bae, D. G. Cahill, and E. Pop, *ACS Nano* **5**, 269 (2011).

[79] L. M. Malard, M. H. D. Guimarães, D. L. Mafra, M. S. C. Mazzoni, and A. Jorio, *Phys. Rev. B* **79**, 125426 (2009).

[80] C. H. Lui, Z. Li, Z. Chen, P. V. Klimov, L. E. Brus, and T. Heinz, *Nano Lett.* **11**, 164 (2011).

[81] M. Koshino and E. McCann, *Phys. Rev. B* **83**, 165443 (2011).

[82] T. Taychatanapat, K. Watanabe, T. Taniguchi, and P. Jarillo-Herrero, *Nat. Phys.* **7**, 621 (2011).

[83] L. Zhang, Y. Zhang, J. Camacho, M. Khodas, and I. A. Zaliznyak, *Nature Phys.* **7**, 953 (2011).

[84] W. Bao, L. Jing, Y. Lee, J. V. Jr., P. Kratz, D. Tran, B. Standley, M. Aykol, S. B. Cronin, D. Smirnov, M. Koshino, E. McCann, M. Bockrath, and C. N. Lau, *Nature Phys.* **7**, 948 (2011).

[85] Done by Jürgen Wurm from the Institute of Theoretical Physics, University of Regensburg.

[86] R. Ribeiro, J.-M. Poumirol, A. Cresti, W. Escoffier, M. Goiran, J.-M. Broto, S. Roche, and B. Raquet, *Phys. Rev. Lett.* **107**, 086601 (2011).

[87] Graph from Jonathan Eroms.

[88] Raman measurements were done by Stefanie Heydrich.

Acknowledgements

An dieser Stelle möchte ich all denen danken, die auf verschiedenste Art zum Gelingen dieser Arbeit beigetragen haben.
Prof. Dr. Dieter Weiss, der mir die Arbeit an einem sehr interessanten Thema ermöglichte und stets als Ansprechpartner zur Verfügung stand.
Prof. Dr. Christoph Strunk, der meine die Arbeit am Hochfeldlabor Dresden anleitete und unterstüzte.
Besonderen Dank auch Jonathan Eroms der mir immer mit Rat und Tat zur Seite stand. Danke für die unendliche Geduld, die produktiven Vorschläge und die gute Betreuung! Danke auch für die Unterstützung und Anteilnahme vorallem im letzten Jahr!
SungHo Jhang, für seine allzeitige Hilfsbereitschaft, die vielen Diskusionen über Graphene und die gute Zusammenarbeit in Dresden.
Shintaro Tokumitsu, Michihisa Yamamoto, Monica Craciun und Saverio Russo für die gute Zusammenarbeit bei den Trilayer Messungen in Dresden! Und die vielen interesannten kulturellen, wie auch wissenschaftlichen Einblicke und Motivation.
Yurii Skourski, der nicht nur im Hochfeldlabor Dresden immer für alle Fragen zur Seite stand. Und die Aufenthalte dort mit seiner freundlichen, positiven Art sehr schön machte!
Prof. Dr. Klaus Richter, Jürgen Wurm und Jan Bundesmann für den theoretischen Support und der Hilfe bei der Interpretation meiner Messungen.
Stefanie Heydrich für die Raman Messungen.
Meinen Kollegen am Lehrstuhl Weiss für ihre Hilfsbereitschaft und Unterstützung in jeglichen Fragen! Vorallem Uli Gürster und Cornelia Linz bei Fragen im Reinraum. Elke Haushalter und Claudia Rahm für stete Hilfsbereitschaft und ein gutes Klima in der Arbeitsgruppe. Daniel Neumaier für hilfreiche Diskussionen und Informationen, auch als er nicht mehr in Rgbg. war.
Und Andreas Einwanger, der immer da war wenn ich Hilfe brauchte, für alle Tipps, ganz viel Hilfe und viele erheiternde Gespräche!
Meinen Korrekturlesern, die zum Gelingen und Verständnis meiner Arbeit unendlich viel beigetragen haben! Nochmals vielen Dank an: Christan, Jonathan, SungHo, Florian und Thomsi.
Meinen Freunden, vor allem Betti, Uli, Rudl, Thomsi, Susanne und Marion die immer für mich da waren, mit denen ich viele tolle Wochenenden verbringen durfte und die mich auch in schweren Tagen unterstüzten!
Meinen Eltern, Großeltern, sowie Hannes und Stefan, die für Abwechslung und Aufheiterung sorgten und mich mit Geduld und Verständnis in jeder Hinsicht unterstützten.

Danke an euch alle!